Isosurface Interactions Within Turbulent Premixed Hydrogen and Hydrocarbon Flames

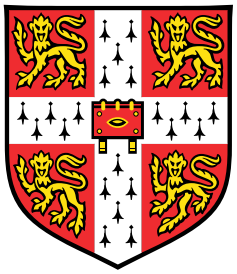

Shrey Trivedi

Supervisor: Professor R. S. Cant

Department of Engineering
University of Cambridge

This dissertation is submitted for the degree of
Doctor of Philosophy

Sidney Sussex College July 2019

Declaration

This thesis is the result of my own work and includes nothing which is the outcome of work done in collaboration except as declared in the Preface and specified in the text. It is not substantially the same as any that I have submitted, or, is being concurrently submitted for a degree or diploma or other qualification at the University of Cambridge or any other University or similar institution except as declared in the Preface and specified in the text. I further state that no substantial part of my thesis has already been submitted, or, is being concurrently submitted for any such degree, diploma or other qualification at the University of Cambridge or any other University or similar institution except as declared in the Preface and specified in the text. It does not exceed the prescribed word limit for the relevant Degree Committee

Shrey Trivedi
July 2019

Isosurface Interactions Within Turbulent Premixed Hydrogen and Hydrocarbon Flames

Shrey Trivedi

The purpose of this thesis is to provide better insight into isosurface interactions in premixed turbulent flames. These interactions for a suitable isosuface corresponding to the reaction zone can be interpreted as flame-flame interactions. Isosurface interactions can be identified with the help of Morse theory of critical points and the local topology at critical points can be evaluated. In previous studies, the interactions have been categorised into four different groups, namely reactant pocket, tunnel formation, tunnel closure and product pocket. The effect of isosurface interactions on flame propagation is analysed by expanding the equations for Surface Density Function (SDF) and displacement speed in the vicinity of a critical point and Direct Numerical Simulation (DNS) is used to validate the theoretical results. In particular, the formation of isolated pockets of reactants or products is associated with flame pinch–off events which cause rapid changes in the flame surface area. In the past, the analysis of pocket formation in turbulent premixed flames has been carried out in two dimensions. In this thesis, the topological analysis is carried out in three dimensions with emphasis on the formation and subsequent burnout of reactant pockets. The terms of the SDF transport equation show singular behaviour which was also observed in the previous two–dimensional analysis. Singular behaviour is also observed in the terms of the displacement speed equation close to reactant pocket burnout. The theory is compared against DNS data from hydrogen–air flames and good agreement is obtained.

Histograms showing the frequency of occurrence of each topological event are presented for different hydrogen and hydrocarbon flame cases. The analysis is first carried out in a twin flame setup with two flames propagating towards each other. It is observed that the relative frequency of occurrence of each type of topology changes with changes in turbulence intensity. With increasing turbulence intensity in hydrocarbon flames, the fraction of product pockets and tunnel formation events increases whereas the fraction of reactant pockets and tunnel closure events decreases. The results for hydrocarbon flames are compared with those for hydrogen flames and the differences are explained both qualitatively and

quantitatively. Self-interactions in single hydrocarbon flames are also analysed and it is found that a significant number of self interactions exist within individual flames. The analysis is further extended to systematic variations in integral length scale as well as turbulence intensity.

Acknowledgements

Family: I owe my greatest thanks to Stan Birkin for his unconditional support during my PhD. And sincere thanks to my parents and my brother who still could not believe I did a PhD.

Academics: I have been very fortunate to work with two of the nicest and kindest people I have ever come across - My supervisor Professor Stewart Cant whose exceptional support has been a blessing for me as a researcher, and Professor John Harvey who helped me unconditionally to pursue a side research project on DSMC. My gratitude also to my graduate tutors Prof. Andy Neely and Dr. Berry Groisman who have been very supportive at every stage of my PhD. Also, many thanks to Professor Matthew Juniper for providing extra computing time in the moment of need and Professor Mastorakos, my advisor, who played a great supporting role. Special thanks to Dr. Jackie Chen from Sandia who always found time to provide her insight into our research work, and Professor Paul Ronney from USC, my Master's advisor, who continued to support me during my PhD.

Friends and Colleagues: Girish, Audrey, Alex, Chin Yik, Ryan and Dante for making research even more fun. Specially the intense discussions with Girish which always came in handy, Ryan helped with the research tools used in this thesis, Audrey for the never-ending laughs that made my jaws hurt.

Funding and resources: Many thanks to the Cambridge Trust for providing the financial support for my PhD. Special thanks to the Nehru Trust and Dr. Anil Seal for providing an additional scholarship in the 2^{nd} year onwards for the "exceptional progress." Thanks also to Sidney Sussex college for providing numerous travel grants for attending academic conferences. The UKCTRF has provided the much needed computing resources during the course of my PhD and my sincere thanks to all the people involved.

Coffee: The lifeline during my PhD, and many thanks to Kate for providing a continuous supply of coffee in the kitchen.

To my family . . .

Table of contents

List of figures

List of tables

Chapter 1

Introduction

Combustion-related processes provide a major fraction of the energy requirement in the world. Approximately 85% of the total world energy in 2018 was fulfilled by oil, coal and natural gas [1] and these are expected to remain the primary sources of energy for years to come [1]. At the same time, there are growing concerns about the local and global effects of emissions from combustion and the need for efficient burning has never been greater. Premixed flames are of growing importance due to their potential in controlling pollutants. Most flames in engineering applications are turbulent, which provides enhanced burning rates by increasing the flame surface area [2]. Moreover, burning increases further as the turbulence intensity increases [3, 4].

The increase in flame surface area caused by turbulence has been studied with the help of flame stretch [5, 6, 7, 8]. Stretch effects have been incorporated into flame surface density equations [9, 10, 11, 12]. The balance equation of flame surface density provides an insight into the production, transport and destruction of the flame area. While flame stretch is responsible for flame area production, flame-flame interactions are believed to be the leading mechanisms for flame area destruction [3, 13, 14, 15]. Flame-flame interactions have been considered in a number of studies [16, 17, 18, 19] but their effects are still not well understood.

Flame-flame interactions occur when the flame becomes highly wrinkled at high turbulence intensities and the flame surface begins to interact with itself locally [15, 20, 21, 22]. They also occur in systems with multiple ignition points and the adjacent flame surfaces collide. Flame-flame interactions are responsible for altering flame surface area [3, 14, 20, 21], for the formation of cusps and reactant pockets [15, 20, 23, 24] and for inducing combustion-related noise [25, 26, 27]. Changes in flame area due to flame-flame interactions are still not accounted for in current models. There is a need to understand the fundamentals of this phenomenon with a view to developing improved mathematical models.

Flame cusps result from flame-flame interactions in narrow elongated flame channels [15]. The formation of cusps in turbulent flames was first suggested by Karlovitz et al. [5] and its dynamics were studied by Zel'dovich [13] who suggested cusps as the "cure" to unmitigated growth of instabilities in the flames. The structures of the colliding flame surfaces merge and lead to mutual annihilation [28, 29]. The colliding flames were found to accelerate prior to merging in a numerical study by Chen and Sohrab [28]. The role of chemistry in flame acceleration prior to merging was investigated by Echekki et al. [29]. The interactions in references [28, 29] were termed as normal interactions where the direction of flame propagation was towards each other. Counter-normal interactions occur when the flame surfaces propagating in opposite directions are brought together by turbulent straining. Such interactions can result in partially-burnt reactants caused by flame extinction [19, 30, 31].

Flame-flame interactions also result in formation of pockets [32, 33]. The dynamics of pocket formation in a flame has been analysed mathematically in two dimensions by Kollmann and Chen [23] and in three dimensions by Trivedi et al. [24]. In other two-dimensional flame topology studies by Chen et al. [20], the mechanism of pocket formation in a lean methane-air flame was investigated. Morse theory of critical points [34] was used to identify flame-flame interactions. Pocket formation was shown to occur in three stages: (1) merging of the reaction layers within adjacent flames on very short timescales, (2) cusp recovery and (3) formation of an isolated flame pocket which eventually burns out [20]. Another important aspect of this two-dimensional study was that strain and curvature effects were found to play an important role in pocket formation.

The theory of critical points was also used in a three-dimensional study emphasising on the flame–flame interactions in a pair of colliding statistically planar hydrogen-air flames [21]. This analysis was performed using the DNS data of Hawkes et al. [35] which consists of counter flowing hydrogen flames at Damköhler number Da = 0.54 (Da+ case) and Da = 0.13 (Da- case). This study [21] determined the full set of all possible flame-flame interaction topologies. Another method to evaluate flame-flame interactions was developed by Dunstan et al. [19] using the wavelet transform method and it was applied to a dual V-flame configuration [19, 36]. The major difference between the above two methods is that the wavelet transform method requires flame surfaces at two different time steps whereas the critical point method can be applied on an instantaneous snapshot of the flame. All of the flame-flame interaction topologies can be broadly classified into four main categories, namely “product pockets", “tunnel closure", “tunnel formation" and “reactant pockets" [19].

In this thesis, the numerical tools of Griffiths et al. [21] are adapted for the analysis of flame-flame interactions in premixed hydrocarbon flames and the results are compared to

those of hydrogen flames. The dataset of Hawkes et al. [35] is used for analysing flame-flame interactions in hydrogen air flames for two different Damköhler numbers. The hydrocarbon-flame datasets are created for turbulence intensities as high as $u' = 40s_L$, where s_L is the unstrained laminar flame speed. Variation in turbulence intensity u' as well as integral length scales of turbulence ℓ_0 are considered. The statistics of critical points and the corresponding topology at each point is analysed and compared for hydrocarbon and hydrogen flames.

The next chapter provides the background theory on the factors influencing flame-flame interactions in turbulent flames. The theory of mutual annihilation of interacting flames is discussed [28, 29]. In turbulent flames, mutual annihilation of flames can occur either when two flame surfaces collide with each other or when the flame surfaces come close to each other in a narrow channel. The flames accelerate prior to colliding which results in increased local fuel consumption rate. Likewise, reactant pockets can also form due to flame-flame interactions and these can alter the flame surface area and the fuel consumption rate.

Chapter 3 provides a review of the numerical tools developed by Griffiths et al. [21] to analyse critical points and the corresponding topology. Critical point theory [34] is utilized to record the flame-flame interactions and the results for the hydrogen dataset [35] are recreated to compare them with those obtained by Griffiths et al. [21]. A mathematical explanation of the theory of pocket formation is provided by analysing the terms in surface density function equation close to the location of the critical points. The equations for displacement speed are also analysed.

Chapter 4 deals with the comparison of critical point statistics between hydrocarbon and hydrogen flames in a twin flame setup. Furthermore, the self interactions in single hydrocarbon flames are also analysed. In Chapter 5, the effect of flame-flame interactions on overall flame propagation is studied. The change in flame area A_T, flame consumption speed s_T and turbulent diffusivity D_T are considered.

Chapter 2

Combustion and Turbulence

2.1 Background Literature

In premixed turbulent combustion studies, flame speed and flame area are of major importance. They are strongly dependent on each other as changes in turbulent flame speed are usually accounted for by changes in flame surface area. Flame-flame interactions are capable of changing the flame surface area and hence the flame speed also. Identifying flame-flame interactions also requires a well-defined flame surface. Given that the flames in practice have a finite thickness, an isosurface of the progress variable corresponding, for example, to the maximum reaction rate can be used to define a flame surface.

Different regimes of premixed turbulent combustion occur depending on the interaction between different scales of turbulence and the flame structure. The nature of flame-flame interactions may vary in these different regimes. In the corrugated flame regime, the flame behaves like a wrinkled laminar flame and the full structure of the flame remains intact. By contrast, in the thin reaction zones regime, the preheat zone of the flame is disrupted and the isosurfaces of the progress variable within the disrupted region can self interact within the flame brush.

The rate of increase of the flame area, called flame stretch, provides information on the changes in flame area and the factors affecting it. Flame surface density Σ defined as the flame surface area per unit volume is a quantity often used for flame area evaluation and its balance equation quantifies the effects of flame stretch. Curvature has a particular importance in flame-flame interactions. Regions of high curvature are expected to have more interaction events, especially events like flame pinch-off that result in the formation of reactant pockets [20]. Shape factors, defined as the ratio of maximum to minimum principal curvature, can be used to evaluate the topology near the flame-flame interaction events [21, 37].

The balance equation for Σ provides a good mathematical basis to study the dynamics of flames near flame-flame interaction events [23]. A generalised form of the flame surface density called the surface density function $\sigma = |\nabla c|$ can be easily evaluated in numerical simulations. Understanding the importance of various terms in the surface density function equations could provide the key to modelling the effects of flame-flame interactions on flame surface area and consequently provide better predictions of the flame speed.

2.1.1 Flamelet assumption

A flamelet is a thin and highly wrinkled interface that separates reactants from products. This thin interface is essentially a strained and curved laminar flame that contains all the chemistry and molecular transport effects of a flame. This makes it possible to decouple the chemistry from the flow and significantly simplify the modelling of flames. Most lower order models used in computational studies are based on the flamelet assumption [38], for example, the Bray Moss Libby model [39] or the G-equation model [4, 40].

A premixed laminar flame propagates normal to itself toward the "cold" reactants and turns them into "hot" products. This conversion occurs within a well-defined and robust structure which is illustrated in Figure 2.1. The flame structure can be divided into three zones:

- The **convection-diffusion zone** or the **preheat zone** is where the preheating of reactants occurs due to thermal conduction from the reaction zone. The reactants are transported from the preheat zone into the reaction zone by convection and molecular diffusion. No significant reactions take place in this zone.

- The **reaction zone** is where most of the reactions take place. The temperature in this zone is high enough to exceed the activation energy of some of the important elementary reactions to sustain combustion. Many highly reactive radicals are present in this zone. The reaction zone is very thin and has a very high gradient of temperature and species resulting in the diffusion of reactants from the preheat zone into it. The balance between reaction and diffusion governs the propagation rate of the flame. Sometimes an additional zone called the **equilibration zone** (not shown in the figure) is also defined within the reaction zone. This is where most of the slower three-body recombination reactions occur [41].

- The **product zone** is where the final products emerge following the chemical reactions in the reaction zone.

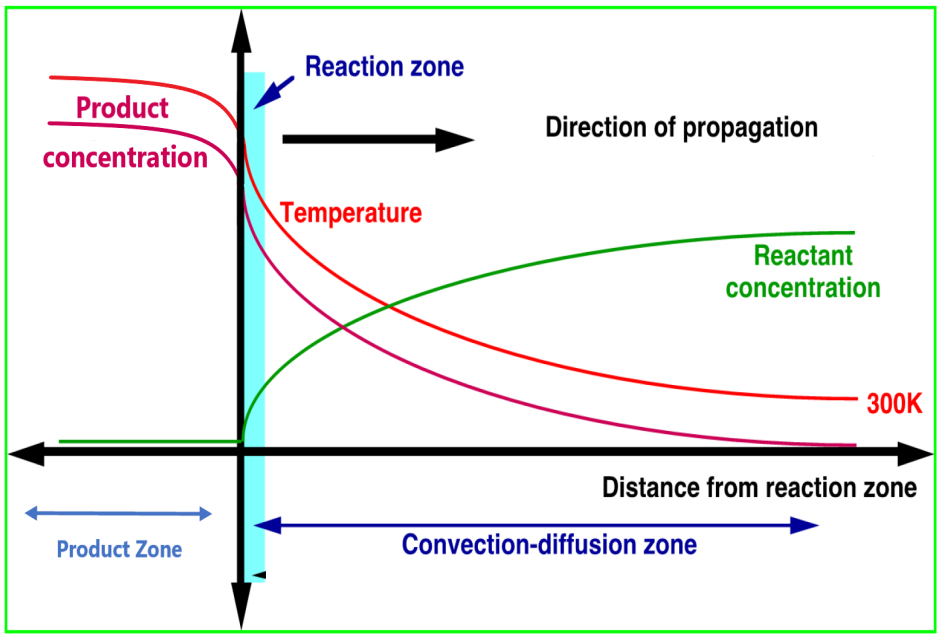

Fig. 2.1 Schematic of a laminar premixed flame structure showing the convection-diffusion (preheat) zone and the reaction zone.

The flame thickness can be defined using the temperature of the burnt gases T_b, the unburnt mixture T_u and the maximum temperature gradient $(|dT/dx|)_{max}$ given by

$$\delta_L = \frac{T_b - T_u}{(|dT/dx|)_{max}} \tag{2.1}$$

In practice, flames have a finite thickness. Nevertheless, it is helpful to identify a well-defined surface within flames. A progress variable c can be used for this purpose, defined as a normalised species mass fraction Y_α

$$c = \frac{Y_\alpha - Y_{\alpha R}}{Y_{\alpha P} - Y_{\alpha R}} \tag{2.2}$$

where the subscripts R and P denote reactants and products, respectively. The value of c goes from zero to unity monotonically on moving from reactants to products. An isosurface of the progress variable can be used as a marker to identify a flame surface. For most simulations, the value of c corresponding to maximum reaction rate is chosen. For hydrocarbon flames, this value is typically ~ 0.8 when a single-step chemical reaction is used. It can range between 0.7 to 0.8 for multi-step chemistry. In high intensity turbulence, the laminar flame

structure may get disrupted, but the reaction zone remains intact and can still be assumed to retain a structure similar to that of a laminar flame. The flamelet assumption is not valid for very high turbulence intensities when the turbulence scales may affect the reaction zone directly [38].

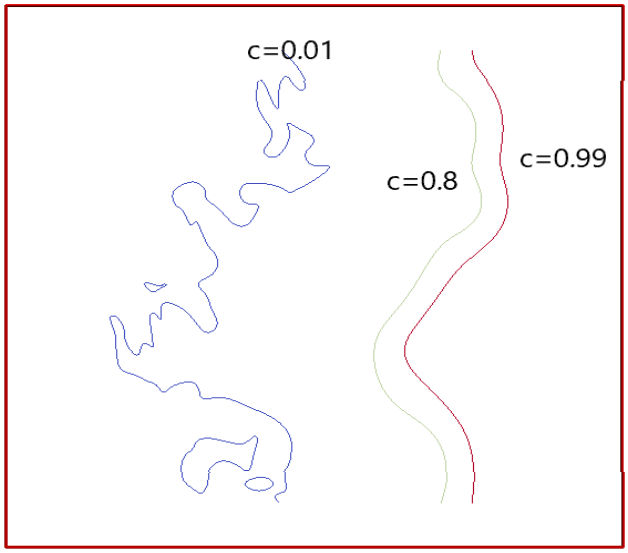

Fig. 2.2 Identification of a flame surface in flames with finite thickness, using isosurface at $c = 0.8$ which approximately represents the surface corresponding to peak reaction rate. The value $c = 0.01$ represents the leading edge of the flame and $c = 0.99$ represents the trailing edge of the flame.

The identification of a flame surface helps to evaluate several properties such as the displacement speed S_d. It measures the normal propagation speed of a flame surface relative to the surrounding mixture. The flow expands and hence, accelerates through the flame, therefore the displacement speed depends on the position within the flame. By choosing an isosurface at a fixed value of c, the expression for S_d can be written as

$$S_d = \frac{1}{|\nabla c|}\frac{Dc}{Dt} \tag{2.3}$$

A more detailed expression of S_d can be used for flame surface modelling (for example in the level-set approach [42]) which is given as [43, 44]

$$S_d = \frac{\dot{\omega}_F + \nabla.[\rho D \nabla c]}{\rho |\nabla c|} \tag{2.4}$$

It must be noted that locally, the wrinkled flame surface behaves like a laminar flame and essentially moves with the same speed as that of a laminar flame. The displacement speed at the location of flame-flame interactions is significantly increased because of the flame acceleration prior to mutual annihilation of flames [15, 28, 29]. Equation 2.4 will be used in Chapter 3 for an analytical analysis of flame acceleration during flame collision and pocket burnout events.

In addition to the displacement speed, the consumption speed s_L of a flame can be defined and it is the rate at which the fuel is consumed by the flame in a domain. For a one-dimensional unstretched laminar flame, s_L is given as

$$s_L = -\frac{1}{\rho_u Y_{u,F}} \int_{-\infty}^{\infty} \dot{\omega}_F(x) dx \tag{2.5}$$

where ρ_u and $Y_{u,F}$ are the unburnt mixture density and fuel mass fraction respectively and ω_F is the reaction rate of the fuel. The typical flame speed for stoichiometric hydrocarbon-air mixtures at ambient conditions ranges from $0.3-0.6$ m/s. Both s_L and δ_L serve as a reference velocity and length scale respectively in many turbulent combustion problems.

2.1.2 Mutual Annihilation of Colliding Flames

The collision of two flame surfaces, called flame-flame interaction, results in mutual annihilation of the two flames [28, 29]. In premixed flames, mutual annihilation is a rapid process preceded by acceleration of the flame immediately prior to the collision. The internal structure of the two flames merges and eventually all the reactants are depleted and the flame quenches. This leads to the destruction of the flame surface area.

Chen and Shorab [28] analysed the mutual annihilation process in one-dimensional methane-air flames. They noted that when the flames were separated by a large distance, they travelled at their characteristic unstrained laminar flame speed s_L. However when the internal structures came closer, their diffusive layers merged leading to moderate acceleration. During the merging of the reaction zones, however, there was rapid acceleration until the flames were completely quenched. They further noted that the Lewis number of the mixture has a significant effect on the acceleration of the merging flames.

Echekki et al. [29] investigated the role of chemistry in a stoichiometric 1-D methane-air flame collision. They attributed the initial acceleration of the flames to the merging of the diffusive layers of individual species, particularly H_2 which diffuses and accumulates within

the reaction zone. The buildup of H_2 was said to enhance the production of radicals, specially the H radical in the reaction zone. In the final stages, the rapid acceleration was attributed to changes in the balance between reaction and diffusion in the reaction zone. In addition, Echekki et al. [29] suggested that in the high curvature regions in a turbulent flame, there is an enhancement in the transport of highly diffusive species such as H_2 and H which could further accelerate the flames before interaction.

2.1.3 Turbulent flames

In turbulent flames, flame-flame interactions arise when these flames become severely wrinkled and self-interactions locally within a flame surface become inevitable. Mutual annihilation of the interacting surface can change the flame surface area [3] as well as the consumption rate of the fuel [15, 45]. In addition, it acts as a precursor to events such as formation of flame pockets which can also affect the overall flame surface area [20]. The frequency of flame-flame interactions depends on the amount of wrinkling of the flame, which in turn is governed by the intensity and length scales of the turbulent flow interacting with the flame.

Turbulence spectrum

Turbulence in a flow results from the growth of instabilities with increasing Reynolds numbers. It is characterised by seemingly random and chaotic three-dimensional vortices, called eddies, which are advected, stretched and eventually break down. Most practical flows are turbulent due to the shearing of the flows caused by walls and mixing layers. A range of length scales of the eddies exist within a turbulent flow, with the large, energy carrying scale being the integral length scale ℓ_0 and the smallest being the Kolmogorov length scale η.

The turbulence intensity u' is the root mean square of the instantaneous velocity at each spatial point. The kinetic energy per unit mass of the turbulent flow can be defined as

$$K = \frac{3}{2}\overline{u'^2} = \frac{1}{2}\left(\overline{u_x'^2} + \overline{u_y'^2} + \overline{u_z'^2}\right) \tag{2.6}$$

Based on the turbulence intensity and integral length scale of turbulence, a Reynolds number can be defined for a turbulent flow as

$$\mathrm{Re_t} = \frac{u'\ell_0}{\nu} \tag{2.7}$$

where ν is the kinematic viscosity.

In a turbulent flow, the kinetic energy cascades down from large scale eddies to small scale eddies. The energy is then dissipated into heat by the action of viscosity. With the help of the Fourier analysis, a mathematical basis for the energy cascade can be determined. For homogeneous and isotropic turbulence,

$$\frac{1}{2}\overline{u_i' u_i'} = \int_0^\infty E(k)dk \tag{2.8}$$

and a typical picture of the energy spectrum is shown in Figure 2.3. Here, k is the wavenumber which goes as $1/\ell$ and $E(k)$ represents the kinetic energy contained in a small range of wavenumber around k.

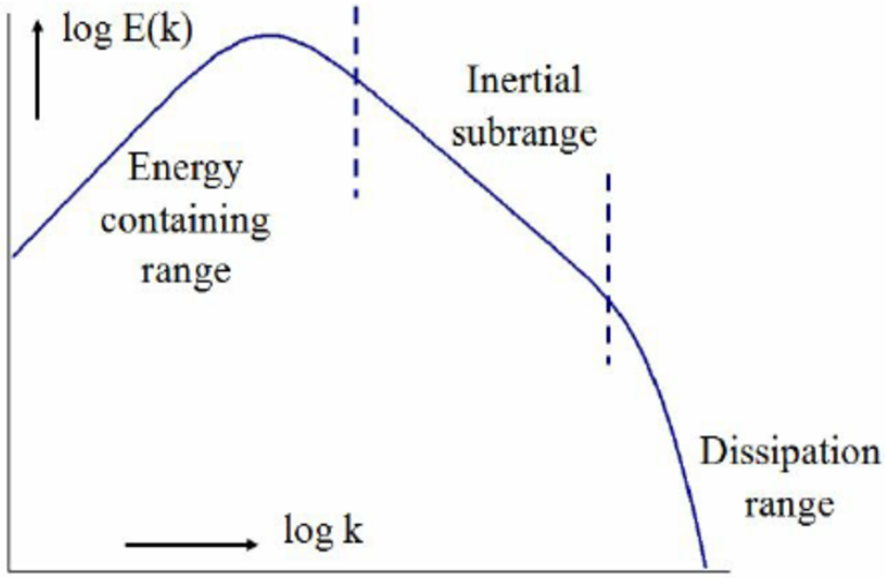

Fig. 2.3 A typical turbulence spectrum showing the energy containing range (integral length scale), the inertial range and the dissipation range (Kolmogorov scales) [46].

The value of $E(k)$ is high at low values of k and vice-versa. It is found that the energy spectrum for higher values of $\mathrm{Re_t}$ is shifted to higher values of k, implying that the smallest eddies become smaller as $\mathrm{Re_t}$ increases. At intermediate values of k, the spectrum is found to decay as $k^{-5/3}$. This range of wavenumber is called the inertial range. For values of k higher than the inertial range, the turbulent kinetic energy gets dissipated due to viscosity [46].

The dissipation of turbulent kinetic energy per unit mass ε is a very important property in turbulent flows. Although dissipation occurs at the smallest scales, its rate is governed by the kinetic energy provided at the largest scales which eventually cascades down to the smallest scales [46]. Dissipation per unit mass, ε for homogeneous isotropic turbulence can then be

defined as

$$\varepsilon \sim \frac{K}{\tau} \sim \frac{u'^3}{\ell_0} \tag{2.9}$$

where τ is the flow time scale associated with the integral length scale ℓ_0.

Dissipation is also very important in combustion since the flame results in high temperatures in the burnt products and also preheating of the reactants immediately ahead of the flame. Since viscosity increases with temperature in gases, the dissipation of turbulence by viscosity is stronger on the product side of the flame (or the trailing edge of the flame) than the reactant side of the flame (or the leading edge of the flame) [41]. This causes a disparity in wrinkling between the leading and trailing edges of the flame and therefore, the flame-flame interaction statistics are expected to differ between these two regions.

Scales of Turbulence

The length scales associated with a turbulent flow play an important role in the analysis of flame-flame interactions. The integral length scales of turbulence are more efficient in changing the flame surface area [14, 47]. The smaller length scales are less efficient in affecting the flame area, but they have high curvature and cause more flame-flame interactions. A summary of the important scales in a turbulent flow is given as follows [46]:

- The larger, energy carrying scale of turbulence is called the integral length scale ℓ_0 and contains most of the kinetic energy of the flow. The timescale associated with these scales is called the eddy turnover time τ. It corresponds to the time it takes for the eddy of size ℓ_0 to make a complete rotation. It is also the timescale over which the larger scales transfer their energy to the smaller scales.

- The smallest scales are called the Kolmogorov scales. These are denoted by η and these are the scales at which the kinetic energy is dissipated by viscous dissipation. The associated timescales and velocity scales are denoted by τ_K and u'_K. The Kolmogorov length, time and velocity scales are given by

$$\eta = (\nu^3/\varepsilon)^{1/4} = \ell_0 Re_t^{-3/4} \tag{2.10}$$

$$\tau_K = (\nu/\varepsilon)^{1/2} = \tau Re_t^{-1/2} \tag{2.11}$$

$$u'_K = (\nu\varepsilon)^{1/4} = u' Re_t^{-1/4} \tag{2.12}$$

- Another length scale of interest in turbulence is the Taylor microscale [46]. The dissipation for isotropic turbulence is given by,

$$\varepsilon = 15\nu\overline{\left(\frac{\partial u_i'}{\partial x_i}\right)^2} \tag{2.13}$$

The Taylor microscale λ_T is defined by

$$\varepsilon = 15\nu\frac{\overline{u'^2}}{\lambda_T^2} \tag{2.14}$$

Flame Wrinkling

In two- or three-dimensional cases, the flames become wrinkled either by the growth of instabilities, for example, by thermo-diffusive imbalance or when the turbulent flow interacts with a planar laminar flame and the flame surface gets strained and curved by the turbulent eddies. A mixture is said to be thermo-diffusively unstable when its molecular diffusivity exceeds its thermal diffusivity, that is,

$$D > \frac{\lambda}{\rho C_p}$$

or the Lewis number

$$\mathrm{Le} = \frac{\lambda}{\rho \mathrm{C_p D}} < 1 \tag{2.15}$$

where λ is the thermal conductivity and ρ is the mixture density. Flame cusps, characterised by the formation of a narrow elongated channel, begin to form [5, 13, 15, 48] as the flame becomes wrinkled and the surfaces in the narrow channel collide. The idea of formation of cusps in flames was introduced by Karlovitz et al. [5] and their dynamics were considered by Zel'dovich [13]. Both analyses focussed on the cusps that are formed by the action of self-propagation of the wrinkled flame surface rather than by the action of flame-flame interactions. Zel'dovich [13] suggested the formation of cusps at high curvature to be the phenomenon that controls the uninhibited growth of flame instabilities. The analysis suggested that because of the high curvature, the tip of the cusp has a high propagation speed which counterbalances the instabilities. It was also suggested that the increase in propagation speed of the cusps was due to the focussing of the heat flux into the fuel. However, since the internal structure of the flame was not considered, the propagation speed of the cusp could not be analysed.

In turbulent flames, the stretching of the flame itself can result in high values of the local curvature $1/R$, where R is the radius of curvature of the flame surface, and therefore result in

formation of the elongated narrow channels. When the curvature of these channels becomes $\sim 1/\delta_L$, i.e., comparable to the flame thickness, it gives rise to flame-flame interactions locally within a flame. The flame structures begin to merge and cusps are formed. Figure 2.4 (left) shows an example of formation of such cusps formed within a simulated turbulent flame [15]. In this figure, blue colour represents the unburnt state and red colour represents the burnt state of the fuel-air mixture. On the right is a schematic of a typical shape of such a cusp.

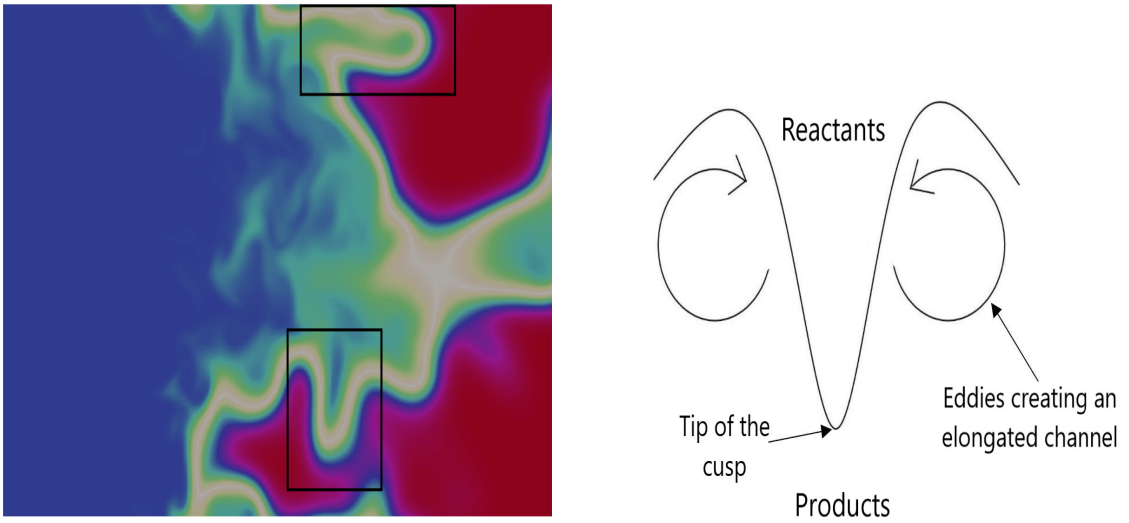

Fig. 2.4 Formation of an elongated channel type cusp in turbulent flames with the left figure showing a snapshot of a species mass fraction profile in a simulated turbulent turbulent flame. Two elongated channel type cusps are marked in this snapshot. The right figure represents a schematic of such a cusp.

Poludnenko and Oran [15] performed simulations specifically to analyse the properties of flame cusps. They initialised two planar flames propagating towards each other at an incline of angle α. When the flames collide on one end, their structure resembles that of a typical cusp found in a turbulent flame (see Fig. 2.4). By changing the value of α, they analysed several different cusps at varying degrees of curvature and their corresponding properties along the centre line. Figure 2.5 shows two different cusps from ref. [15], one at a lower value of α (top) and the other at a higher value of α (bottom). Consequently, the cusp propagates with a velocity higher than the laminar flame speed s_L [15] because of the flame structures merging, which is consistent with the analysis of Chen and Sohrab [28] and Echekki et al. [29] for 1-D flames.

The key finding of this simplified analysis was that for smaller values of α, both the reaction zone and the preheat zone thickens and the tip of the cusp propagates much faster

than the laminar flame speed s_L. For higher values of α, the reaction zone eventually resembles that of a laminar flame. Even so, the preheat zone was still found to be thicker than a typical laminar flame profile. An important conclusion of this analysis was that the cusps burn out rapidly and increase the overall fuel consumption rate locally.

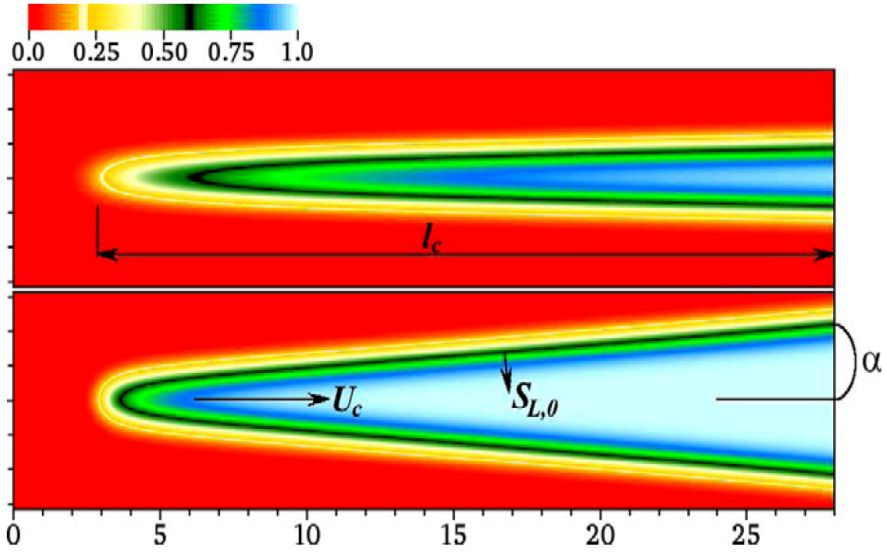

Fig. 2.5 Profile of species mass fraction taken from [15] showing the analysis of a cusp formation through collision of two planar flame sheets, resulting in a cusp at the tip which moves with speed U_c [15]. On the top is a picture of the flames colliding at a smaller incline angle α resulting in a higher curvature cusp. At the bottom the flames collide at a higher value of α resulting in a lower curvature cusp.

Another type of cusp formation at lower curvature can occur in turbulent flames. This is shown in Figure 2.6 (left) with a pocket shaped flame structure. The schematic of such a structure is presented on the right side of this figure. The reactant pocket is formed by an eddy of curvature larger than $1/\delta_L$ with near planar flame-flame interaction at the end of this pocket. When the colliding flame surfaces annihilate each other, an isolated reactant pocket emerges which propagates inwards [20, 23].

The mechanism of pocket formation in a two-dimensional turbulent lean methane-air flame was analysed by Chen et al. [20] using direct numerical simulations (DNS). Pocket formation was shown to occur in three stages: (1) the flame surfaces in highly curved regions come close and collide, result in merging of the reaction zones of the flames in very short timescales, i.e. mutual annihilation [28, 29], (2) recovery of a flame cusp following the mutual annihilation of colliding flame surfaces and (3) formation of an isolated flame pocket as the flame cusp pinches off from the overall flame surface. The reactant pocket thus formed

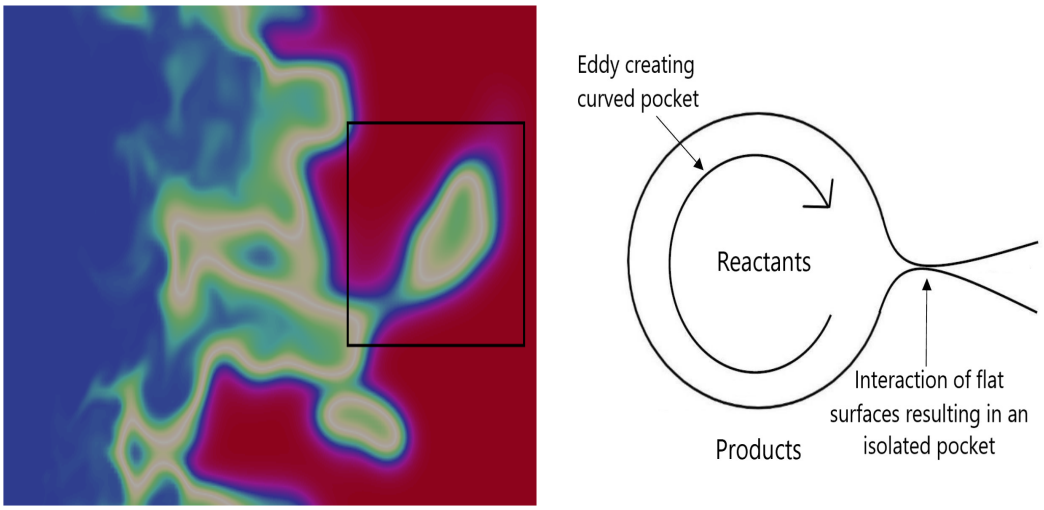

Fig. 2.6 An example of a flame-flame interaction event which leads to formation of a reactant pocket in a turbulent flame. On the left is a pocket formation in a simulated turbulent flame and on the right is the schematic of such a cusp resulting from relatively flat flame surfaces interacting.

burns out rapidly. Another important aspect of this two-dimensional study was that the strain and curvature effects were found to play an important role in pocket formation.

In turbulent flames, the two types of cusps discussed above, namely, the narrow channel type and one which leads to a reactant pocket, frequently occur together. An example of such an event is presented in Figure 2.7. On a close inspection, it can be seen that a reactant pocket is beginning to separate out from the narrow elongated cusp.

The frequency of the flame-flame interactions increases with increasing turbulence intensity and alters the flame surface area [3, 14]. The flame surface area is directly related to the increase in the burning rate for $\ell_0 > \delta_L$ [2], given by

$$\frac{s_T}{s_L} = \frac{A_T}{A_L} \tag{2.16}$$

where s_T is the turbulent flame speed, s_L is the laminar flame speed, A_T is the area of the flame surface and A_L is the cross sectional area of the domain for statistically planar flames. It is assumed that locally the flame structure remains identical to the laminar flame structure and that the flame wrinkling only changes the global consumption rate. The turbulent flame speed s_T can be defined based on the fuel mass consumption rate as

$$s_T = \frac{\dot{m}_F}{\rho Y_{u,F} A_L} = -\frac{1}{\rho_u Y_{u,F} A_L} \int_V \dot{\omega}_F dV \tag{2.17}$$

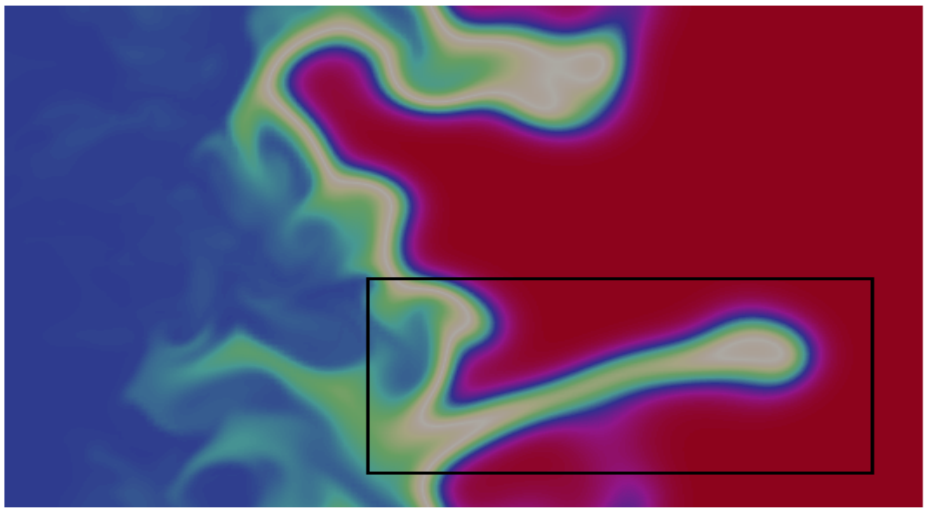

Fig. 2.7 A typical example of a flame cusp found in a turbulent flame consisting of both elongated channel type and reactant pocket type cusps. An elongated channel type cusp can be seen with a reactant pocket beginning to form on one end.

where ρ_u and $Y_{u,F}$ are the unburnt mixture density and fuel mass fraction respectively, $\dot{m}_F$ is the fuel mass flux into the flame, $\dot{\omega}_F$ is the reaction rate of the fuel. In addition to the flame surface area changes, both types of cusp formations discussed above result in rapid consumption of fuel locally within the cusp which itself can alter the overall flame propagation speed [15, 45, 48]. Thus, it follows that the effect of flame-flame interactions on flame propagation is expected to be very significant.

The flame acceleration prior to flame surface collision analysed by Chen and Shorab [28], Echekki et al. [29] and Poludnenko and Oran [15] was based on direct measurement of rate of flame structures merging. For modelling purposes, it is more helpful to analyse these events through differential equations that can be analysed along a flame surface [23, 24]. The concept of flame surface density is used for this purpose.

Flame Surface Density and Flame Stretch

The concept of flame surface density Σ is central to combustion modelling [4, 9, 10, 11]. It is defined as the flame surface area per unit volume, that is

$$\Sigma = \frac{\delta A}{\delta V} \tag{2.18}$$

for an isosurface at $c = c^*$. The surface area of a wrinkled flamelet for this isosurface can be evaluated using the expression

$$A_T = \int_{-\infty}^{\infty} \Sigma \delta(c - c^*) dV \tag{2.19}$$

Flame surface density Σ can also be defined by using the gradient of progress variable [49] using the expression

$$\Sigma = |\nabla c| \delta(c - c^*) \tag{2.20}$$

The balance equation of Σ takes the form [9, 10]

$$\frac{\partial \Sigma}{\partial t} + \frac{\partial}{\partial x_i}(u_i + S_d n_i)\Sigma = \dot{S}\Sigma \tag{2.21}$$

where S_d is the displacement speed of the flame, $\dot{S}$ is the stretch rate and n_i is the flame normal given by

$$n_i = -\frac{\nabla c}{|\nabla c|} \tag{2.22}$$

The flame stretch rate $\dot{S}$ in the Σ equation is defined as the rate of increase of flame area and it contains the contributions of hydrodynamic strain and curvature [6, 7]. Thus, the stretch rate $\dot{S}$ can be defined as

$$\dot{S} = \frac{1}{A}\frac{dA}{dt} = a_T + 2S_d \kappa \tag{2.23}$$

where a_T is the tangential rate of hydrodynamic strain and κ is the mean curvature. The expression for a_T can be given as

$$a_T = (\delta_{ij} - n_i n_j)\frac{\partial u_i}{\partial x_j} \tag{2.24}$$

where δ_{ij} is the Kronecker delta function which is unity when $i = j$ and zero otherwise, and the mean curvature κ is defined as

$$\kappa = \frac{1}{2}\frac{\partial n_i}{\partial x_i} \tag{2.25}$$

The stretching of flames is inevitable in turbulent flows which induce both hydrodynamic straining and curvature. It has been observed that there is generally an overall positive straining of a flame stretched by the action of turbulence, whereas the average curvature of a statistically planar flame is zero [44, 50, 51]. Thus, most studies on stretched flames have

focussed only on strain [37] and the contribution of curvature in flame propagation is often ignored [52]. Negative flame stretch has also been investigated recently by Ruan et al. [53].

However, curvature plays an important role in terms of flame-flame interactions. It can be argued on physical grounds that regions of high curvature will be more likely to undergo flame-flame interactions [3, 20, 23]. Hence, to model flame-flame interactions, a good understanding of flame stretching, and in particular flame curvature is necessary. Flame curvature is also important in defining the flame surface geometry and topology. It can be further decomposed as

$$\kappa = \frac{1}{2}(h_l + h_u) \tag{2.26}$$

where h_l and h_u are respectively the minimum and maximum local principal curvatures by magnitude. The local flame surface geometry can be quantified using the curvature shape factor, defined as $S_h = h_l/h_u$ and is constrained between -1 and 1. The value of $S_h = -1$ represents the spherical saddle point, $S_h = 0$ represents the cylindrical topology and $S_h = 1$ represents the spherical topology. It is found that cylindrical topology generally dominates over the spherical topology [50, 54].

Flame stretch can also affect the internal structure of the flame [8]. These effects were incorporated by Bray and Cant into a single quantity called the stretch factor I_0 [14, 55]. It is defined as the ratio of local instantaneous propagation speed s_L^* to the untrained laminar flame speed s_L, that is

$$I_0 = \frac{s_L^*}{s_L} \tag{2.27}$$

The quantity I_0 has been found to be ~ 1 for for thermo-diffusively neutral mixtures, i.e., $\mathrm{Le} = 1$ but the value of I_0 deviates from unity for non-unity Lewis number [52, 56, 57] or for very high Ka values [14]. Furthermore, flame stretch also affects I_0 [14]. Based on this, a modified relation between A_T and s_T can be defined as follows:

$$\frac{s_T}{s_L} = I_0 \frac{A_T}{A_L} \tag{2.28}$$

The impact of flame-flame interactions on I_0 is part of the investigation presented in this thesis. The stretch rate $\dot{S}$ generally serves as a production term in the balance equation for Σ. Whether or not it can account for the area destruction within the flame due to flame-flame interaction events remains an open question [37]. An additional term in the Σ equation has been modelled [3, 15, 58] to account for flame-flame interactions but the validity of these models is still uncertain.

Regimes in Turbulent Combustion

The process of wrinkling in turbulent flames depends on the turbulence intensity u' as well as the scales of turbulence. The internal structure of the flame interacts differently with different scales of turbulence. The regimes in turbulent flames are defined based on how the internal flame structure gets affected upon interacting with turbulence [37, 59]. The chemical reaction time scale τ_C, flow time scale or eddy turnover time τ and Kolmogorov time scale τ_K can be defined using flame quantities as follows:

$$\tau_C = \frac{\delta_L}{s_L}; \tau = \frac{\ell_0}{u'}; \tau_K = \frac{\eta}{u'_K}$$

Based on these time scales, some important dimensionless numbers related to turbulent flames can be defined [41].

1. Damköhler number is defined as the ratio of flow time scale to chemical time scale

$$\mathrm{Da} = \frac{\tau}{\tau_C} = \frac{s_L \ell_0}{\delta_L u'} \tag{2.29}$$

2. Karlovitz number defined as the ratio of chemical time scale to Kolmogorov time scale.

$$\mathrm{Ka} = \frac{\tau_c}{\tau_K} = \frac{\delta_L u'_K}{s_L \eta} = \frac{\delta_L u'}{s_L \lambda_T} \tag{2.30}$$

   where λ_T is the Taylor microscale (see Eqn. 2.14). Using scaling parameters, Ka can be redefined as

$$\mathrm{Ka} = \left(\frac{\ell_0}{\delta_L}\right)^{-1/2} \left(\frac{u'}{s_L}\right)^{3/2} \tag{2.31}$$

3. Another Karlovitz number can be defined based on the reaction zone thickness δ.

$$\mathrm{Ka}_\delta = \frac{\delta u'_K}{s_L \eta} = \frac{\delta u'}{s_L \lambda_T} \tag{2.32}$$

   The turbulence Reynolds number (Eqn. 2.7) can be restated using flame quantities as

$$\mathrm{Re_t} = \frac{u'}{s_L} \frac{\ell_0}{\delta_L} \tag{2.33}$$

   Using the above definitions of Da and Ka, $\mathrm{Re_t}$ we get

$$\mathrm{Re_t} = \mathrm{Da}^2 \mathrm{Ka}^2 \tag{2.34}$$

The regimes of turbulent combustion can be defined based on these dimensionless numbers. These regimes are presented in Figure 2.8 in a graph of u'/s_L plotted against ℓ_0/δ_L. The bottom left of the figures represents the region where $\mathrm{Re_t} < 1$, and the flow will remain laminar. The lines showing $\mathrm{Da} = 1$, $\mathrm{Ka} = 1$ and $\mathrm{Ka}_\delta = 1$ are marked in the figure.

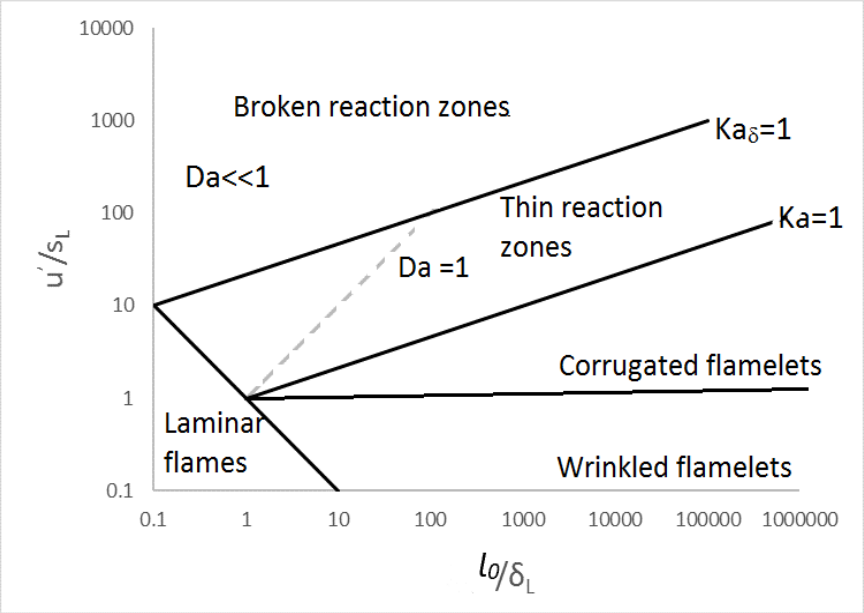

Fig. 2.8 Regime diagram in turbulent combustion based on $\mathrm{Ka}, \mathrm{Ka}_\delta$ and Da. The lines corresponding to $\mathrm{Ka} = 1$, $\mathrm{Ka}_\delta = 1$ and $\mathrm{Da} = 1$ are used to define different regimes [41].

- For $\mathrm{Ka} < 1$, $\mathrm{Da} > 1$ and $u'/s_L < 1$, the chemical length scale, i.e. the flame thickness δ_L, is larger than even the smallest Kolmogorov length scales η. The flame can get moderately wrinkled and this is called the *wrinkled flame regime*.

- For $\mathrm{Ka} < 1$, $\mathrm{Da} > 1$ and $u'/s_L > 1$, the flame thickness remains larger than η but there is strong wrinkling of the flame due to high u'. However, since the turbulence does not penetrate into the flame, the overall effect is a corrugated flame with enhanced surface area but the flame structure remains the same as that of a laminar flame. This is called the *corrugated flame regime*.

- As the turbulence intensity gets higher such that $\mathrm{Ka} > 1$, $\mathrm{Da} > 1$ $\mathrm{Ka}_\delta < 1$, the Kolmogorov scales η become smaller than the flame thickness δ_L. The result is that the large scales strongly wrinkle the flame whereas the small scales now penetrate the flame and therefore cause thickening of the overall flame structure. The reaction zone, however, still remains intact. This is called the *thin reaction zones* regime.

- If $\mathrm{Ka}_\delta > 1$ and $\mathrm{Da} < 1$, the largest scales can now enter the reaction zone and disrupt the reaction zone. In this case, the reaction zone will thicken. This is called the *broken reaction zones* or *well-stirred reaction zones* regime.

Identification of the different regimes serves an important purpose in studying turbulent combustion. Based on the regime, some key modelling issues can be identified. For example, the concept of flamelet is no longer valid in the broken (or well-stirred) reaction zone, while the enhancement of transport by turbulence should be taken into account in the thin reaction zones regime. Experiments and DNS analysis find that the boundaries between the regimes are not well defined. For example, the reaction zone remains intact for values of Da significantly less than unity [60], but the idea behind the theory still remains significant.

Furthermore, these regimes play an important role in analysing flame-flame interactions. There is an important distinction between the occurrence of flame-flame interaction in the corrugated regime and thin reaction zones regime. In corrugated flame regime, all the isosurfaces of progress variable c are parallel to each other throughout the thickness of the flame, whereas in the thin reaction zones regime, the preheat zone of the flame structure gets disrupted by the smaller scales of turbulence. Thus, the isosurfaces are no longer parallel to each other and can self-interact within the flame brush. Figure 2.9 shows a comparison between a set of isosurfaces of c at different values throughout the flame. A slice is presented of the iso-contours of c values between 0.1 to 0.9 with an increment of 0.1. The figure on the top shows the contours of a flame at low intensity turbulence which is very nearly in the corrugated flame regime, whereas that on the bottom shows contours for the flame well within the thin reaction zones regime.

It is evident that in the corrugated regime (Fig 2.9a), the contours remain parallel to each other throughout the thickness of the flame. In the thin reaction zones regime (Fig. 2.9b), however, the contours are not parallel, particularly in the preheat zone of the flame. With increasing turbulence intensity or decreasing size of scales, the eddies penetrate deeper into the flame, and contours will increasingly become non-parallel. This has a significant importance in terms of flame-flame interaction analysis. The interactions in the thin reaction zones regime will not necessarily result from a collision of full flame structures, but individual isosurfaces can curve significantly within the flame and will self-interact with themselves.

The relationship for flame surface area and flame speed given in Eqn. 2.16 is only valid in the corrugated flame regime. In the broken reaction zones regime when the integral scale ℓ_0 becomes smaller than δ_L, Damköhler's second hypothesis can be used to determine the flame speed according to

$$s_T/s_L = \left(1 + \frac{D_T}{D}\right)^{1/2} \tag{2.35}$$

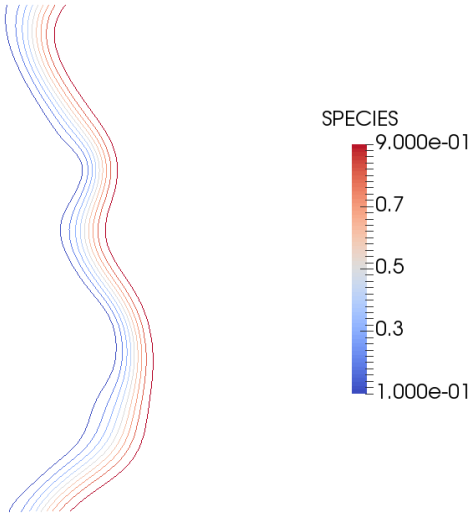

(a) Low u' representing corrugated flame regime

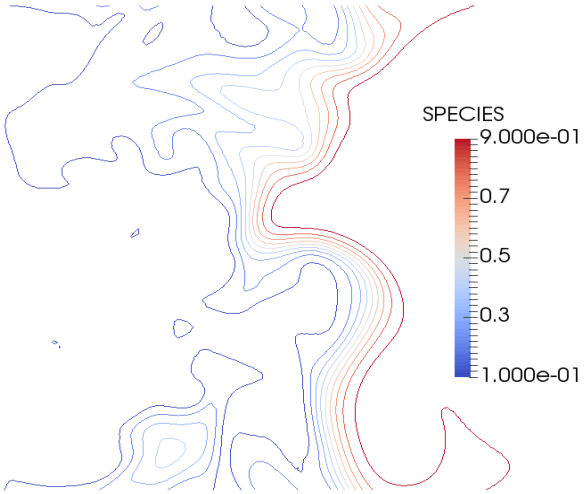

(b) High u' representing thin reaction zones regime

Fig. 2.9 Iso-contour slices of c showing $c = 0.1$ to 0.9 at an increment of $c = 0.1$: (a) shows parallel isosurfaces for low u' representative of corrugated regime whereas (b) shows disrupted isosurfaces at the leading edge for high u' in the thin reaction zones regime

Here, D_T is the turbulent diffusivity, i.e. the effective diffusivity due to turbulent transport. In the thin reaction zones regime, ℓ_0 remains larger than δ_L and the small scales can become smaller than δ_L [4]. In that case, s_T may be estimated from [61]

$$s_T/s_L = \frac{A_T}{A_L}\left(1+\frac{D_T}{D}\right)^{1/2} \tag{2.36}$$

consisting of enhancement due to both flame surface area and turbulent diffusivity D_T. This will be of particular interest in flame-flame interaction analysis since in the thin reaction zones regime, the isosurfaces of the progress variable can self-interact within the flame brush. It can be hypothesised that these interactions result in the enhancement of the turbulence transport D_T which will be discussed in detail in Chapter 5.

2.2 Numerical Simulations of Turbulent Combustion

The central idea of Computational Fluid Dynamics (CFD) is to solve the equations that govern flows (reactive or non-reactive) and for turbulent flows, simulation methods such as Reynolds Averaged Numerical Simulations (RANS), Large Eddy Simulations (LES) and Direct Numerical Simulations (DNS) are used. These equations are derived from a basic concept of conservation of mass, momentum and energy. The equations are complex differential equations that can not be solved analytically except for very specific simple cases. Reacting flows require additional knowledge of the chemical species and their balance equations.

2.2.1 Governing Equations

The equations that govern reacting flows are the continuity equation, the Navier-Stokes equations, and the conservation equations for energy and species mass fraction.

Conservation of mass - Continuity Equation

$$\frac{\partial}{\partial t}\rho + \frac{\partial}{\partial x_k}\rho u_k = 0, \tag{2.37}$$

Conservation of Momentum - the Navier-Stokes equations

$$\frac{\partial}{\partial t}\rho u_i + \frac{\partial}{\partial x_k}\rho u_k u_i = -\frac{\partial}{\partial x_i}p + \frac{\partial}{\partial x_k}\tau_{ki}, \tag{2.38}$$

where the viscous stress tensor is given by

$$\tau_{ki} = \mu\left(\frac{\partial u_k}{\partial x_i}+\frac{\partial u_i}{\partial x_k}\right) - \frac{2}{3}\mu\frac{\partial u_m}{\partial x_m}\delta_{ki}, \tag{2.39}$$

Equations for the conservation of energy have various forms in terms of enthalpy, entropy, internal energy and temperature. The internal energy form is given as

$$\frac{\partial}{\partial t}\rho E + \frac{\partial}{\partial x_k}\rho u_k E = -\frac{\partial}{\partial x_k}pu_k - \frac{\partial}{\partial x_k}q_k + \frac{\partial}{\partial x_k}\tau_{km}u_m + \dot{q}_R, \tag{2.40}$$

while the caloric equation of state provides the definition of the stagnation internal energy as

$$E = \sum_{\alpha=1}^{N} Y_\alpha h_\alpha - \frac{P}{\rho} + \frac{1}{2}u_k u_k \tag{2.41}$$

where the enthalpy of species α is defined as

$$h_\alpha = \int_{T_0}^{T} C_{p\alpha} dT + h_\alpha^0, \tag{2.42}$$

in which $C_{p\alpha}$ is the mass–based specific heat capacity of species α and h_α^0 is the species enthalpy at the reference temperature T_0. In the energy equation (2.40), the quantity q_k is the heat flux vector, while the quantity $\dot{q}_R$ is a radiation heat transfer term.

Conservation of mass fractions of the species is given by

$$\frac{\partial}{\partial t}\rho Y_\alpha + \frac{\partial}{\partial x_k}\rho u_k Y_\alpha = \dot{\omega}_\alpha - \frac{\partial}{\partial x_k}\rho V_{\alpha,k} Y_\alpha. \tag{2.43}$$

Here $\dot{\omega}$ rate of production of species α and Y_α is the species mass fraction given by

$$Y_\alpha = \frac{m_\alpha}{m} \tag{2.44}$$

where m_α is the mass of species α, m is the total mass, and V_α is the diffusion velocity of the species α.
Also, the species mass fractions must satisfy

$$\sum_{\alpha=1}^{N} Y_\alpha = 1 \tag{2.45}$$

while the diffusion velocities must satisfy

$$\sum_{\alpha=1}^{N} \rho V_{\alpha,k} Y_\alpha = 0. \tag{2.46}$$

It must also be noted that by adding all the species equations, the continuity equation must be recovered.
Finally, the thermal equation of state is

$$p = \rho R^0 T \sum_{\alpha=1}^{N} \frac{Y_\alpha}{W_\alpha} \tag{2.47}$$

where R^0 is the universal gas constant.

There could be hundreds or thousands of species and reactions within a flame. Thus, the number of equations to be solved can be very large. In addition, quantities like C_p, enthalpies, entropy all differ for different species and will vary with temperature. Data have been tabulated for these quantities at different temperatures for different species.

Simplifications can be made by assuming reduced chemistry with fewer species, constant values of properties like C_p, constant molecular weight and simplified transport properties. These simplifications make it possible to compute a flame numerically in low order codes for RANS and LES at a much more convenient cost and still manage to give fairly accurate results. However, care must always be taken when using such assumptions. With the availability of much more powerful computers, it is becoming possible to carry out DNS to get accurate solutions with fewer underlying assumptions.

2.2.2 Chemical Kinetics

For a reaction mechanism involving N species and M steps, the chemical reaction can be represented by

$$\sum_{\alpha=1}^{N} \nu'_{\alpha,m} \mathscr{M}_\alpha \rightarrow \sum_{\alpha=1}^{N} \nu''_{\alpha,m} \mathscr{M}_\alpha, \quad m = 1, \ldots, M \tag{2.48}$$

Here, $\nu'_{\alpha,m}$ and $\nu''_{\alpha,m}$ are respectively the reactant and product stoichiometric coefficients of species α for reaction m and $\mathscr{M}$ represents the chemical symbol of species α. The chemical production rate $\dot{\omega}_\alpha$ for species α with molecular weight W_α is expressed as

$$\dot{\omega}_\alpha = W_\alpha \sum_{m=1}^{M} \left(\nu''_{\alpha,m} - \nu'_{\alpha,m}\right) k_m(T) \prod_{\beta=1}^{N} c_\beta^{\nu'_{\beta,m}}. \tag{2.49}$$

The specific reaction rate coefficient $k_m(T)$ is given by the Arrhenius expression

$$k_m(T) = A_m T^{n_m} \exp\left(-\frac{E_m}{R^0 T}\right) \tag{2.50}$$

where E_m is the activation energy, n_m is the temperature exponent and A_m is the pre-exponential factor for reaction m. The concentration c_β of species β is related to mass fraction by

$$c_\beta = \frac{\rho Y_\beta}{W_\beta}. \tag{2.51}$$

For the reaction rates the compatibility condition is

$$\sum_{\alpha=1}^{N} \dot{\omega}_\alpha = 0. \tag{2.52}$$

2.3 Thesis Objectives

This thesis serves to further the knowledge on flame-flame interactions in premixed turbulent flames which remains very limited in the current literature. This is done in several steps that are outlined below.

- Firstly, this work aims to identify the interactions between isosurfaces of progress variable c in a turbulent flame. Numerical tools based on Morse theory of critical points have been developed by Griffiths et al. [21] for this purpose. These tools are used to analyse the location and the local topology of flame-flame interaction events.

- After identification of the isosurface interaction topology, the overall impact on the dynamics of the flame needs to be explained. The surface density function equation is used as the framework for the mathematical analysis of individual topologies that exist when flames collide.

- The frequency of occurrence of isosurface interactions and their corresponding topology for a hydrocarbon flame is analysed. To do this, datasets are created using the Direct Numerical Simulation (DNS) method. Twin premixed flames based on single–step chemistry, propagating towards each other in a homogeneous isotropic turbulence are set up. All possible topologies for the isosurface interaction are evaluated for this dataset and the results are compared with the results of Griffiths et al. [21] for hydrogen-air flames.

- Parametric studies are performed on hydrocarbon flame datasets looking at the effect of varying intensities and scales of turbulence. Based on obtained results, the impact of isosurface interactions on overall flame propagation is assessed. Factors other than the frequency of occurrence of the total interactions are taken into account.

Chapter 3

Theory of Isosurface Interactions: Topology and Flame Dynamics

The literature reviewed in the previous section helps to understand some of the important concepts related to turbulent combustion such as flame stretch. While the theory of flame stretch sufficiently describes the flame area increase caused by straining and curvature, it does not account for flame area changes due to flame-flame interactions. These interactions lead to phenomena such as cusp formation and pocket burnout that can have a significant effect on flame area. Therefore, it is important not only to identify the flame-flame interactions, but also to study their effect on flame propagation properties.

The occurrence of flame-flame interactions can be studied with the help of Morse theory of critical points [34]. According to this theory, the critical points are defined as the points on a surface at which the gradient is either zero or does not exist. A flame surface can be characterised with the help of a reaction progress variable c, restated here as

$$c = \frac{Y_\alpha - Y_{\alpha R}}{Y_{\alpha P} - Y_{\alpha R}}$$

An isosurface of c is used as a marker for the flame surface. When the two flame surfaces interact, the gradient of the progress variable c at the point of interaction of the isosurfaces of c becomes zero. By definition, such points at which $\nabla c = 0$ are called critical points.

Two different aspects of Morse theory [34] are considered here. The first part of this chapter deals with capturing isosurface interactions by first identifying the critical points and then evaluating the local topology around them. The quantities and statistics presented in this and later chapters for isosurface interactions conditioned on c corresponding to maximum reaction rate can be interpreted to be those for flame-flame interactions. The numerical tools to apply the critical point method were developed by Griffiths et al. [21] and these

were applied to the Hawkes et al. [35] DNS dataset consisting of co-flowing H_2-air flames under shear generated turbulence to evaluate the frequency of occurrence of each individual topological event. Two separate datasets at different Damköhler number Da were studied. The topology of flame-flame interactions can be broadly categorised into four principal types called product pockets, reactant pockets, tunnel closure and tunnel formation [19, 21, 36].

The second part of this chapter extends Morse theory to define the values of the progress variable c in terms of scaled coordinates near all four topological events. The equations for the Surface Density Function σ and the displacement speed S_d are expanded in the framework of this theory, and the individual terms in these equations are analysed in depth in the vicinity of the critical points. For the purpose of validating the theory, these terms are then calculated using the Hawkes et al. [35] dataset for the H_2-air flames.

3.1 Flame Topology at Critical Points

The first part of Morse theory defines the flame-flame interaction topology [34]. Taking advantage of the fact that $\nabla c = 0$ at the critical point, the Taylor expansion of c around a critical point located at $\underline{x} = \underline{a}$ is given by

$$c(\underline{a}+\underline{x}) = c(\underline{a}) + \frac{\underline{x}^T}{2}\underline{\underline{H}}(c(\underline{a}))\underline{x} + ... \tag{3.1}$$

Here, $\underline{x}^T$ is the transpose of the vector $\underline{x}$. The Hessian matrix $\underline{\underline{H}}(c)$ contains information on the local topology in the vicinity of critical points. The eigenvalues of the Hessian λ_1, λ_2 and λ_3 give the curvature along the three orthogonal principal axes defined by the corresponding eigenvectors (e_{λ_1}, e_{λ_2}, e_{λ_3}). The eigenvalues define the local topology to second order accuracy in $\underline{x}$.

By using a local spherical coordinate system and taking $\lambda_1 > \lambda_2 > \lambda_3$, shape factors θ and ϕ and mean curvature κ can be derived using the eigenvalues of the Hessian according to

$$\theta = \frac{6}{\pi}\arctan\frac{(\lambda_1 - 2\lambda_2 + \lambda_3)/6^{1/2}}{(\lambda_1 - \lambda_3)/2^{1/2}} \tag{3.2}$$

$$\phi = \frac{2}{\pi}\arctan\frac{(\lambda_1 + \lambda_2 + \lambda_3)\cos(\theta\pi/6)/3^{1/2}}{(\lambda_1 - \lambda_3)/2^{1/2}} \tag{3.3}$$

$$\kappa = (\lambda_1^2 + \lambda_2^2 + \lambda_3^2)^{1/2} \tag{3.4}$$

The shape factors fully define the local topology of the flame surface close to the critical point. Their scaled value ranges from -1 to +1. Figure 3.1 shows all mathematically possible topologies of flame-flame interactions when the values of θ and ϕ vary between -1 to +1. The four general types of topologies identified by Griffiths et al. [21], namely “reactant pocket" (RP) shown in the figure in red background, “tunnel closure" (TC) in pink background, “tunnel formation" (TF) in blue background and “product pocket" (PP) in purple background.

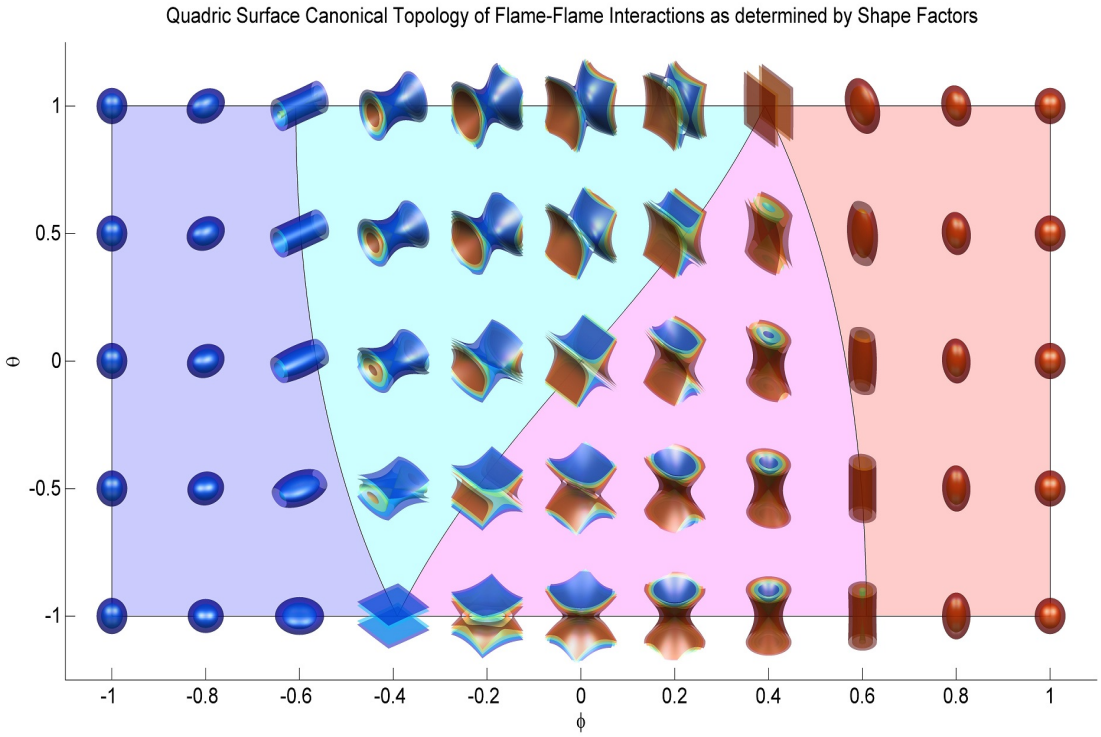

Fig. 3.1 The set of all possible flame–flame interaction topologies as determined by the shape factors [21]. Blue colour represents an unburnt isosurface whereas red colour represents a burnt isosurface.

In Fig. 3.1, blue colour represents a lower value of c and red colour represents a higher value of c. The flame always propagates towards the lower value of c. Reactant pockets are inward propagating spherical pockets with reactants at a lower c value surrounded by burnt products at a higher c value, and are therefore represented by the solid red colour in the figure. Likewise, product pockets propagate outward with burnt products at higher c value in the middle surrounded by unburnt reactants at lower c value. Similarly, tunnel closure involves inward propagation of a topologically cylindrical flame, while tunnel formation involves outward propagation.

3.1.1 Dataset Description

In the original work, Griffiths et al. [21] used the well established DNS dataset of Hawkes et al. [35] generated for two initially planar lean hydrogen–air flames. These flames propagate in a high intensity shear–driven turbulent flow which is created by temporally evolving jet of premixed reactants. The equivalence ratio of the mixture was 0.7 and it was preheated to 700K. A detailed reaction mechanism containing 9 species and 21 reversible reactions was employed [62]. The dataset was produced using the DNS code S3D [63] which employs an 8th order spatial finite–difference scheme and 4th order explicit Runge–Kutta time–stepping. The full dataset involves two different cases run for Damköhler numbers denoted as Da- (Da=0.13) and Da+ (Da = 0.54). The schematic of the simulation setup is shown in Figure 3.2. In the figure, two statistically planar flames represented by the local heat release rate can be seen to be propagating towards each other. The region between the flames contains unburnt reactants in shear generated turbulence.

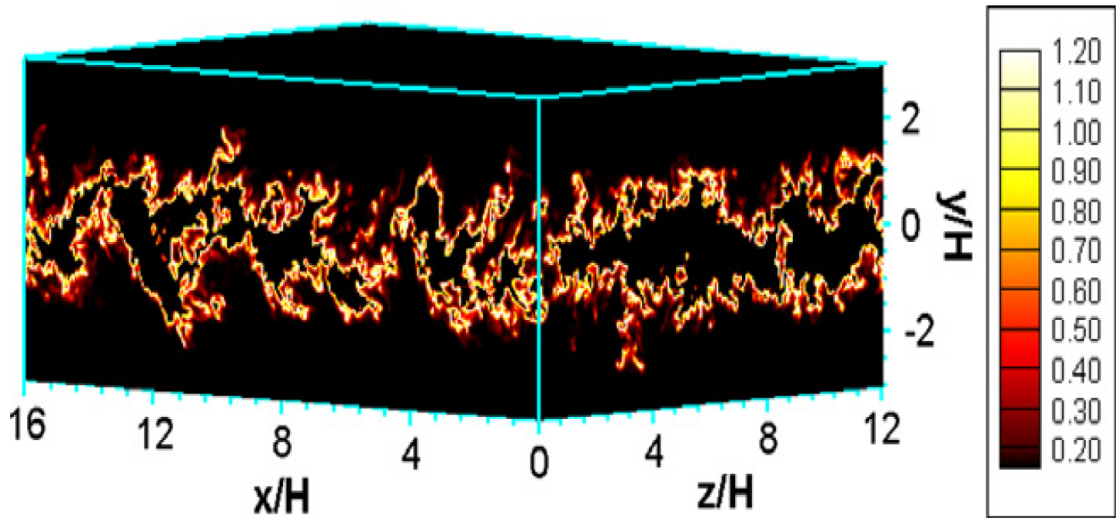

Fig. 3.2 Schematic of the Hawkes et al. [35] dataset showing the two hydrogen flame surfaces propagating towards each other. The surfaces are represented by the local heat release rate for the Da+ case normalised by maximum heat release rate in the laminar flame. Image taken from reference [35].

The computational domain was a cuboid of physical size $16H \times 20H \times 12H$, where H is the width of the slot-jet. This domain was discretised using $2400 \times 1600 \times 1800$ mesh points. The value of H was 5.4mm and 2.7mm and the mesh spacing was 36 μm and 18 μm for the Da+ and Da- cases respectively. The integral length scale was $H/3$ resulting in the value of 1.8mm for the Da+ case and 0.9mm for the Da- case. The smaller mesh size

in the Da- case results in half the domain length in all directions compared to the Da+ case. Boundary conditions were set to be periodic in the streamwise and spanwise directions, with outflow in the direction perpendicular to the flames.

The flames are in the thin reaction zones regime for both cases. In this regime, the smaller scales of turbulence penetrate into the preheat zone but the reactants and products remain separated by a continuous flame surface. No broken reaction zones were observed.

3.1.2 Statistics of Critical Points

A small subset of the full dataset was analysed to evaluate the statistics of the occurrence of critical points. Sufficient critical points were found within this subset for a good statistical result while still keeping reasonable computational cost and memory requirements. The temperature field for this subset is shown in Fig.3.3 for the Da+ case.

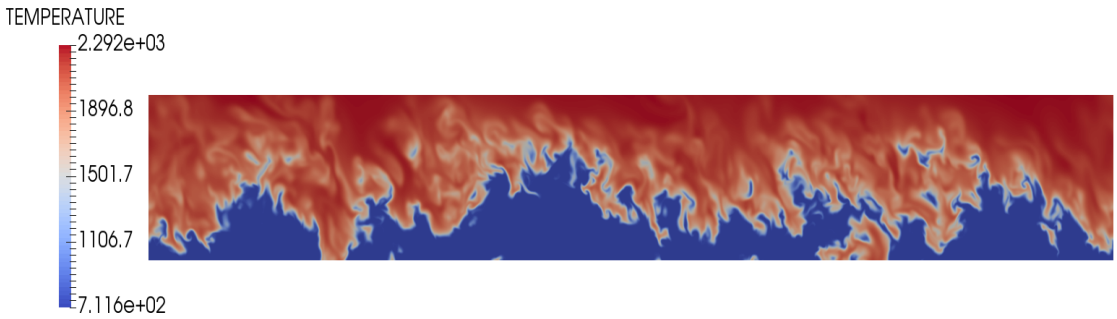

Fig. 3.3 Temperature field of the subset of Da+ dataset from Hawkes et al. [35]

To find the critical points within a cell, tri-linear interpolation on each component of the gradient of the progress variable of the eight surrounding grid points was performed. If the interpolant of each component of the gradient contained zero value, the location of the critical point was deduced by linearising the gradient of the progress variable around each grid point surrounding the critical point. Provided at least one of the eight solutions were found within the cell, the final value of the critical point was calculated using the Newton's method algorithm [64], with the initial solution being provided by the mean of all the feasible solutions. Due to the large domain sizes, various other filtering methods can be applied to locate regions where the probability of finding critical points is high. More details about these steps can be found in reference [21].

Here the progress variable was defined according to Eqn. 2.2 using the mass fraction of H_2. For each of the critical points, the corresponding progress variable value, the coordinates

within the domain and the eigenvalues of the Hessian matrix were recorded. The shape factors were calculated using Equations 3.2 - 3.4. The total number of critical points are presented in the form of histograms plotted against their progress variable value.

The resulting occurrence of critical points for the Hawkes et al. [35] dataset is presented in Fig. 3.4 for both Da+ (left) and Da- (right) cases. It must be noted that the critical points for an entire range of progress variable c are analysed in this thesis. Analysis of flame-flame interactions can be deduced from this data by choosing a specific value of c that provides the best representation of the flame. Only a single snapshot is analysed for both cases. Different colours show the different types of topologies (see legend). The general shape of the histograms differs for the two cases but shows a common trend. Both cases show a significant number of critical points, and hence interactions of isosurfaces of c, at the leading edge of the flame $(0.01 < c < 0.2)$ but their frequency of occurrence decreases in the middle of the flame $(0.2 < c < 0.8)$. Then, there is a resurgence of the number of isosurface interactions towards the trailing edge ($c > 0.8$).

It is also worth noting that the product pocket (PP) and reactant pocket (RP) are spherical events whereas tunnel closure (TC) and tunnel formation (TF) are cylindrical events. It can been seen in the histograms that the cylindrical topological events (sum of TC and TF) occur more frequently than the spherical (sum of RP and PP) events. This is consistent with the findings of Cant et al. [50] in reacting flows and Pope et al. [54] for material surfaces.

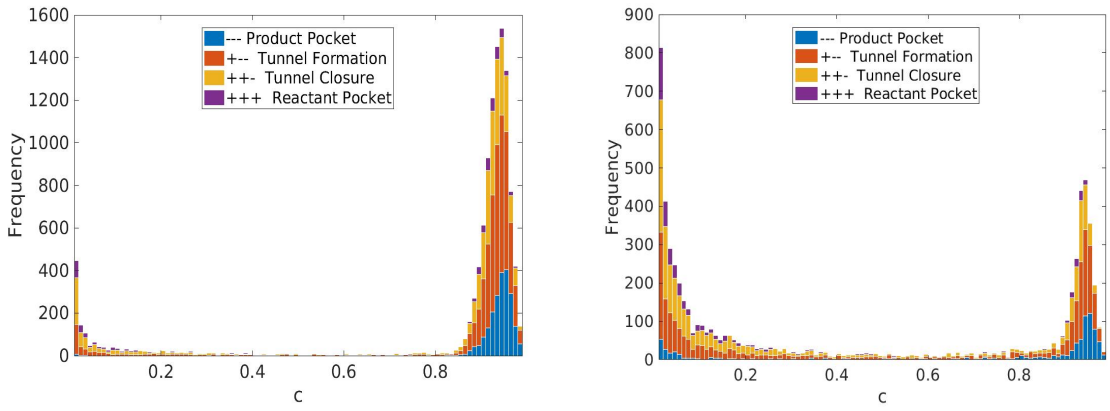

Fig. 3.4 Histograms showing the number of isosurface interactions for Da+ (left) and Da- (right) cases

These histograms are similar to those presented by Griffiths et al. in reference [21] with two exceptions: 1) a progress variable based on H_2 instead of H_2O is used for this analysis because the latter shows an undesirable non-monotonic behaviour towards the trailing edge, and 2) a smaller subset of the Hawkes et al. dataset [35] was used. However, this was still large enough to provide the same general shape of the histograms as in [21]. The

non-monotonicity of progress variable based on the mass fraction of H_2O is demonstrated in Fig. 3.5 showing a 2-D slice of an iso-surface of c based on H_2O at $c = 0.7$. Two almost parallel lines can be seen in the figure, indicating that two surfaces exist for a single value of c and hence, c is non-monotonic . A similar result was seen for various values of c.

Fig. 3.5 Non-monotonicity in H_2O based c shown with the help of a contour slice for $c = 0.7$. Clearly, two surfaces exist for the same progress variable value which indicates that c does not increase monotonically from reactants to products.

The results presented so far summarise the previous literature on this topic developed in [21]. An important point to add into this analysis is that the subdomain for the Da- case is half in length in all of the three dimensions than the Da+ case. Therefore the cross section area in these two cases differs by a factor of four and hence the statistics cannot be directly compared. To make a direct comparison between these cases, the number of interactions is divided by the surface area of the isosurface at $c = 0.5$. The result is presented in Fig. 3.6.

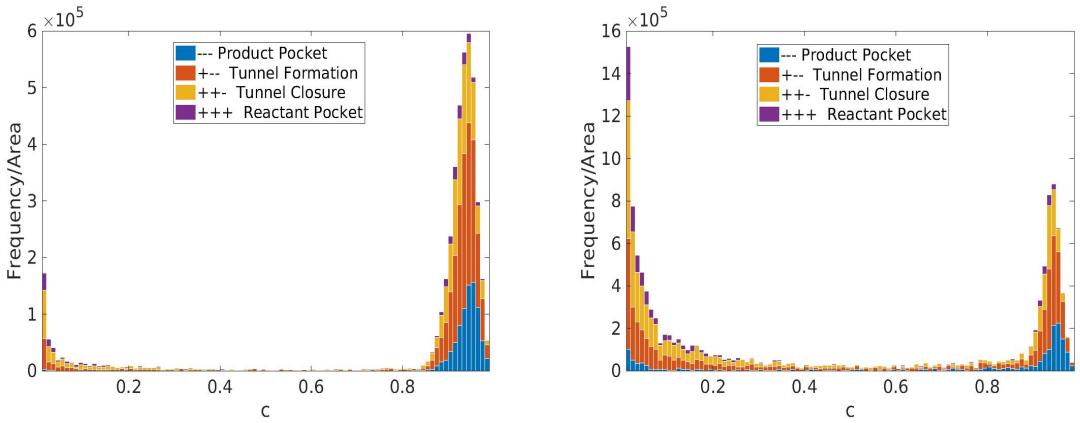

Fig. 3.6 Histograms of the number of isosurface interactions divided by surface area at $c = 0.5$ for Da+ (left) and Da- (right) cases

It is evident from Figure 3.6 that at the trailing edge, the number of isosurface interactions per unit surface area is similar in magnitude for both cases whereas they are larger in magnitude at the leading edge for the Da- case. The reasons for the observed shapes of the histograms as well as the similarities and differences between the Da+ and Da- cases will be explained in more detail in the next chapter. These results will analysed alongside those for hydrocarbon flames to bring out the effects of thermo-diffusive phenomena more clearly. The effect of turbulence on interaction statistics will be analysed for hydrocarbon flames at varying turbulence intensity and turbulence length scales.

Contour slices of various isosurfaces of the progress variable ranging from the leading to the trailing edge of the flame are shown in Figure 3.7 for smaller subsets of the Da+ (top) and Da- (bottom) cases. As discussed in Chapter 2, it is clear that the preheat zone is disrupted by the action of high intensity turbulence. The isosurfaces towards the leading edge are no longer parallel to each other [15, 65] resulting in individual isosurfaces getting wrinkled independently and self interacting locally.

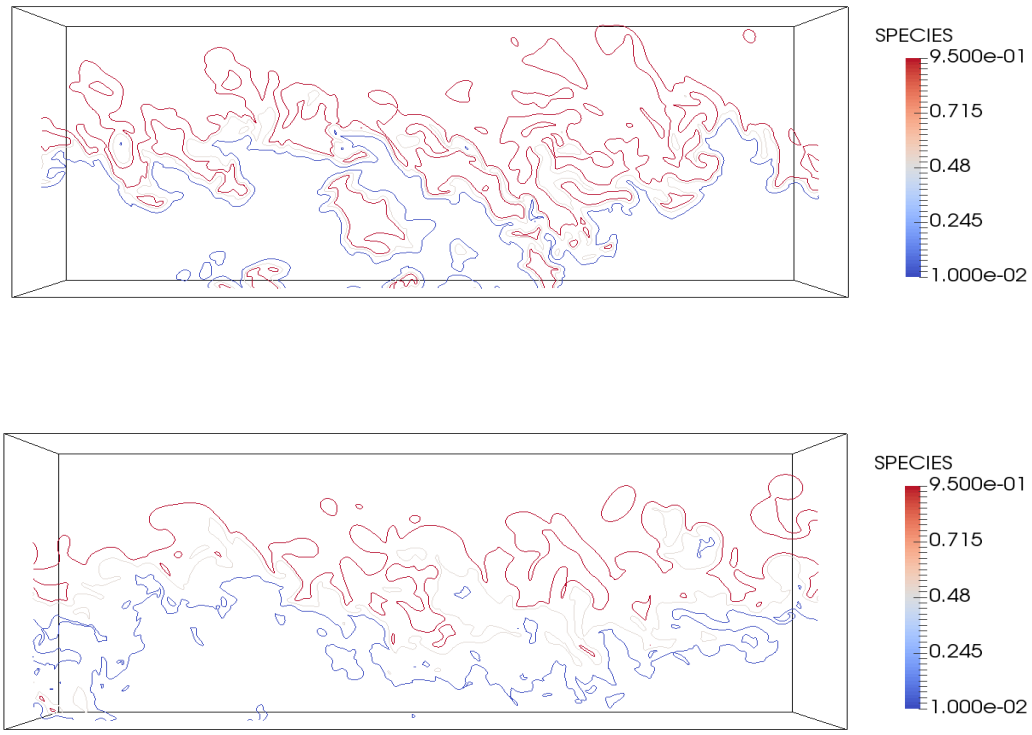

Fig. 3.7 Contour slices of subsets of the Da+ (top) and Da- (bottom) cases showing various isosurfaces of c ranging from the leading edge represented by blue lines to the trailing edge represented by red lines.

3.2 Flame Dynamics at Critical Points

The numerical techniques presented in the previous section provide the ability to capture the critical points and to determine the range of possible geometrical configurations of the flame surface. Moreover, it provides the relative frequency of occurrence of the individual topological events. In this section, the theory is expanded to incorporate the flame dynamics around these topologies and their possible effect on flame propagation.

Among the most important events in terms of its effect on the total flame surface area is flame pinch–off. This occurs kinematically when two adjacent flame surfaces collide, leading to the occurrence of a critical point and the formation of a pocket. This process has been analysed in detail for the two–dimensional case of a head–on collision and the formation of a pocket of reactants [20, 23]. It was shown that a singularity occurs at the critical point, leading to a rapid recession of the interface during pocket formation. The previous two–dimensional topological approach of Kollmann and Chen [23] is extended using a similar theoretical basis [34] to the much richer topology accessible in three dimensions. It is demonstrated that the theory remains valid in three dimensions despite the additional topological complexity and indeed allows for similar physical conclusions. The results confirm that singular behaviour occurs during three–dimensional pinch–off events, and during the final closure of reactant pockets.

It is evident on physical grounds that tunnel closure may lead to pinch–off and the formation of a reactant pocket. Hence this configuration offers the opportunity to extend the previous two–dimensional analysis to three dimensions, and to gain some insight into the kinematics of the pinch–off event and its effect on flame surface area. The other configurations of interest are also amenable to similar treatment.

The purpose of this section is to analyse the four principal flame configurations previously identified in three dimensions by Griffiths et al [21]. The starting point of this analysis is based on the evaluation of the Surface Density Function (SDF) and expanding its balance equation around different types of critical points. In addition, the displacement speed of the flame is analysed in the vicinity of the critical points. The theory is validated using the Hawkes et al. [35] dataset (Section 3.1.1) for the particular case of reactant pocket formation.

3.2.1 SDF Equation at Critical Points

A reaction progress variable c has been defined previously. A balance equation for c may be written as

$$\rho \frac{\partial c}{\partial t} + \rho u_k \frac{\partial c}{\partial x_k} = \dot{\omega} + \frac{\partial}{\partial x_k}\left(\rho D \frac{\partial c}{\partial x_k}\right) \tag{3.5}$$

where ρ is the density, u_i is the velocity, D is the diffusivity of c and $\dot{\omega}$ is the chemical production rate of c.

The SDF σ is defined as the magnitude of the gradient of c given as

$$\sigma = |\nabla c| \tag{3.6}$$

It can be viewed as the generalised flame surface density Σ which does not depend on a specific isosurface. The flame normal pointing towards the unburnt reactants defined in Eqn. 2.22 is restated here as

$$n_i = -\frac{\nabla c}{|\nabla c|}$$

A balance equation for σ can be extracted from the c-equation, by applying the ∇-operator on Eqn. 3.5 and multiplying it by the the unit normal vector $\underline{n}$. The resulting equation takes the form [23]:

$$\frac{\partial \sigma}{\partial t} + u_k \frac{\partial \sigma}{\partial x_k} = \underbrace{-n_i n_k \sigma \frac{\partial u_i}{\partial x_k}}_{\text{Strain Rate Term}} + \underbrace{n_k \frac{\partial}{\partial x_k}(D\kappa\sigma)}_{\text{Dissipation Term}} + \underbrace{n_k \frac{\partial}{\partial x_k}\left[\frac{w}{\rho} + \frac{n_j}{\rho}\frac{\partial}{\partial x_j}(\rho D \sigma)\right]}_{\text{Kinematic Restoration Term}} \tag{3.7}$$

where $\kappa = \partial n_k / \partial x_k$ is (twice) the curvature of the flame surface. The first term on the right–hand side of this equation describes the surface area production due to the strain rate and is called the strain rate term. The second term is called the dissipation term and it accounts for the diffusive dissipation of the flame surface. The last term is the kinematic restoration term [23] which contains two contributions arising from reaction and from normal diffusion.

Considering only the local topology, it is possible to represent each of the four principal configurations (reactant pocket RP, product pocket PP, tunnel closure TC and tunnel formation TF) for small distances away from the critical point using the lemma of Morse [34]. Placing the point of origin at the critical point, the resulting expressions in terms of the local coordinates x, y and z are:

$$\text{(RP)} \quad c(x,y,z) = c_0 + \frac{1}{2}x^2 + \frac{1}{2}y^2 + \frac{1}{2}z^2 \tag{3.8}$$

$$\text{(PP)} \quad c(x,y,z) = c_0 - \frac{1}{2}x^2 - \frac{1}{2}y^2 - \frac{1}{2}z^2 \tag{3.9}$$

$$\text{(TC)} \quad c(x,y,z) = c_0 - \frac{1}{2}x^2 + \frac{1}{2}y^2 + \frac{1}{2}z^2 \tag{3.10}$$

$$\text{(TF)} \quad c(x,y,z) = c_0 + \frac{1}{2}x^2 - \frac{1}{2}y^2 - \frac{1}{2}z^2 \tag{3.11}$$

where c_0 is the value of the progress variable at the critical point. A reactant pocket by definition corresponds to a local minimum, with a low value of the progress variable in the centre with higher values all around. For this configuration the normal vector is $\underline{n} = (-x/r, -y/r, -z/r)^T$ and the curvature $\kappa = -2/r$, where the radius $r = (x^2+y^2+z^2)^{1/2}$. For a product pocket, which corresponds to a local maximum with a high value of the progress variable in the centre and with lower values all around, the same quantities are given by $\underline{n} = (x/r, y/r, z/r)^T$ and $\kappa = 2/r$.

A tunnel closure corresponds to a local saddle point with a maximum on the central axis of the tunnel (taken here as the x direction) combined with a minimum in the other two directions. The normal vector is $\underline{n} = (x/r, -y/r, -z/r)^T$ and the curvature is $\kappa = -2x^2/r^3$. For tunnel formation, the normal vector is $\underline{n} = (-x/r, y/r, z/r)^T$ and the curvature is $\kappa = 2x^2/r^3$. The values of $\underline{n}$ and κ for different configurations are summarised in Table 3.1. For all four configurations the SDF is given by $\sigma = r$ in the vicinity of the critical points.

Configurations	Cases	
	normal vector	curvature
PP	$(x/r, y/r, z/r)$	$\kappa = 2/r$
RP	$(-x/r, -y/r, -z/r)$	$\kappa = -2/r$
TF	$(-x/r, y/r, z/r)$	$\kappa = 2x^2/r^3$
TC	$(x/r, -y/r, -z/r)$	$\kappa = -2x^2/r^3$

Table 3.1 Normal vector and curvature for the four principal configurations.

For the tunnel closure configuration, it is interesting to examine the behaviour of the last two terms in the SDF balance equation (Eqn. 3.7). The dissipation term can be expanded as

$$n_k \frac{\partial}{\partial x_k}(D\kappa\sigma) = n_k(\kappa\sigma)\frac{\partial D}{\partial x_k} + n_k D\frac{\partial(\kappa\sigma)}{\partial x_k} \tag{3.12}$$

and the two terms in the right–hand side may be evaluated close to the critical point as

$$n_k(\kappa\sigma)\frac{\partial D}{\partial x_k} = -\frac{2x^2}{r^3}\left(x\frac{\partial D}{\partial x} + y\frac{\partial D}{\partial y} + z\frac{\partial D}{\partial z}\right) \tag{3.13}$$

$$n_k D\frac{\partial(\kappa\sigma)}{\partial x_k} = -8D\left(\frac{x^2y^2 + x^2z^2}{r^5}\right) \tag{3.14}$$

In the limit of small r, as the critical point is approached and assuming that $r \sim x, y, z$ as $r \to 0$, the first term (Eqn. 3.13) remains bounded but the second term (Eqn. 3.14) becomes singular,

behaving like $1/r$ for $r \to 0$. This result is consistent with the previous two-dimensional analysis [23].

A similar examination may be carried out for the kinematic restoration term. It may be shown readily that the reactive restoration term remains bounded close to the critical point for all configurations. The normal restoration term may be decomposed into five terms according to

$$\begin{aligned} n_k \frac{\partial}{\partial x_k}\left[\frac{n_j}{\rho}\frac{\partial}{\partial x_j}(\rho D\sigma)\right] &= Dn_k\frac{\partial n_j}{\partial x_k}\frac{\partial \sigma}{\partial x_j} + Dn_k n_j \frac{\partial^2 \sigma}{\partial x_k \partial x_j} + n_k \frac{\partial n_j}{\partial x_k}\frac{\sigma}{\rho}\frac{\partial}{\partial x_j}(\rho D\sigma) \\ &+ n_k n_j \frac{\partial D}{\partial x_k}\frac{\partial \sigma}{\partial x_k} + n_k n_j \frac{\partial}{\partial x_k}\left[\frac{\sigma}{\rho}\frac{\partial}{\partial x_j}(\rho D)\right] \end{aligned} \tag{3.15}$$

All of these terms may be evaluated using the expressions for n_i and σ as stated above. For the tunnel closure configuration, the last three terms remain bounded. The first two terms may be evaluated together as

$$Dn_k\frac{\partial n_j}{\partial x_k}\frac{\partial \sigma}{\partial x_j} + Dn_k n_j \frac{\partial^2 \sigma}{\partial x_k \partial x_j} = 4D\left(\frac{x^2y^2 + x^2z^2}{r^5}\right) + 4D\left(\frac{x^2y^2 + x^2z^2}{r^5}\right) \tag{3.16}$$

Again, in the limit of small r, these terms become singular, behaving like $1/r$ as $r \to 0$. Moreover, together they cancel out exactly with the singular term arising from the dissipation (see Eqn. 3.14). Hence the balance equation for σ remains bounded, and indeed $\sigma \to 0$ in the limit. Again, these findings are consistent with the previous two-dimensional analysis [23]. Similar singular behaviour may be observed in the tunnel formation case.

This mathematical result has an important implication in terms of physical flame behaviour. Any flame pinch–off event is preceded by tunnel closure events and it involves mutual annihilation of the flame surfaces in very short time scales. Any irregularities caused by the singularity in the kinematic term will be balanced by the dissipation of such events, thus keeping a physically realisable flame surface. The overall solution will only remain feasible if the two terms cancel each other out, and as a result, a well-defined flame pocket will emerge after the pinch–off.

In the case of reactant pockets and product pockets, no singularities are observed in the σ equation. This is the case even close to the pocket burnout, therefore the flame surface area remains physically well-behaved for these events.

3.2.2 Displacement Speed at Critical Points

Analysing the σ equation provides an understanding of the flame surface behaviour at the critical points but it does not provide any details about the flame propagation properties. To gain further insight into that, it is worth considering the displacement speed S_d, defined with reference to the right–hand side of the c–equation (Eqn. 3.5), for the topological events at the critical points according to

$$\rho S_d \sigma = \dot{\omega} + \frac{\partial}{\partial x_k}\left(\rho D \frac{\partial c}{\partial x_k}\right) \tag{3.17}$$

The displacement speed may be split into contributions arising from reaction, normal diffusion and curvature according to

$$S_r = \frac{\dot{\omega}}{\rho\sigma}; \quad S_n = -\frac{n_k}{\rho\sigma}\frac{\partial}{\partial x_k}(\rho D\sigma); \quad S_t = -2D\kappa \tag{3.18}$$

The contribution due to normal diffusion may be further decomposed as

$$S_n = -\frac{n_k}{\rho}\frac{\partial}{\partial x_k}(\rho D) - \frac{n_k D}{\sigma}\frac{\partial \sigma}{\partial x_k} \tag{3.19}$$

Evaluation for the tunnel closure configuration indicates that the first term remains bounded. The second term may be combined with the curvature term to yield

$$S_n + S_t = -D\left[\frac{x^2}{r^3} - \frac{y^2}{r^3} - \frac{z^2}{r^3}\right] + 2D\frac{x^2}{r^3} \sim \frac{D}{r} \tag{3.20}$$

which becomes singular as $r \to 0$ provided that D remains non–zero in the limit. Note that the reactive term also becomes singular provided that $\dot{\omega}$ remains non–zero in the limit. Hence the displacement speed is unbounded during tunnel closure.

Similar behaviour is evident in the displacement speed during reactant pocket burnout. The equation for $S_n + S_t$ then becomes,

$$S_n + S_t = D\left[\frac{x^2}{r^3} + \frac{y^2}{r^3} + \frac{z^2}{r^3}\right] + \frac{2D}{r} \sim \frac{D}{r} \tag{3.21}$$

which will be singular as $r \to 0$.

In physical terms, this means that the mutual annihilation of two interacting flames during tunnel closure or the burnout of reactant pockets is a rapid event as evident from the singularity in S_d near critical points. The overall effect is to consume the reactants faster, particularly for inward propagating events, namely tunnel closure and reactant pocket events.

These events then lead to cusp formation and pocket burnout which can alter the flame surface area, and hence the overall flame speed.

The S_d terms can also be evaluated for the PP and TF configurations. However, these events occur due to straining of the flow field. Once these events occur, they expand and their corresponding r increases and eventually the propagation becomes similar to an ordinary flame surface. It is important to note that the quantity $S_d\sigma$ remains bounded in all configurations, and hence both the progress variable equation and the SDF equation remain well-behaved.

3.2.3 Validation using DNS Data

The DNS data of Hawkes et al. [35], previously described in section 3.1.1, is used for validating the theory presented in this section. This analysis has been published by Trivedi et al. in ref. [24]. The reaction progress variable used in this analysis is defined based on O_2 mass fraction according to

$$c = \frac{Y_{O_2,R} - Y_{O_2}}{Y_{O_2,R} - Y_{O_2,P}} \tag{3.22}$$

The progress variable gradient is used to evaluate quantities such as the flame normal $\underline{n}$, curvature κ and SDF σ. Hence it is possible to evaluate the terms of the SDF balance equation, and especially the dissipation and kinematic restoration terms in the vicinity of each critical point (see Eqns. 3.12 and 3.15). Similarly, it is possible to evaluate the different contributions to the displacement speed. The choice of progress variable based on O_2 is made in consideration of the data provided by Hawkes et al. [35] at the time of the analysis. It must be noted that the theory should be valid near the critical points regardless of the choice of progress variable. The validation of the σ equation is performed for tunnel closure events whereas reactant pocket burnout events are analysed to validate the displacement speed equations.

Tunnel closure

Several small subsets were separated from the entire Da+ dataset on the basis of high frequency of occurrence of the tunnel closure events. Of these subsets, those that resulted in a flame pinch–off were selected for the analysis. These subsets range in domain size from 30 points cubed to 80 points cubed. Each subset was scanned to find all the critical points, and each critical point was classified according to the analysis of Griffiths et al. [21]. Critical points with the tunnel closure topology were selected for further analysis.

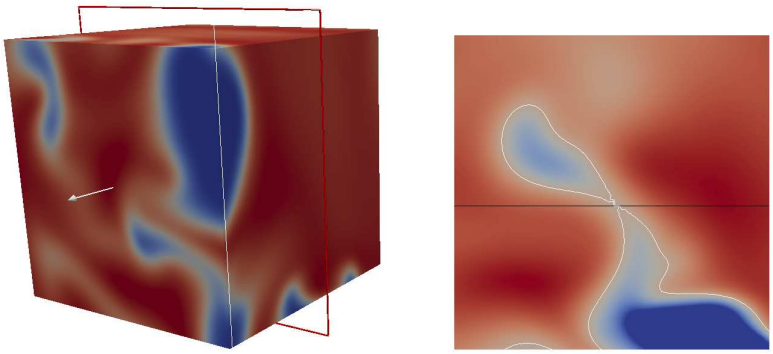

Fig. 3.8 Example of a tunnel closure event. Colour scale runs from blue in reactants to red in products.

To overcome the difficulty of dealing with an extremely complicated three–dimensional topology, a 2-D slice was selected out of the 3-D subdomain showing a clear pinch–off leading to the formation of a reactant pocket. This is shown in Figure 3.8. A DNS mesh line that passes closest to the critical point is carefully chosen and the dissipation and kinematic restoration terms were evaluated along this mesh. This procedure avoids the need for interpolation, and allows all of the quantities to be evaluated directly from the DNS data. Both terms were then compared with the theory in Section 3.2.1. It should be noted that the theory is valid only close to each critical point, and that the spatial extent of its validity is not known *a priori*.

Each tunnel closure event was found to have its own and possibly unique large–scale geometry. Four different examples are provided in Fig. 3.9, which shows two–dimensional slices taken close to the critical point (left side) together with the corresponding plots of the dissipation and kinematic restoration terms (right side).

Figure 3.9 shows 2-D slices in the figures on the left side similar to the one shown in Fig. 3.8. The white outlines represent the contour of the progress variable c that corresponds as closely as possible to the tunnel closure event captured on each plane. The straight black lines show the mesh lines along which the kinematic restoration and the dissipation terms were evaluated. Their corresponding values are plotted in the figures in the right columns.

It is clear from the plots in the right column of Fig. 3.9 that both the dissipation term and the kinematic restoration term reach their highest magnitudes in the vicinity of a critical point. Furthermore, the terms form a rough mirror image, having similar magnitudes but opposite signs, thus tending to cancel one another. This result is in good agreement with the theory and also with the two–dimensional DNS results of Kollmann and Chen [23].

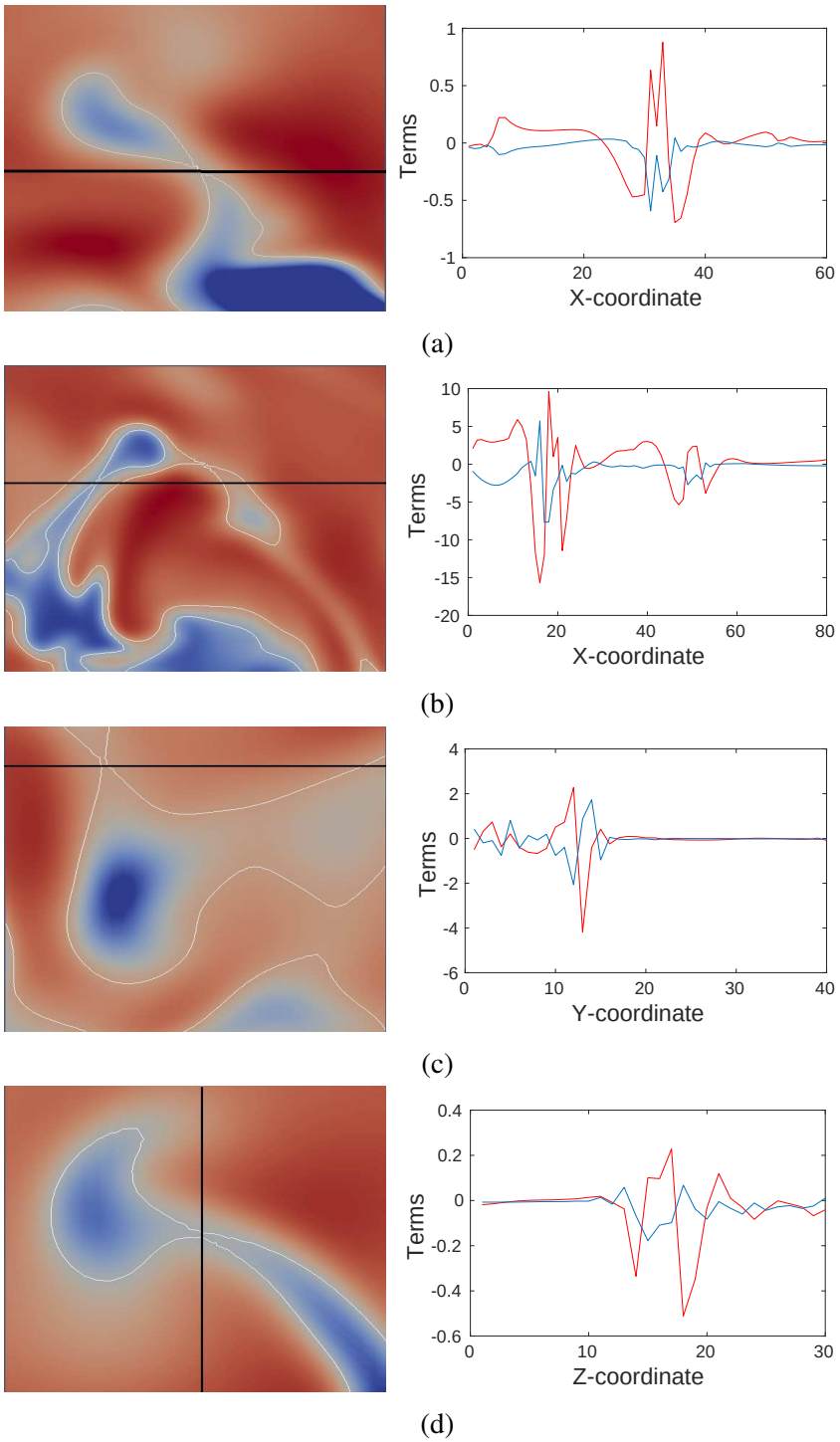

Fig. 3.9 Examples of tunnel closure events (left column) together with (right column) the corresponding SDF equation dissipation term (blue line) and kinematic restoration term (red line).

The lack of complete cancellation between the dissipation and kinematic restoration terms is an indication that the axis of evaluation, i.e. the mesh line, does not pass exactly through the location of the critical point. This is to be expected, since in general the critical point location will not lie on a DNS mesh line. Instead, the analysis method identifies the nearest DNS mesh line as the axis of evaluation, and therefore does guarantee that the critical point lies within a minimum distance corresponding to one–half of the DNS mesh spacing. The accuracy of the results can be improved with the help of interpolation within a DNS mesh cell. Nevertheless, the current axis of evaluation appears to be sufficiently close to the critical point and hence provides a reasonable validation of the theory.

There is no specific value to be expected for either the dissipation term or the kinematic restoration term since in general these terms approach singularity close to a critical point. The recorded values depend on how close the mesh line gets to exact location of the critical point. The variations observed for all the cases can be attributed to the complex topology in all three dimensions.

Figure 3.9b shows a different subdomain containing a different tunnel closure event. Again, the same terms were evaluated along a line passing through the approximate location of the critical point. In this case it can be seen that there are two locations of interest on the same line. Once again, both dissipation and kinematic restoration terms have large magnitudes close to each critical point and the terms tend to cancel each other at both locations.

Figure 3.9c and 3.9d show further subdomains containing different tunnel closure events, with planar views taken in different coordinate orientations. The terms are evaluated along the y-coordinate in Fig. 3.9c and along the z-coordinate in Fig. 3.9d. Again the results are consistent with the theory showing high magnitudes close to the critical point and a tendency to cancel each other.

It would be desirable to carry out a more complete statistical survey of the available critical points in order to confirm the generality of the results. This would be a major undertaking due to the large number of tunnel closure events, as well as the variety of scales, orientations and detailed geometrical features that are observed. Development of an automated procedure for this purpose is left to future work.

Reactant pocket burnout

Another subdomain containing a fully isolated reactant pocket was selected to investigate the behaviour of the displacement speed close to reactant pocket burnout. The displacement speed is computed at the isosurfaces near the centre of the pocket, i.e. at $r \to 0$, which behaves as a critical point. Linear interpolation in each coordinate direction is used to

determine the location of the isosurface and the corresponding value of displacement speed. Figure 3.10a shows a slice through a reactant pocket burnout event. Since only a single snapshot is available, S_d is analysed at multiple isosurfaces (white contours) surrounding the critical point during a reactant pocket burnout event.

Figure 3.10b shows the displacement speed S_d plotted against the progress variable. Here the values of S_d have been averaged over each progress variable isosurface. It is clear that S_d takes large values close to the critical point and falls sharply with increasing progress variable. This happens despite the fact that the density decreases for higher isosurface values which will tend to increase their S_d values. These results are consistent with the behaviour expected from theory, as expressed by Eqn. 3.21.

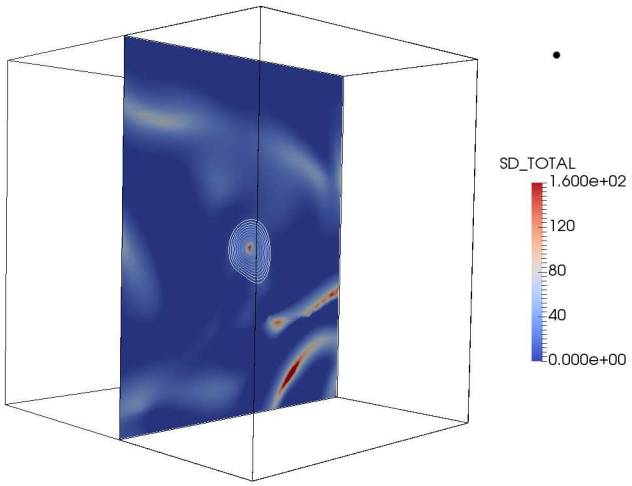

(a)

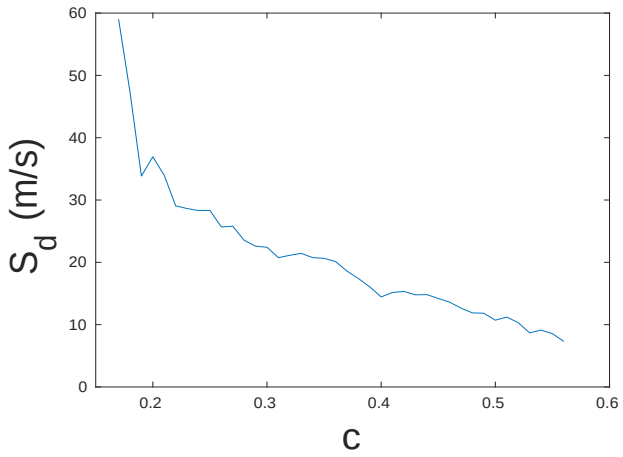

(b)

Fig. 3.10 (a) Progress variable isosurfaces close to a critical point during reactant pocket burnout. (b) Variation of displacement speed S_d close to reactant pocket burnout.

3.3 Chapter Conclusions

This chapter presents the theory developed for understanding flame-flame interactions. Two different aspects of Morse theory are used for this purpose. The first part of this chapter deals with the methodology developed by Griffiths et al. [21] to extract the interactions of isosurfaces of progress variable c and their corresponding topology. These topological events are categorised in four major groups called reactant pockets, product pockets, tunnel formation and tunnel closure. The frequency of these events is computed for the DNS dataset of Hawkes et al. [35] for H_2-air flames. It was found that the majority of interactions interactions are observed towards the leading edge and trailing edge of the flames and very few interactions are recorded in the middle of the flame. It was also evident from this analysis that the occurrence of the cylindrical topologies such as tunnel formation (TF) and tunnel closure (TC) is dominant over the spherical topologies such as reactant pockets (RP) and product pockets(PP).

The second part of the chapter provides an insight into flame behaviour and flame propagation characteristics by solving for the surface density function σ and displacement speed S_d equations in the vicinity of the critical points. This is done by using the lemma of Morse that describes the values of the progress variable c near the critical points in terms of scaled coordinates. It was found that the kinematic restoration term and the dissipation term in the σ equation show singular behaviour for the tunnel formation and tunnel closure events. However, these singularities exactly cancel out, and hence the σ equation remains well-behaved. The S_d analysis on the other hand reveals that all of the flame-flame interaction events result in singularity in S_d values near the critical point.

Flame-flame interactions result in the mutual annihilation of both flames. The tunnel closure events result in flame pinch–off leading to the formation of reactant pockets. The cancellation in singularities between the kinematic restoration and dissipation terms in the σ equation ensures that the flame surface remains well-defined after the pinch–off. Therefore, the flame does not get "punctured" as a consequence of the pinch–off event. These events are important to analyse as they have a significant impact on flame area. Also, the flame-flame interaction events are rapid and result in high values of S_d.

The flame characteristics of the individual events combined with the frequency of the occurrence of each event can be helpful in understanding the role of flame-flame interaction in global flame propagation. The short-term singularities presented in this chapter need further analysis to understand their global effect on the flame properties. This could then be used to build models to account for the effects of change in flame area due to these events.

Chapter 4

Comparison Between Isosurface Interactions in Hydrocarbon and Hydrogen Flames

Previous work by Griffiths et al. [21] focussed on isosurface interactions only in hydrogen flames. However, hydrocarbon fuels are more common in engineering applications, for example, in I.C. engines. The commonly used hydrocarbon fuels have a large number of C and H atoms which results in many intermediate species that undergo a very high number of chemical reactions during combustion. Nevertheless, most premixed hydrocarbon-air fuels burn at similar temperatures and have approximately the same flame thickness and fuel consumption rate. This is important since it allows for the use of simpler chemistry to represent hydrocarbon flames in general.

One of the key differences between hydrocarbon and hydrogen flames is that they have considerably different Lewis numbers Le, given by Eqn. 2.15 and restated here as

$$\mathrm{Le} = \frac{\lambda}{\rho C_p D}$$

Note that in combustion problems, the Lewis number of the deficient reactant is considered. For lean hydrogen combustion, molecular diffusion of highly diffusive species such as hydrogen dominates over thermal diffusion, i.e. $D > \lambda/\rho c_p$, and hence, Le < 1 whereas in case of hydrocarbon flames, Le ~ 1 for methane flames or Le > 1 (Le ~ 1) for lean (rich) heavier hydrocarbon flames. Significant differences in flame behaviour between hydrocarbon and hydrogen flames exist because of the thermo-diffusive instabilities caused by the non-unity Lewis number in lean hydrogen flames [66, 67]. The onset of these instabilities is explained below.

When the flame is positively curved (convex towards the reactants) and Le < 1, the fuel diffuses into the flame faster than the flame loses its heat. Thus, the reaction rate increases and the positively curved flamelet propagates faster than the laminar flame speed, and in the process the flame channel gets elongated towards the reactants. The schematic of this process is presented in Figure 4.1a. The effect of Le < 1 on a negatively curved flamelet (convex towards the products) is shown in Figure 4.1b for which the fuel still preferentially diffuses into the flame but as a result, the mixture becomes leaner in the narrow channel of the reactants. This causes the flame to slow down and the flame channel gets elongated towards the products. Both positively and negatively curved flamelets result in growth of the elongated channels and increase wrinkling. The effect of Le > 1 is exactly the opposite and acts to stabilise the flame, i.e. resist the growth of the elongated channels.

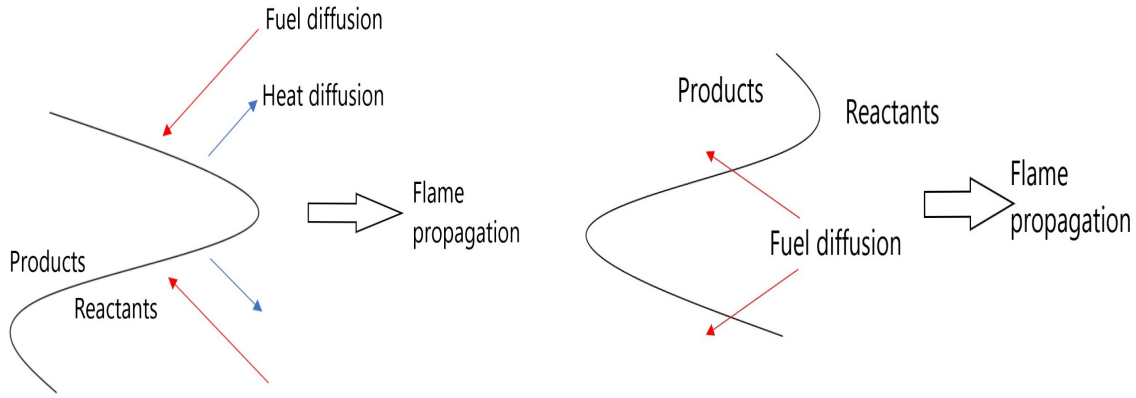

(a) Positively curved flamelet (b) Negatively curved flamelet

Fig. 4.1 Schematic of the thermo-diffusive instability caused by Le < 1. On the left is the positively curved flamelet that propagates faster into the reactants and on the right is the negatively curved flamelet that propagates slower into the reactants. In both cases, the flame channel gets elongated and enhances the wrinkling of the flame.

The Lewis number effects make hydrocarbon and hydrogen flames fundamentally very different from each other and this can have important implications in terms of flame-flame interactions [36]. In hydrogen flames, the thermo-diffusive instabilities wrinkle the flame in addition to the wrinkling caused by turbulence. Therefore, Lewis number effects can change the flame-flame interaction statistics compared to thermo-diffusively neutral (Le $= 1$) or stabilized flames (Le > 1) [36].

In this chapter, the interaction between the isosurfaces of progress variable c are analysed in hydrocarbon-air flames for a twin flame setup. Note that flame-flame interactions can be analysed using this data by choosing an isosurface which is a representative of the flame

(for example, c corresponding to maximum reaction rate). The existence of two colliding flames ensures that there is a sufficient number of isosurface interactions for a good statistical result even for a relatively small sample. These results are compared with those for the hydrogen-air twin flames presented in Chapter 3 and the similarities and differences between these results are discussed. In a later section, the statistics of isosurface interactions in a twin flame setup are compared with those of the single flame. Analysis of the self-interactions in single hydrocarbon flames is provided and the implications on overall flame propagation are discussed.

4.1 Hydrocarbon twin flames

A twin hydrocarbon-air flame dataset was created as part of the present work for comparison with the hydrogen-air flames of Hawkes et al. [35]. In this setup, the two flames within the domain propagate towards each other and eventually collide causing mutual annihilation. This aspect of the dataset is the same as the hydrogen flame of Hawkes et al. [35]. However, because of the limited availability of computing resources, two notable differences exist between these datasets. First, single-step chemistry is used to create the hydrocarbon-air flame dataset. The single-step mechanism is tuned to replicate the propagation properties of a stoichiometric methane-air flame. Despite the simplification, this mechanism allows for an adequate representation of the wrinkling of the flame surface that is essential to study flame-flame interactions. Secondly, homogeneous isotropic turbulence is generated within the domain which differs from the shear-generated turbulence used in Hawkes et al. [35] dataset.

A set of hydrocarbon-air flames were simulated using the DNS code `Senga2` [68]. In this code, the governing equations for the reacting flows are numerically solved in their 3D compressible form with 10th order spatial and 4th order five-stage Runge–Kutta temporal discretisation schemes. Both reduced and detailed chemical schemes are available for hydrogen-air [62] and methane-air [69] combustion. Boundary conditions are set-up using the Navier Stokes Characteristic Boundary Condition (NSCBC) formulation [70]. The initial conditions are described as follows.

4.1.1 Initial Conditions

Turbulence initial conditions

To generate a field of homogeneous isotropic turbulence, the Orszag method [71] is employed, in which a fluctuating velocity field is computed in a cubical domain of length L. The energy

of the fluctuations is computed with the help of the energy spectrum function $E(k)$, where k is the wavenumber vector magnitude in Fourier space.

The spectrum function $E(k)$ used in `Senga2` [68] by default is the Batchelor–Townsend spectrum [72]. The form of the Batchelor–Townsend spectrum is given by

$$E(k) = c_0 \frac{k^4}{k_0^5} \exp\left[-2\left(\frac{k}{k_0}\right)^2\right] \tag{4.1}$$

Here, k_0 is the wavenumber corresponding to the maximum turbulent kinetic energy and c_0 is defined for the initial mean turbulent kinetic energy K_0. Using this spectrum, various turbulence quantities are given as

Turbulent kinetic energy

$$K_0 = \frac{3}{32}\sqrt{\frac{\pi}{2}} c_0$$

Turbulence energy dissipation rate

$$\varepsilon = \frac{15}{16}\sqrt{\frac{\pi}{2}} \pi^2 \nu c_0 k_0^2$$

Longitudinal integral length scale

$$\ell_0 = \frac{1}{\sqrt{2\pi} k_0}$$

Taylor length scale

$$\lambda^2 = \frac{1}{2\pi^2 k_0^2}$$

Kolmogorov length scale

$$\eta = \left[\frac{\nu^2}{\frac{15}{16}\sqrt{\frac{\pi}{2}}\pi^2 c_0 k_0^2}\right]^{1/4}$$

The velocity field can be transformed from the wavenumber space to Cartesian space by performing a Fourier transform. Different statistical realisations of the same velocity field may be obtained by changing the integer seed provided as input to the random number generator.

For the current simulations, the velocity of the turbulent field is initialised in a three-dimensional 5mm cubical domain with 192 uniformly spaced mesh points in each direction (with spacing $\Delta x \simeq 26\mu$m) and is visualised in Figure 4.2. For initialisation of the velocity field, the boundary conditions are set to be periodic in all directions. Using the spectrum parameters c_0 and k_0, the required values of turbulence intensity u' and ℓ_0 can be set. For

the case shown in Fig. 4.2, these values correspond to $u' = 20 s_L$ and $\ell_0 = 2 \times \delta_L$, s_L and δ_L being the unstrained laminar burning velocity ($\sim 39\text{cm/s}$) and flame thickness ($\sim 0.4\text{mm}$) respectively for the stoichiometric methane-air flame.

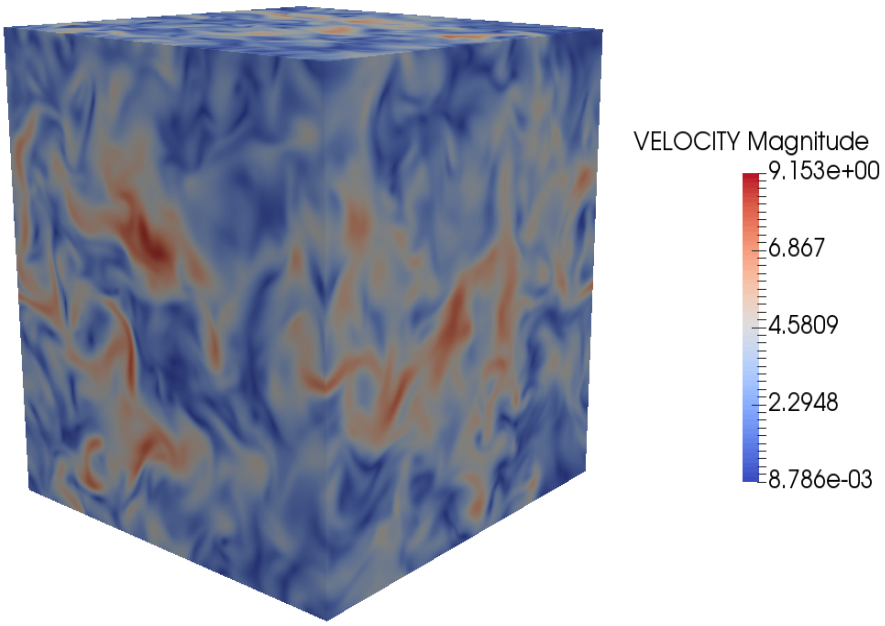

Fig. 4.2 Velocity fluctuations in a cubical box of homogeneous isotropic turbulence

This cubical field of turbulence computed *a priori* is then mapped onto the cuboidal domain. The dimensions of the y-z plane of the domain are kept the same as the cubical homogeneous isotropic turbulence box, i.e. a fixed rectangular cross-section of length $5mm$, which is $\simeq 12\delta_L$. The x-direction is elongated to accommodate the two flames and their wrinkling. The cubical boxes are repeatedly copied along the x-direction until the full length of the domain is covered.

Thermochemical initial conditions

An error-function profile is employed to initialise a one-dimensional laminar flame solution for progress variable c in the $x-$direction, given as

$$c(x;t=0) = \frac{1}{2}\left[1 + \text{erf}\left(\frac{x - x_0}{\delta}\right)\right] \tag{4.2}$$

where x_0 is the location of the centre of the flame profile. Using the progress variable, the mass fraction of the major species may be obtained by:

$$Y_\alpha(x;t=0) = Y_{\alpha,R} + c(x)\,(Y_{\alpha,P} - Y_{\alpha,R}) \tag{4.3}$$

where the subscripts R and P denote the reactants and products respectively. The temperature and density profiles are initialised in the same manner.

A single-step reaction mechanism is used in this analysis in which the chemical reaction formula is simply $R \rightarrow P$ where R is the reactant and P is the product. For this mechanism, the progress variable is simply defined as

$$c = Y_P$$

This scheme preserves the transport and thermal properties of hydrocarbon flames and is a computationally inexpensive and efficient to investigate various combustion problems where the use of detailed chemistry is not necessary.

4.1.2 Dataset Description

Two premixed planar laminar flames are initialised facing each other, with their corresponding normals along the x and $-x$ directions. They are set at distance $\sim 15\delta_L$ apart which allows for a sufficient number of large eddies of size $\ell_0 = 2\delta_L$ between them. The initial temperature and pressure were set as $T_0 = 300$K and $p_0 = 1$ bar respectively. The Lewis number is kept as unity in the current simulations. The schematic of the twin flame setup is shown in Figure 4.3.

The boundaries are set as periodic in the $y-$ and $z-$ directions. Along the $x-$direction, both the $+x$ and $-x$ boundaries are set as outflow to allow for the exit of the expanded burnt products. There is no inflow of fuel in any direction and therefore the flames are only allowed to propagate into the fresh reactants in the middle of the domain. The initial flame profile and turbulence evolve together as the flames propagate towards each other. The planar flames get wrinkled under the influence of turbulence as seen in Figure 4.3.

The initial "fresh" turbulence in the unburnt reactants contained between the two flames primarily drives the flame wrinkling since the turbulence on the product side dissipates rapidly due to enhanced viscosity at high temperatures [41]. Even in the unburnt reactants, the homogeneous isotropic turbulence decays in the absence of a source term [73]. Despite the turbulence decay, the flame carries the memory of the turbulence it has already seen [14] and stays wrinkled for much longer. Eventually, these wrinkled flames collide and this

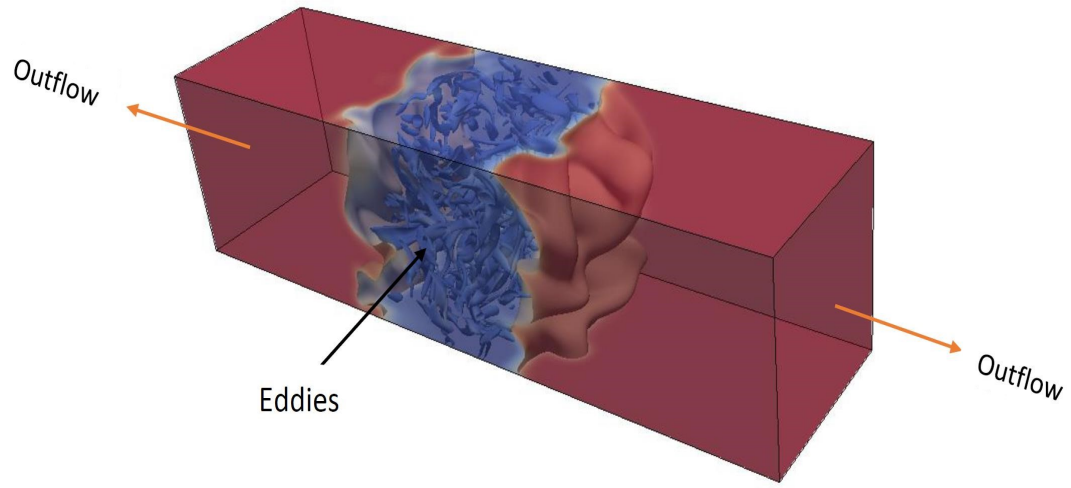

Fig. 4.3 Illustration of the twin hydrocarbon flame setup. Both boundaries are set as outflow. Blue contours in the middle represent the turbulent eddies.

ensures that the isosurface interactions are captured in the domain along with their topology at the point of interaction.

Three different cases were simulated with the turbulence intensity of the initial mixture varied from $u' = 10s_L$, to $u' = 20s_L$ and finally $u' = 40s_L$. The integral length scale ℓ_0 was kept the same for all cases at $\ell_0 = 2\delta_L$. The domain was discretised using a uniform mesh of cubical cells with spacing $\Delta x = 26\mu$m and a fixed timestep $\Delta t = 5ns$ was used in all the simulations. Each simulation was run until the flames had fully interacted, which took a different amount of time for each case. The case with $u' = 10s_L$ fully interacted in $t \simeq 12\tau$ where τ is the eddy turnover time. The higher intensity case at $u' = 20s_L$ took $t \simeq 20\tau$ and the highest intensity case took $t \simeq 30\tau$ to interact fully.

A distinguishing feature of the dataset is that all of the thermo-chemical and physical parameters are maintained constant with the exception of turbulent root-mean-square velocity u'. The Karlovitz number (Eqn. 2.31)

$$\mathrm{Ka} = \frac{u'}{\lambda_T}\frac{\delta_L}{s_L} \sim \left(\frac{u'}{s_L}\right)^{\frac{3}{2}}\left(\frac{\delta_L}{\ell_0}\right)^{\frac{1}{2}},$$

based on the Taylor length scale λ_T increases across the dataset as u' increases. Also recall the Damköhler number (Eqn. 2.29)

$$\mathrm{Da} = \frac{s_L \ell_0}{u' \delta_L}$$

decreases as the u' increases. Some of the important parameters of this dataset along with the dimensionless numbers Ka, Da and Re ($= \mathrm{Ka}^2\mathrm{Da}^2$) are summarised in Table 4.1.

Parameters	u'/s_L		
	10	20	40
ℓ_0/δ_L	2.0	2.0	2.0
η (μm)	26	18	13
Ka	22.36	63.25	178.9
Da	0.20	0.10	0.05
Re	20	40	80
x-length (mm)	30	40	80
Δ x (μm)	26	26	26

Table 4.1 Main parameters of the twin hydrocarbon flame setup.

Figure 4.4 shows the slices of the product mass fraction for this dataset with the turbulence intensity increasing from $u' = 10s_L$ in the top row to $20s_L$ in the middle row and $40s_L$ in the bottom row. The length of the domain in the x direction varies for each case to keep the flames sufficiently distant from the boundaries. Only a small section of the domain is shown here, which is chosen such that it fully contains the two flames. The snapshots from left to right represent flames at after $t = 0$, 5τ and 10τ respectively. The left column shows the initial planar flames which get increasingly wrinkled by the effect of the turbulence as seen in the middle and right columns.

All the cases resulted in an intact, continuous progress variable isosurface at a value corresponding to the peak reaction rate value, i.e. $c = 0.8$. No broken reaction zones were observed. This holds true despite the high values of Ka and low values of Da as seen in Table 4.1. Also noted in the table is that for the $u' = 20s_L$ and $u' = 40s_L$ cases, the Kolmogorov scales are smaller than the mesh spacing Δx. Thus, the turbulence is slightly under resolved. A discussion of the resolution requirements is provided in Appendix A.

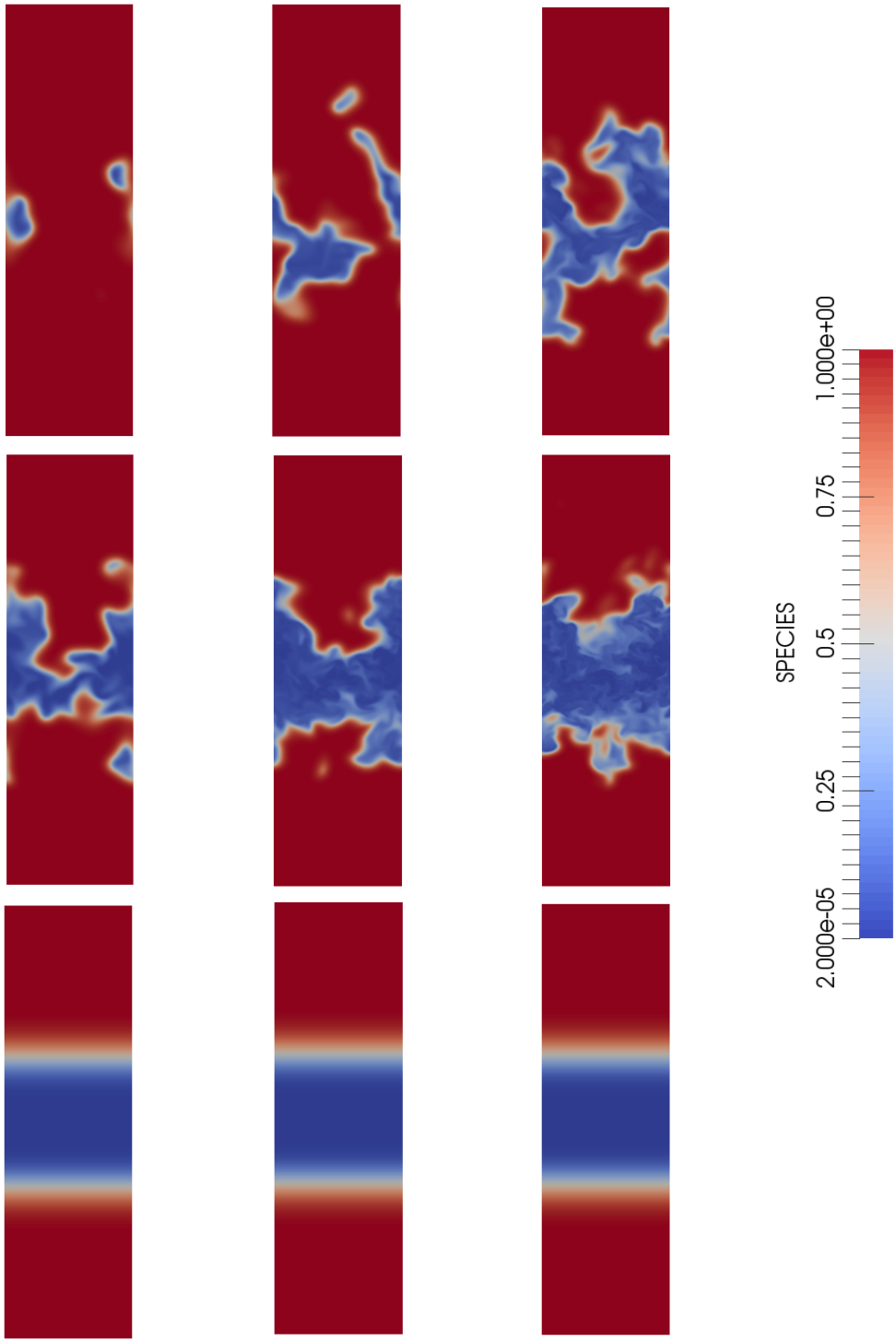

Fig. 4.4 X-Y slices through the 3-D domain of twin hydrocarbon flames at $t = 0,5\tau, 10\tau$ in left, middle and right panels respectively for $u'/s_L = 10, 20$ and 40 cases (top to bottom). The flames can be seen becoming wrinkled and eventually colliding with each other

4.1.3 Critical Point Statistics

The statistics of the occurrence of critical points (or interactions of isosurfaces of c) are evaluated using the numerical tools of Griffiths et al. [21] that were discussed in Chapter 3. The number of flame-flame interactions can be estimated by considering interactions at a carefully chosen isosurface of c which corresponds to the reaction zone. Histograms of the frequency of occurrence of different types of the critical points for hydrocarbon flames are shown in Figure 4.5 plotted against the progress variable c. The individual topologies, categorised as reactant pockets (RP), tunnel closure (TC), tunnel formation (TF) and product pocket (PP) are represented by different colours. The top row in Figure 4.5 shows results for the low turbulence intensity case with $u' = 10s_L$. The middle row results correspond to the $u' = 20s_L$ case and the bottom row results are for the $u' = 40s_L$ case.

The computational domain for the hydrocarbon dataset used for this analysis is much smaller in physical size than for the hydrogen dataset of Hawkes et al. [35]. Thus, analysing a single snapshot may not result in sufficient critical points to obtain a sufficient statistical sample, especially for the $u' = 10s_L$ case for which there are fewer isosurface interactions. To account for this, multiple snapshots are analysed and their results are combined into a single histogram for each of the flames. These snapshots were set $\Delta t = 50\mu s$ apart in physical time. In terms of eddy turnover times τ, this corresponds to $\Delta t = 0.25\tau$ apart for the $u' = 10s_L$ case, $\Delta t = 0.50\tau$ for the $u' = 20s_L$ case and $\Delta t = 1.0\tau$ for the $u' = 40s_L$ case. The combined statistics of all these snapshots are reported until the point at which flames fully annihilated each other.

The number of critical points, and hence the number of isosurface interactions, is found to increase as the turbulence intensity increases. The histograms on the left in Figure 4.5 show the frequency of isosurface interactions for the entire range of the flame, that is, $0.01 < c < 0.99$ and those on the right show the frequency of isosurface interactions for $0.3 < c < 0.99$. This was done because the number of interactions between $0.3 < c < 0.99$ are much fewer than at the leading edge of the flame, and hence, their contribution is not well represented when looking at the histogram showing the entire range of c in the flame.

For all the histograms, the occurrence of isosurface interactions with respect to the progress variable c follows the same pattern. The number of interactions are dominant for $0.01 < c < 0.2$ which can be regarded as the leading edge of the flame. The frequency of isosurface interactions drops as c increases and becomes almost negligible in the range $0.2 < c < 0.8$. Finally, for $0.8 < c < 0.99$ taken as the trailing edge of the flame, there is a rise in the number of isosurface interactions compared to that in the middle, but the number of trailing edge interactions remains much smaller than the number of leading edge interactions.

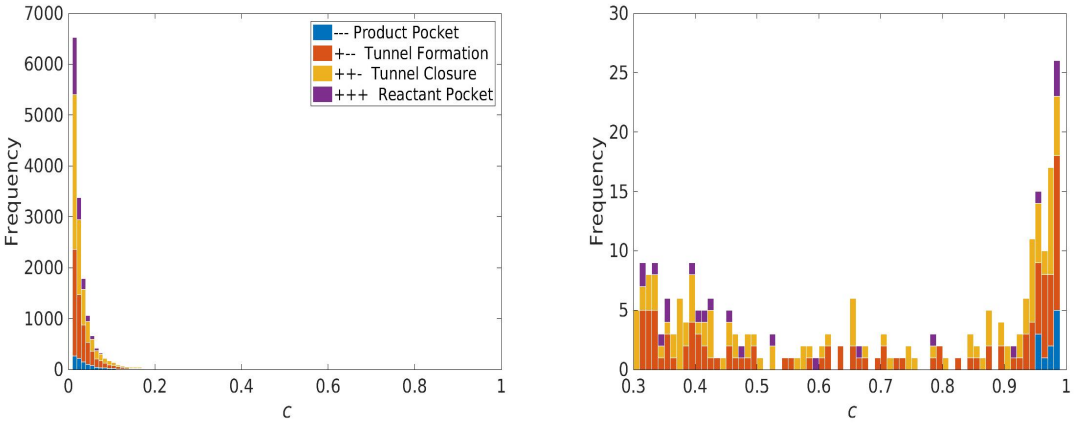

(a) $u'/s_L = 10$

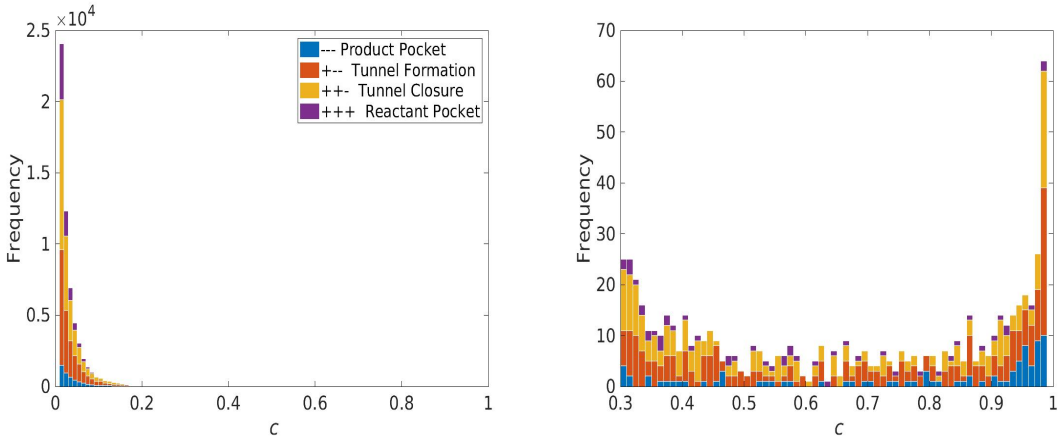

(b) $u'/s_L = 20$

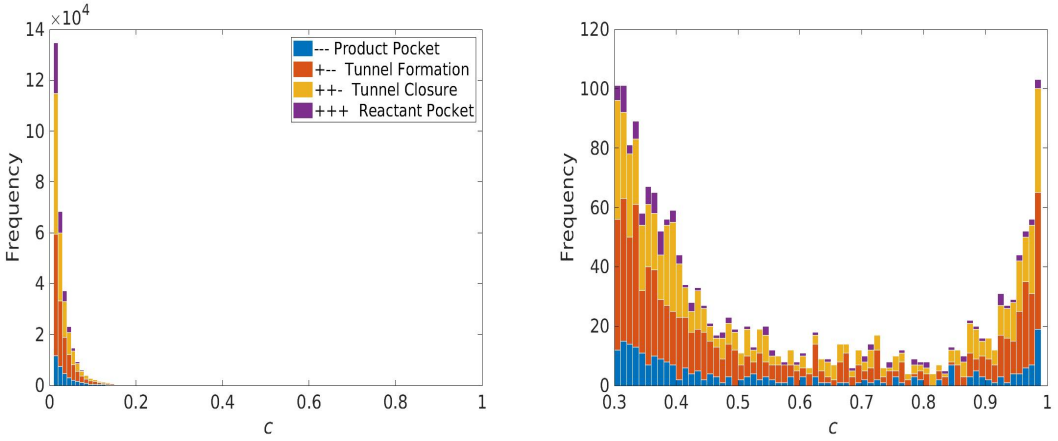

(c) $u'/s_L = 40$

Fig. 4.5 Histograms for the frequency of occurrence of critical points and their corresponding topologies represented by different colours. The left column shows the results for $0.01 < c < 0.99$ whereas the right column shows the results for $0.3 < c < 0.99$.

From Figure 4.5, it is clear that there is a significant increase in the frequency of occurrence of isosurface interactions as u' increases. The number of isosurface interactions increases from roughly 15,000 for the $u' = 10s_L$ case to 60,000 for $u' = 20s_L$ case and then to 300,000 for the $u' = 40s_L$ case. The rise in isosurface interactions can be observed throughout the entire range of c with the increase in u'.

The above histograms for the hydrocarbon flames can now be analysed against those for the hydrogen flames which are replotted in Figure 4.6 for convenience. As previously discussed in Chapter 3 (Section 3.1.2), these plots show isosurface interactions per unit flame surface area to provide a fairer comparison between the Da+ and Da- cases. The turbulence intensities and length scales for the hydrogen and hydrocarbon datasets are not identical, and hence, these results should not be treated as a direct comparison. The aim here is to provide an insight into the difference observed in the general shape of the histograms for the hydrocarbon and hydrogen flames.

The pattern of isosurface interactions in hydrogen flames can be described as follows. There is a noticeable number of isosurface interactions at the leading edge, especially for the Da- case, and their frequency drops as the value of c increases. The isosurface interactions reappear for $c > 0.8$ and become very significant in the range $0.8 < c < 0.99$ for both Da+ and Da- cases. This is in contrast with the hydrocarbon flame results in which the isosurface interactions are mostly found at the leading edge of the flame. However, in the hydrogen flames very few interactions occur in the middle, i.e. $0.2 < c < 0.8$, which is similar to the hydrocarbon flame results.

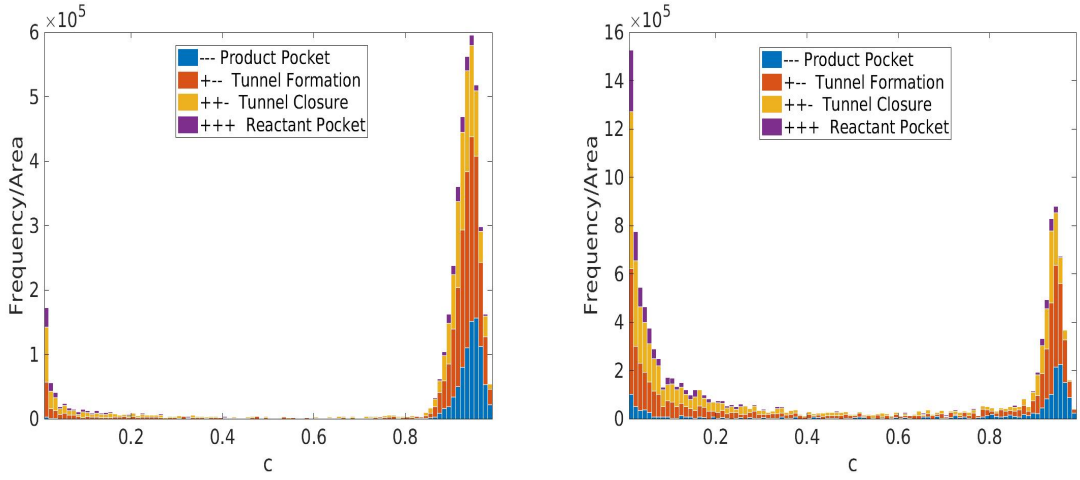

Fig. 4.6 Histograms showing the number of isosurface interactions for Da+ (left) and Da- (right) cases. These figures are replotted from Chapter 3 (Section 3.1.2) for convenience.

The isosurface interaction pattern of the hydrocarbon flames is discussed first. The decrease in the number of interactions with increasing values of c can be can be attributed to the dissipation behaviour of turbulence within the flame. The temperature rises across the flame as c increases and hence, the viscosity increases and results in an increase in the viscous dissipation of turbulence. In the absence of a source of turbulence within the flame, the turbulence monotonically decays within the flame and as a result, the number of isosurface interactions decreases with increasing c values.

Figure 4.7a shows this behaviour qualitatively for the $u' = 20s_L$ case. In this figure, the blue surface is the isosurface at $c = 0.1$ representing the leading edge of the flame and the red surface an isosurface at $c = 0.9$ representing the trailing edge of the flame. It can be observed from this figure that the blue surface exhibits numerous high curvature cusps. On the other hand, the red surface exhibits fewer, low curvature cusps. To quantify this behaviour, it is helpful to examine the flame curvature.
Recall that the mean curvature of a flame surface can be evaluated locally as (Eqn 2.25),

$$\kappa = \frac{1}{2}\frac{\partial n_i}{\partial x_i}$$

where n_i is the local flame normal vector. The curvature is considered positive when the flame surface is curved towards the reactants and vice-versa. For a statistically planar flame, the mean curvature of the flame surface is almost equally likely to be positive or negative, and is therefore close to zero when averaged over a flame surface [51]. The absolute value of mean curvature $|\kappa|$, however, gives a measure of the curvature of the surface regardless of its direction. This quantity averaged over isosurfaces of c, i.e. $\overline{|\kappa|}$ is plotted against c in Fig. 4.7b, normalised by the unstrained laminar flame thickness δ_L. This figure represents the extent of wrinkling at different isosurfaces across the flame. The blue, red and yellow curves in the figure show values of $\overline{|\kappa|}$ for the $u' = 10s_L$, $20s_L$ and $40s_L$ cases respectively. It is clear in Fig. 4.7b that $\overline{|\kappa|}$ is highest for the lowest value of c. The isosurface is therefore more wrinkled at lower values of c and hence results in a high number of isosurface interactions. As c increases, the turbulence decays within the flame and the value of $\overline{|\kappa|}$ decreases monotonically. Consequently, the number of isosurface interactions also decrease as c increases.

The surface averaged value of mean curvature $\overline{|\kappa|}$ is not the only marker for the occurrence of isosurface interactions. On close inspection of Figure 4.7b, it can be observed that the value of $\overline{|\kappa|}$ at $c = 0.3$ for $u' = 40s_L$ is similar to that at $c = 0.1$ for $u' = 20s_L$. However, the number of isosurface interactions corresponding to these values are 100 and 600 respectively. Likewise, the value of $\overline{|\kappa|}$ at $c = 0.3$ for $u' = 20s_L$ is identical to $\overline{|\kappa|}$ at $c = 0.10$ for $u' = 10s_L$,

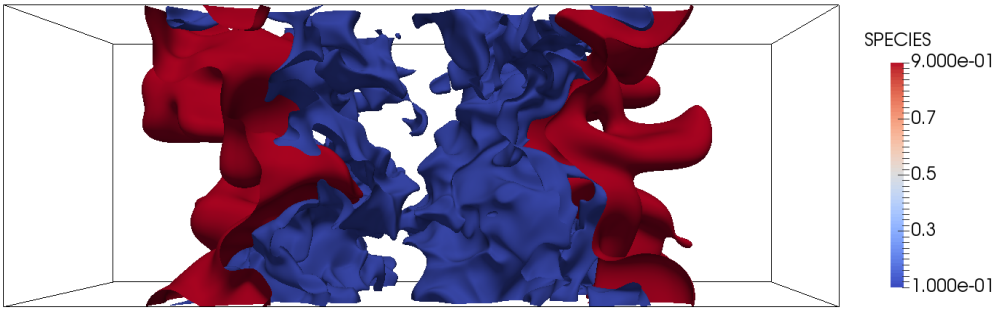

(a)

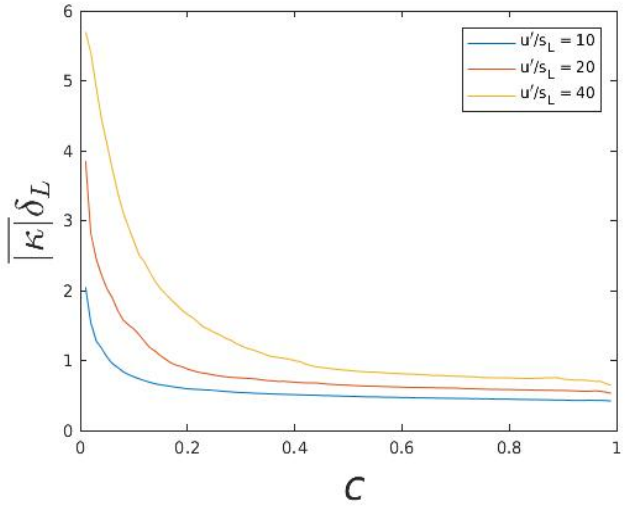

(b)

Fig. 4.7 a) Contours of progress variable at $c = 0.1$ representing the leading edge (blue) and at $c = 0.9$ representing the trailing edge (red) of the flame; b) absolute value of the mean curvature surface averaged over the isosurfaces of progress variable c, normalised by the unstrained laminar flame thickness δ_L, plotted against c for the hydrocarbon flame cases.

but the number of interactions at these values are 25 and 200 respectively. This indicates that the location of the flame at which the isosurface interactions are evaluated also has an important effect on their statistics. The explanation for this behaviour is provided below.

The reaction rate profile for a one-dimensional unstrained laminar flame simulated with single-step chemistry is plotted against the progress variable in Fig. 4.8. All parameters for this 1-D flame are exactly the same as the initial laminar flame profile used in the twin flame dataset. The reaction rate is plotted after the 1-D flame reaches a steady state. The resulting reaction rate profile for this flame should be the same as for all the cases of turbulent flames in the twin flame dataset since no broken reaction zones were observed. Figure 4.8

shows that the reaction rate (blue line) becomes non-zero at $c \simeq 0.3$ and with a peak value at around $c = 0.8$. The shaded background in this figure represents the general shape of the histogram for the $u' = 20s_L$ case. Note that the isosurface interactions disappear in the region $0.3 < c < 0.9$ where the reaction rate starts increasing.

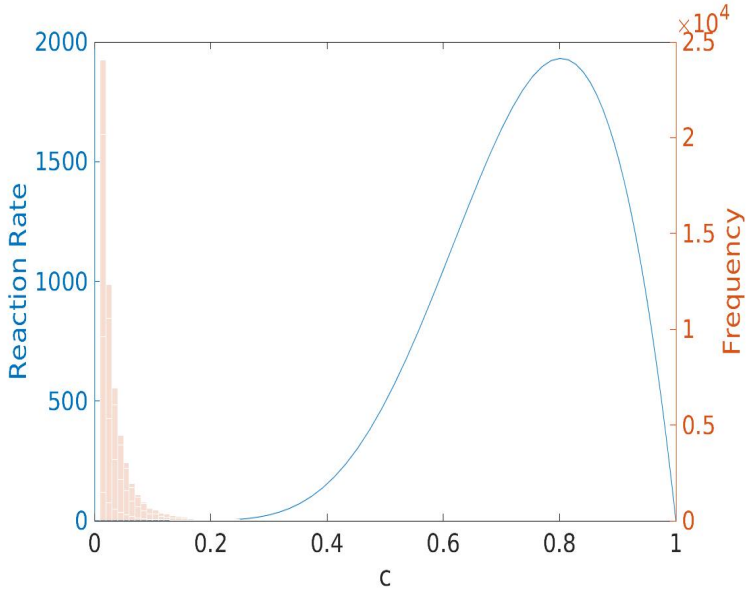

Fig. 4.8 Reaction rate for a 1-D laminar hydrocarbon flame plotted against progress variable c showing the rise in reaction rates and the subsequent drop in the number of interactions represented by the shaded background

The rise in the rate of reaction causes enhanced gradients of both the temperature and progress variable. In physical space, this manifests itself by causing the isosurfaces of the progress variable to come very close to each other. This can be observed in Fig. 4.9 in which a slice of a subsection of the $u' = 20s_L$ case is shown. For simplicity, a subsection is carefully chosen such that it contains only one flame and shows the self-interactions within this flame. Blue colour represents $c = 0$ and red colour represents $c = 1$. The white lines in each subfigure represent a pair of iso-contours of c. In Fig. 4.9a, the iso-contours are at $c = 0.05$ and 0.07, Fig. 4.9b shows iso-contours at ($c = 0.20$ and 0.22), Fig. 4.9c shows iso-contours at $c = 0.50$ and 0.52 and Fig. 4.9d shows iso-contours at $c = 0.90$ and 0.92. Therefore, each pair is $c = 0.02$ apart and represents the leading edge, the approximate point at which reactions begin, middle and the trailing edge of the flame respectively. The distance between the pair of iso-contours at the leading edge (Fig. 4.9a) is large but it decreases as the reactions begin (Fig. 4.9b). In the middle of the flame, the iso-contours become nearly inseparable (Fig. 4.9c).

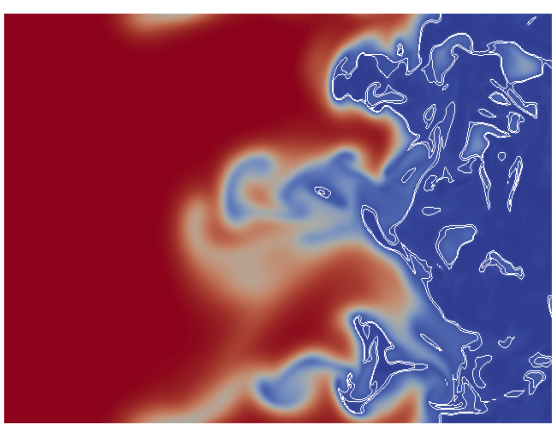

(a) Iso-contours at $c = 0.05$ and 0.07

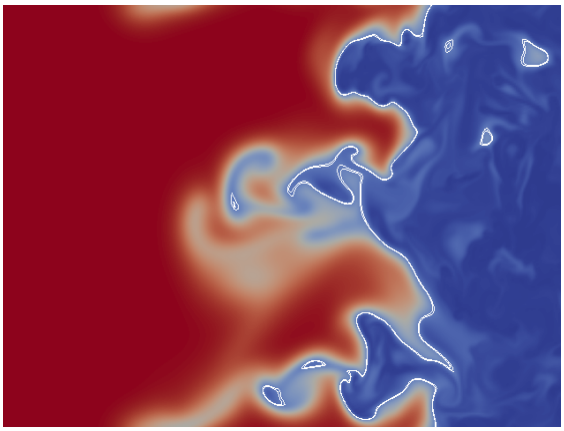

(b) Iso-contours at $c = 0.20$ and 0.22

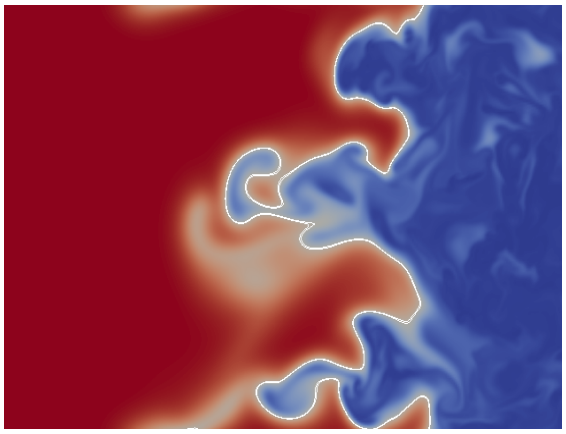

(c) Iso-contours at $c = 0.50$ and 0.52

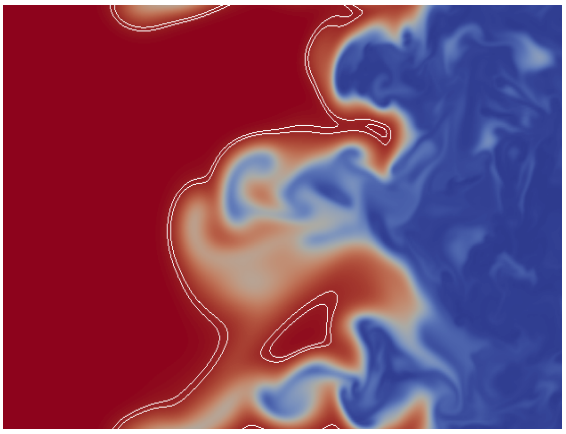

(d) Iso-contours at $c = 0.90$ and 0.92

Fig. 4.9 Slices of the mass fraction profile showing a pair of isosurfaces separated by $c = 0.02$ at four different locations in the flame for the $u' = 20s_L$ case. Blue colour represents $c = 0$ (fresh reactants) and red colour represents $c = 1$ (burnt products).

This has an important effect on the isosurface interaction statistics. Recall that for flames in thin reaction zones regime, i.e. all the flames analysed in this work, the isosurfaces of progress variable are not always parallel to each other. They can bend individually and cause self interactions. The relatively large separation between iso-contours in Fig. 4.9a allows them to curve and self-interact, whereas the small separation between the iso-contours in the middle does not offer enough room for such self interactions. This, combined with the drop in the absolute mean curvature of the flame, explains why the isosurface interactions are less frequent in the middle of the flame.

At the trailing edge of the flame, the separation between the iso-contours is larger compared to that in the middle of the flame (Fig. 4.9d). This provides more room for the self-interactions despite the fact that the surface averaged absolute value of mean curvature

$\overline{|\kappa|}$ is the lowest at the trailing edge of the flame (see Fig. 4.7b). Therefore, the number of isosurface interactions show a slight increase at the trailing edge of the flame as seen in the right hand side subfigures in Fig. 4.6.

The graph between $\overline{|\kappa|}$ and progress variable c for hydrogen flames, normalised by its unstrained laminar flame thickness δ_L, is presented in Figure 4.10. The blue line shows $\overline{|\kappa|}$ for the Da+ case and the red line shows $\overline{|\kappa|}$ for the Da- case. The value of $\overline{|\kappa|}$ is higher for the Da- case (which is at a higher u') resulting in more isosurface interactions than the Da+ case (see Fig. 4.6). The general pattern of this graph at the leading edge remains similar to that of the hydrocarbon flames in that as c increases, the value of $\overline{|\kappa|}$, and consequently the number of isosurface interactions, decreases for both the Da+ and Da- cases.

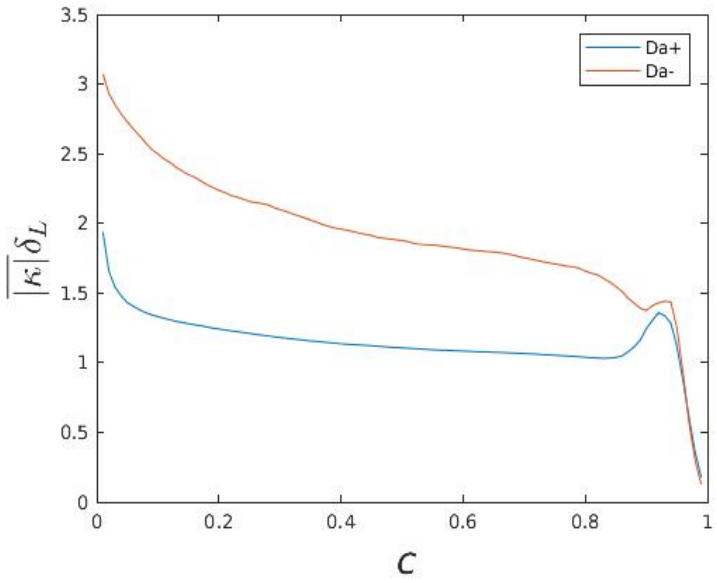

Fig. 4.10 Surface averaged absolute value of the mean curvature $\overline{|\kappa|}$ normalised by the unstrained laminar flame thickness δ_L, plotted against the progress variable c. In this figure, the blue line represents $\overline{|\kappa|}$ for the Da+ case and the red line represents $\overline{|\kappa|}$ for the Da- case

Near the trailing edge of the hydrogen-air flames, there is a peak in the graph of $\overline{|\kappa|}$ for both cases. Although the peak is more pronounced for the Da+ than the Da- case, the peak value of $\overline{|\kappa|}$ is roughly the same for both cases and it occurs at around $c \sim 0.9$. This increase in $\overline{|\kappa|}$ near the trailing edge drives the increase in the frequency of isosurface interactions as observed in Fig. 4.6. As previously discussed, this behaviour is unique to the hydrogen flames and is not seen in the hydrocarbon flames. There are two main reasons for it.

First, the turbulence generated in the hydrogen-air flame dataset of Hawkes et al. [35] is due to mean shear in the flow which may provide a continuous source of turbulence through the flame. Chaudhuri et al. [74] analysed the relative contribution of mean shear on total

strain rate for the Hawkes et al. dataset [35] by plotting the quantity F, which is the ratio of strain rate caused by mean velocity gradients on the surface to the total tangential strain rate due to turbulence. This is shown in Figure 4.11. They found that the mean shear amounts to about 3-20% of the total strain rate, with highest contribution at the trailing edge of the flame. The value of F was found to be higher for the Da+ case than for the Da- case throughout the flame. The direct effect of mean shear on the isosurface interactions statistics is unknown. Given that the value of F remains relatively small, i.e. the contribution of mean shear is small relative to the tangential strain rate, mean shear is not likely to be the primary cause of the increase in the isosurface interactions at the trailing edge of the flame.

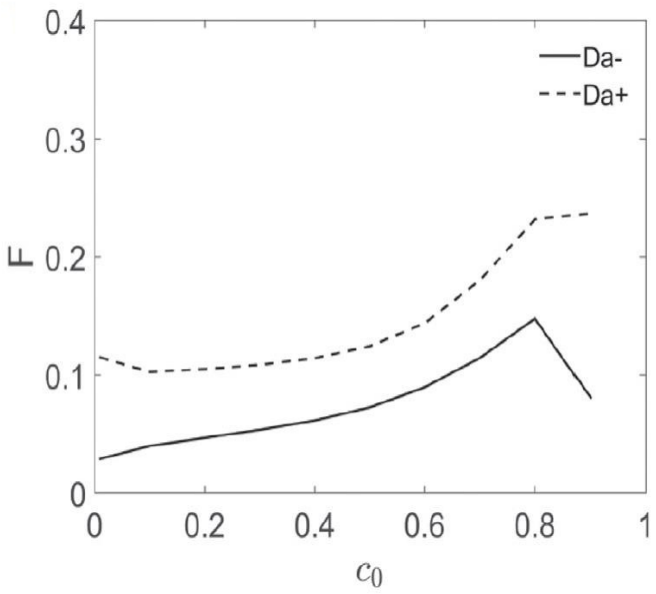

Fig. 4.11 Figure from [74] showing the ratio F of strain caused by the mean velocity gradients, i.e. contribution of mean shear to the total tangential strain rate plotted against the progress variable c_0 defined using temperature by Chaudhuri et al. [74]. The dotted line is for the Da+ case and the solid line is for the Da- case. The net contribution of mean shear can be seen to be higher at the trailing edge of the flames.

The second and very important reason for the increased number of isosurface interactions is the effect of thermo-diffusive instabilities caused by Le < 1. The mechanism for such instabilities has been discussed earlier. These instabilities are enhanced towards the trailing edge of the flame where the Lewis number takes its lowest value. This can be shown by analysing Le in a one-dimensional hydrogen-air laminar flame simulated using the code `Senga2` [68]. This flame was simulated in a 1-D domain of length 1.5cm in the x-direction, which corresponds to $30\delta_L$. A 9-species, 21-step mechanism [62] was used with the equivalence ratio of the mixture set to $\phi = 0.7$ and the reactants preheated to 700K. This

made the initial mixture the same as that used in Hawkes et al. dataset [35]. The unstrained laminar flame speed and thickness for this mixture are 7.9m/s and 0.5mm respectively (see Section 3.1.1, Chapter 3). The boundaries of the domain were set as inflow-outflow. The reactants enter the domain with an inflow velocity of 7.9m/s to match the flame speed of the mixture and keep the flame stationary in space.

The thermal conductivity λ for the mixture and mass diffusivity D of H_2 are calculated using the mixture averaged transport approach. Using these values, the Lewis number (Eqn. 2.15) is evaluated and plotted against the progress variable c. The result obtained for this flame is shown in Fig. 4.12 which clearly shows that the Lewis number decreases across the flame as the c increases and is lowest at the trailing edge of the flame. This indicates that the thermo-diffusive instabilities are further exaggerated towards the trailing edge of the flame resulting in increased isosurface curvature and more frequent isosurface interactions.

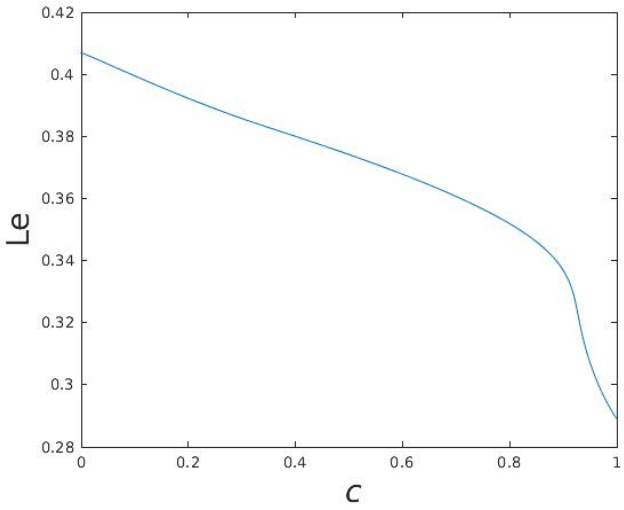

Fig. 4.12 Variation of Lewis number with c in a 1-D laminar hydrogen flame.

The importance of Le < 1 for flame wrinkling at the trailing edge of the flame is demonstrated further through a simulation of a lean hydrogen-air flame evolving in three-dimensional low intensity turbulence. For this simulation, a single 1-D laminar H_2-air flame profile computed as described above was mapped on a 3-D domain along with a pre-computed field of homogeneous and isotropic turbulence. The intensity of turbulence was kept low so as not to directly cause isosurface interactions but sufficient to trigger the thermo-diffusive instabilities. Inflow-outflow boundary conditions were employed with reactants incoming at the laminar flame speed (=7.9m/s). The flame was allowed to interact with the turbulence for $t = 2.5\tau$ and the statistics of isosurface interactions were recorded [21]. The results for this flame are shown in Fig. 4.13.

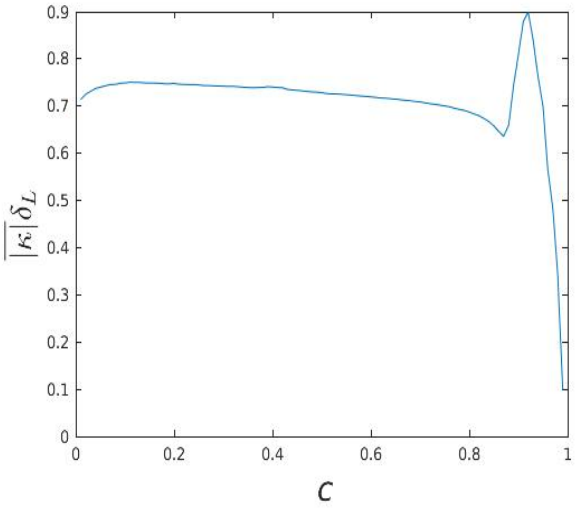

(a) Surface averaged absolute mean curvature $\overline{|\kappa|}$ normalised by the unstrained laminar flame thickness δ_L vs c for hydrogen flame in the box in low intensity turbulence

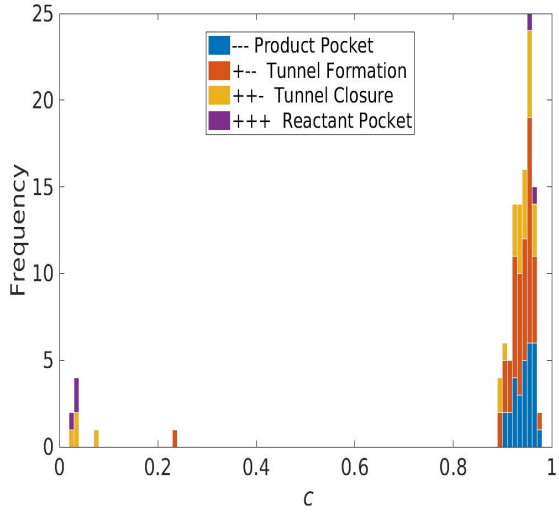

(b) Histogram showing frequency of occurrence of isosurface interactions for hydrogen flame in the box

Fig. 4.13 Results of hydrogen flame in the box especially simulated to show the effects of thermo-diffusive instabilities caused by Le < 1 on the statistics of isosurface interactions

It can be seen in Fig. 4.13a that there is a significant rise in $\overline{|\kappa|}$ at the trailing edge of the flame consistent with the results for the Da+ and Da- cases. Keeping in mind that there is no turbulence generation in this case and that the homogeneous isotropic turbulence decays over time, the increase in $\overline{|\kappa|}$ observed at the trailing edge of the flame arises only from the action of the thermo-diffusive instabilities due to Le < 1. The resulting histogram of the frequency of isosurface interactions is shown in Fig. 4.13b. Very few interactions are observed at the

leading edge because of the low intensity of turbulence. However, a significant number of interactions occurs at the trailing edge. It is therefore clear that a significant fraction of the trailing edge isosurface interactions observed for the hydrogen-air flames results from the non-unity Lewis number effects on the thermo-diffusive balance of the flame.

The combined effect of mean shear in the hydrogen flame dataset and the thermo-diffusive instabilities explain the peak in $\overline{|\kappa|}$ and the corresponding increase in the isosurface interactions at the trailing edge of the flame. In the middle of the hydrogen air flames ($0.2 < c < 0.9$), the frequency of interactions decreases considerably, similar to what was observed for the hydrocarbon flames. This is attributed to the high gradients of temperature and species mass fraction caused by the increase in reaction rate. The isosurfaces of c come very close together and suppress the isosurface interactions. Figure 4.14 shows the reaction rate (blue line) plotted against c for a 1-D unstrained laminar hydrogen-air flame with the same chemistry and initial parameters as in the Hawkes et al. [35] dataset. The shaded background shows the shape of the histograms of the number of isosurface interactions for the Da+ case. The number of isosurface interactions can be seen to disappear as the reaction rate becomes significant. Also note that the isosurface interactions towards the trailing edge become significant as the reaction rate decreases.

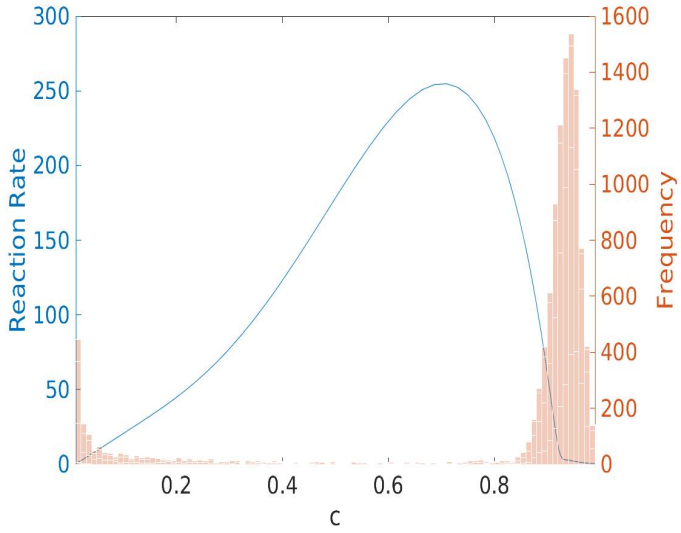

Fig. 4.14 Reaction rate profile for a 1-D laminar hydrogen flame (blue line) plotted against c. The shaded red background represents the general shape of the histograms of frequency of isosurface interactions for the Da+ case.

4.2 Self-Interactions in Hydrocarbon Premixed Flames

The comparisons between the hydrocarbon and hydrogen flames highlight the important factors that result in isosurface interactions. The results so far only focus on the twin flame configuration that ensures the occurrence of isosurface interactions due to the two flame surfaces colliding, but there can also be a significant number of interactions within each of these flames individually. The flame-flame interaction events such as flame pinch-off that lead to changes in flame surface area occur within single flames and the altered flame surface continues to propagate. In twin flames, these events can get suppressed as the flame surfaces collide and get completely annihilated. Therefore, the effect of flame-flame interactions on overall flame propagation properties is better represented through self-interactions in single flames.

The first question is whether there is a sufficient number of self-interactions in a single flame to obtain statistically converged results. The statistics of isosurface interactions of the $u' = 20s_L$ case in a twin flame configuration are compared with a single flame simulated with exactly the same physical and thermo-chemical parameters but in an inflow-outflow configuration. The statistics are recorded for $t = 10\tau$ during which a significant amount of collision has occurred in the twin flames whereas only self-interactions have occurred in a single flame. The combined histogram of multiple snapshots taken every $t = 0.25\tau$ apart during the simulation is analysed for each case. The resulting histograms are shown in Figure 4.15. The histogram on the left is for the twin flame configuration whereas that on the right is for a single flame. The colours in the figure represent the topology of the interacting flame surfaces near the isosurface interaction events.

It is observed that the shape of the histogram is qualitatively similar in both cases. Furthermore, the number of interactions for a single flame is roughly half that for the twin flames indicating that the number of interactions per flame is nearly equal for both cases. Hence, it follows that the isosurface interactions resulting from the direct collision of two flames in a twin flame setup are simply replaced by self-interactions in a single flame and the overall isosurface interaction statistics are not significantly altered. This makes it possible to perform a standalone statistical analysis of isosurface interactions in single flames [22].

4.2.1 Dataset

The DNS data analysed here are part of a published dataset [75] generated using the `Senga2` solver [68]. This dataset consists of five separate simulations conducted by solving the Navier-Stokes equations in 3D compressible form along with a transport equation for the

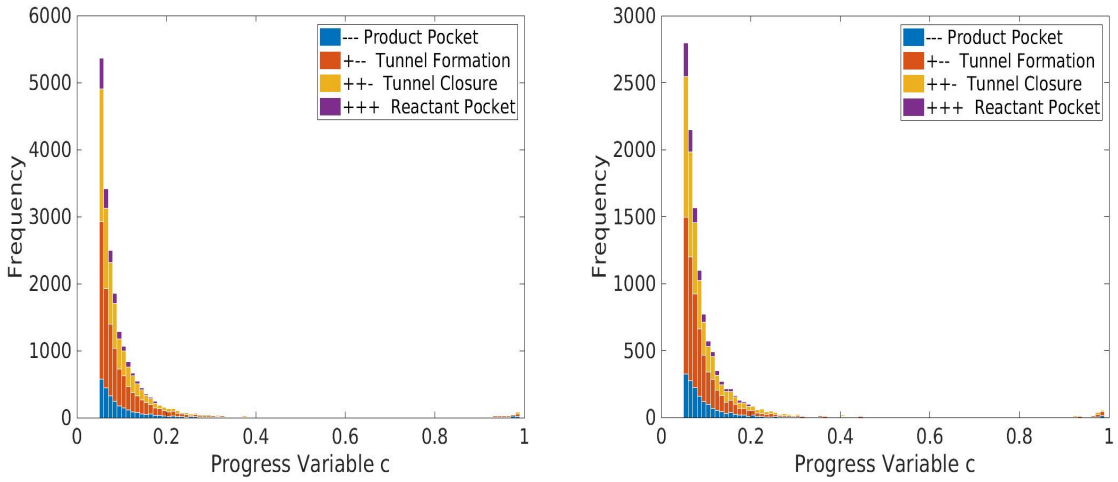

Fig. 4.15 Histograms of the number of interactions in a single flame (left) vs counter flowing flames (right). The number of interactions for counter flowing flames is roughly twice as much as the single flame

progress variable. Each case simulates a statistically-planar flame brush propagating freely towards the inlet in an inflow-outflow configuration.

The domain is initialised with a planar laminar flame surrounded by a field of homogeneous isotropic turbulence of desired intensity computed *a priori*. A copy of the initial turbulent flow field is also convected through the inlet so as to maintain the turbulence ahead of the flame. The intensity of the turbulent flow field is increased successively across the simulation dataset. Flame chemistry is represented using a single-step Arrhenius reaction mechanism with the Lewis number of the reacting species set to unity.

The reaction mechanism is tuned to replicate the flame propagation speed of stoichiometric methane-air flame, i.e 39 cm/s, and also to capture the corresponding thickness of the reaction zone. Furthermore, Nivarti et al. [75] validated the results obtained for a high-intensity case in this dataset using a detailed 25-step reaction mechanism for methane-air combustion [69]. Hence the DNS dataset can be taken as representative of hydrocarbon-air combustion.

Similar to the twin flame setup, all thermo-chemical and physical parameters are maintained constant except the turbulence intensity u'. The integral length scale ℓ_0 was initialised at $\ell_0 = 2.5\delta_L$. The values of u' in this dataset are $1.5s_L$, $5s_L$, $10s_L$ and $20s_L$ and $30s_L$. Only the latter three cases are analysed. The domain for all cases was discretised using a uniform mesh of cubical cells with spacing $\Delta x = 52\mu$m. Table 4.2 summarises the important parameters for this dataset.

u'/s_L	ℓ_0/δ_L	η_K	Da	Re	Ka	Δx	$x-length$
10	2.5	29μm	0.27	20	19.08	52μm	15mm
20	2.5	20μm	0.13	40	53.96	52μm	15mm
30	2.5	17μm	0.09	80	99.82	52μm	15mm

Table 4.2 Key parameters for the hydrocarbon dataset. The values of Ka increases and Da decreases as u' increases.

The Karlovitz number

$$\mathrm{Ka} = \frac{u'}{\lambda_T}\frac{\delta_L}{s_L} \sim \left(\frac{u'}{s_L}\right)^{\frac{3}{2}}\left(\frac{\delta_L}{\ell_0}\right)^{\frac{1}{2}},$$

based on the Taylor length scale λ_T, and the Damköhler number

$$\mathrm{Da} = \frac{s_L \ell_0}{u'\delta_L}$$

varies across the dataset in that Ka increases and Da decreases as u' increases (see Table 4.2). This is shown in the Borghi diagram in Figure 4.16. The red squares represent the cases with $u' = 10s_L, 20s_L$ and $30s_L$ that are analysed in this section. More details on the dataset can be found in the reference [75].

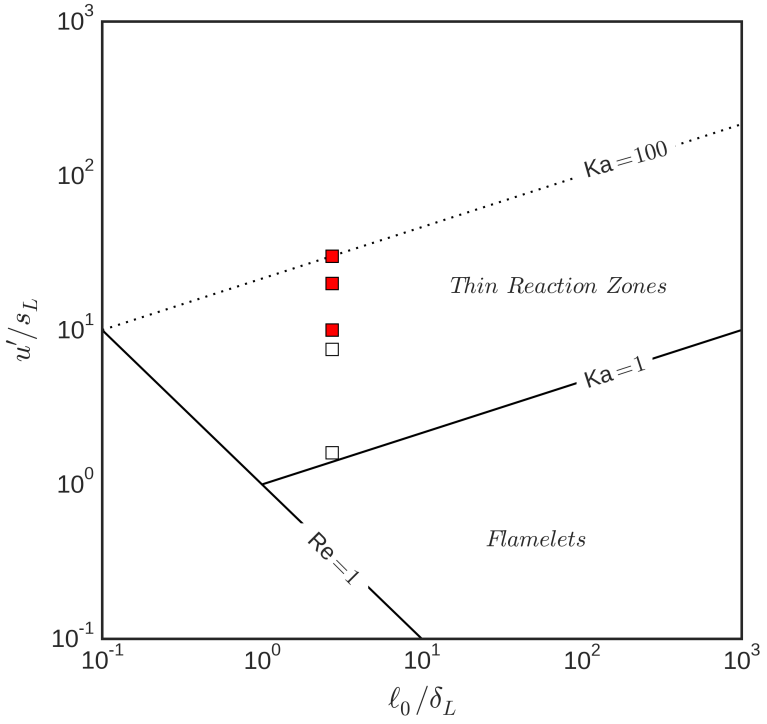

Fig. 4.16 Regimes of combustion indicating the cases investigated here (red squares).

Two dimensional slices of the product mass fraction in the three-dimensional simulation domain for each case are shown in Figure 4.17. Each slice is taken at the end of the simulation, i.e. at $t = 4.8\tau$. The top row in Fig. 4.17a is the product mass fraction for the $u' = 10s_L$ case, the middle row (Fig. 4.17b) is for the $u' = 20s_L$ case and the bottom row (Fig. 4.17c) is for the $u' = 30s_L$ case. Blue colour represents fresh reactants whereas red colour represents burnt products. The reaction zone in each case remained as an intact continuous surface indicating that the flamelet assumption is valid for these cases.

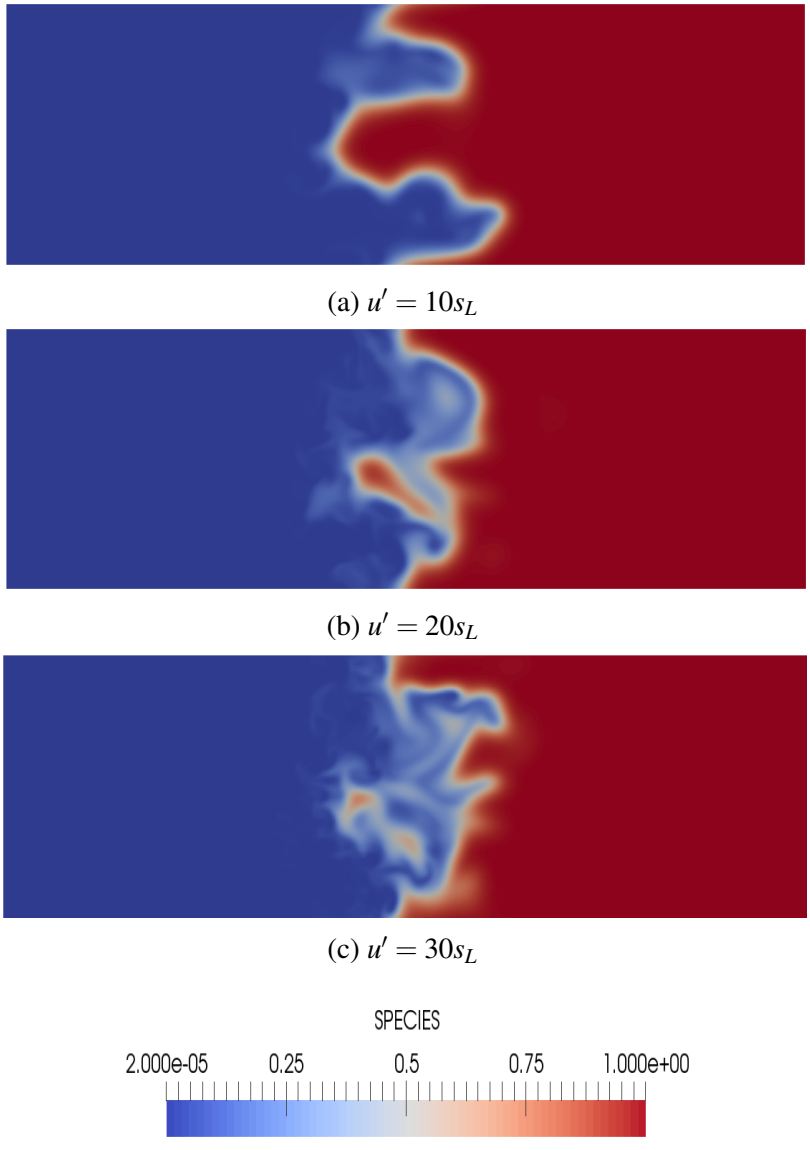

(a) $u' = 10s_L$

(b) $u' = 20s_L$

(c) $u' = 30s_L$

Fig. 4.17 Two dimensional slices of the 3-D snapshots at increasing u' (top to bottom) after $t = 4.8\tau$. Colour scheme represents product mass fraction

4.2.2 Flame Self Interaction Statistics

The method of evaluating isosurface interactions using the Morse theory of critical points [34] is now applied to the Nivarti and Cant dataset [75]. The frequency of occurrence of critical points is recorded in the form of histograms plotted against the progress variable c in exactly the same way as for the twin flame setup. The results for the single flames are presented in Figure 4.18. The left column of the figure shows the total number of critical points, and hence the isosurface interactions across the whole range of the flame, i.e. $0.01 < c < 0.99$, whereas the right column focusses only on the $0.3 < c < 0.99$ range where the isosurface interactions are relatively fewer. The statistics are recorded for multiple snapshots to get sufficient interactions for good statistical results. These snapshots are taken $t = 50\mu$s apart during the total runtime of $t = 4.8\tau$ for each simulation.

The colours in the histograms represent the different general topologies at the critical points namely reactant pockets (RP). tunnel closure (TC), tunnel formation (TF) and product pockets (PP). The general shape of the histogram in all cases is similar to those previously observed for the twin flame cases. The peak number of interactions occurs at the leading edge of the flame ($0.01 < c < 0.2$) and drops monotonically as the value of c increases. Very few interactions are observed between $0.2 < c < 0.9$. At the trailing edge ($c > 0.9$), a marginal increase in isosurface interactions is observed, although the number is still small compared to the leading edge interactions.

All the interactions observed in Fig. 4.18 are self interactions within single flames. These histograms show that numerous isosurface interactions take place even within a single flame, and their frequency increases significantly as the turbulence intensity increases. This is consistent with the results obtained for the twin flame configuration previously. Going from $u'/s_L = 10$ at the top row to $u'/s_L = 30$ at the bottom, the number of isosurface interactions increases by more than an order of magnitude.

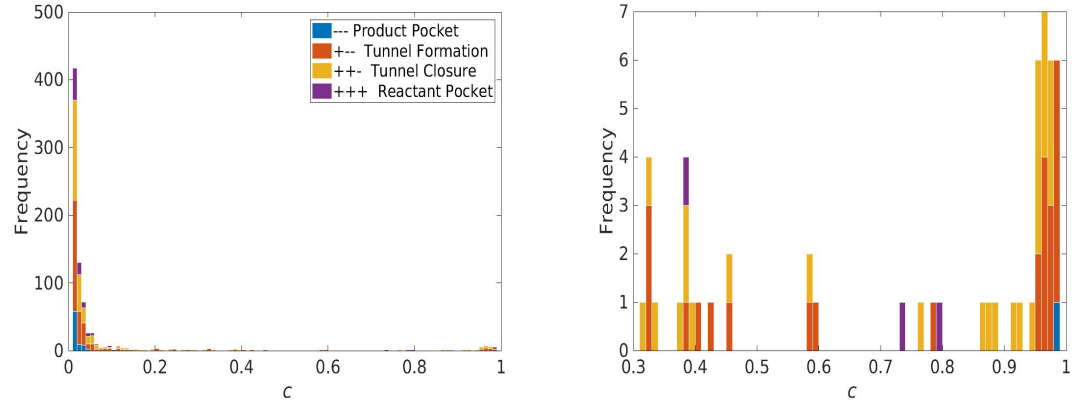

(a) $u'/s_L = 10$

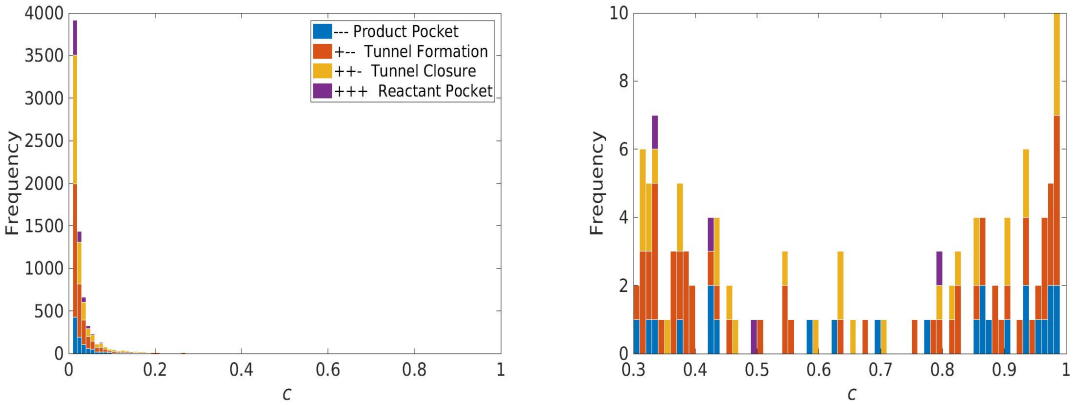

(b) $u'/s_L = 20$

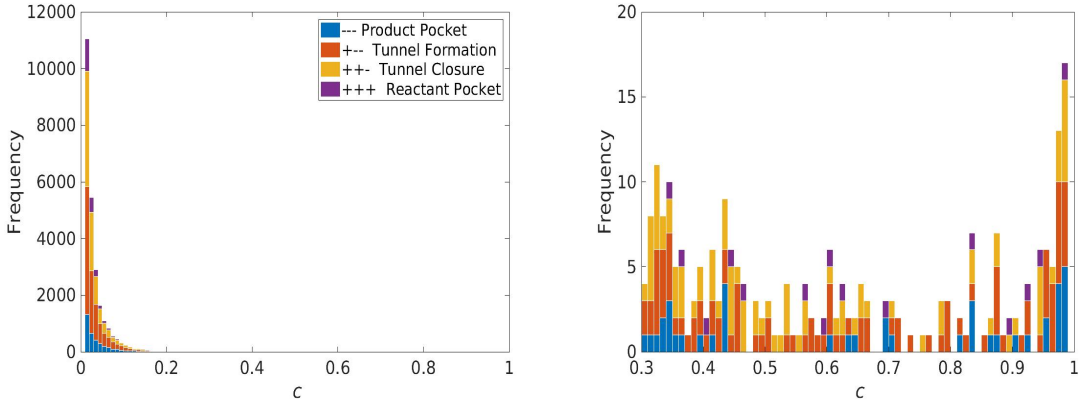

(c) $u'/s_L = 40$

Fig. 4.18 Histograms for the single flame dataset with increasing turbulence intensity. Histograms on the left represent the result for the leading edge $(0.01 < c < 0.99)$ and those on the right focus on $(0.3 < c < 0.99)$ since the critical points in this region are fewer and not clearly visible in the figures on the left.

The reasoning for the observed pattern also remains the same as that for the twin flame setup. The dominance of isosurface interactions at the leading edge of the flame is due to greater wrinkling at low values of c. The isosurfaces of the progress variable representing the leading edge and trailing edge of the flame are shown in Figure 4.19a. It can be observed that the leading edge of the flame represented by the blue surface is more wrinkled than the trailing edge represented by the red surface. The surface averaged absolute value of mean curvature $\overline{|\kappa|}$ normalised by the unstrained laminar flame thickness δ_L, plotted against c is presented in Figure 4.19b for the $u'/s_L = 30$ case. It is apparent that the flame indeed has higher curvature at the leading edge and that the curvature keeps decreasing as c increases.

It is also interesting to look at the relative occurrence of individual topological events at the point where the flame surfaces interact. This is important for understanding the effect of isosurface interactions on overall propagation since each individual topology has different propagation characteristics as discussed in Chapter 3. For example, reactant pockets are formed following the tunnel closure of a narrow channel in a high curvature cusp. The tunnel closure event in this case leads to a reduction in overall flame surface area as the pocket pinches off. At the same time, the pocket burns out rapidly, thus causing enhanced consumption rate.

Table 4.3 shows the fraction of each type of topology for increasing turbulent intensities. The fractions are calculated by dividing the frequency of occurrence of individual topological events by the total number of interactions for an entire range of c. It should be noted that tunnel formation TF and tunnel closure TC are cylindrical topologies whereas product pockets PP and reactant pockets RP are spherical topologies. It can be seen in Table 4.3 that cylindrical topologies TF and TC account for about 80% of the total number of observed interactions while spherical topologies PP and RP account for about 20% of the total interactions. This is consistent with the findings of Pope et al. [54] and Cant et al. [50]. This also suggests that the overall effects related to cylindrical topologies, for example the reduction in flame surface area following a tunnel closure event, will be dominant over the effects related to spherical topologies, such as enhanced consumption rate due to pocket burnout.

An interesting picture emerges when plotting the fraction of topologies with increasing turbulence intensity (Fig. 4.20 top). When the turbulence intensity increases from $u' = 10s_L$ to $u' = 30s_L$, it is observed that a larger fraction of product pockets are formed within the domain. At the same time, the fraction of reactant pockets decreases as u' increases. Furthermore, the rise in the proportion of product pockets is almost mirrored by the drop in the proportion of reactant pockets. A similar observation is made for tunnel formation and tunnel closure (Fig. 4.20 bottom), in that there is a steady rise in the proportion of tunnel formation and an almost identical drop in the proportion of tunnel closure events.

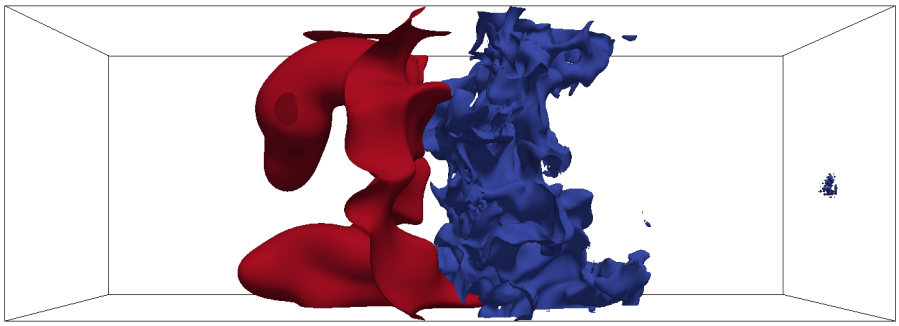

(a) Two different isosurfaces of the progress variable at $u'/s_L = 30$. Blue surface represents c=0.02 and red surface represents c=0.99. The difference in wrinkling is apparent

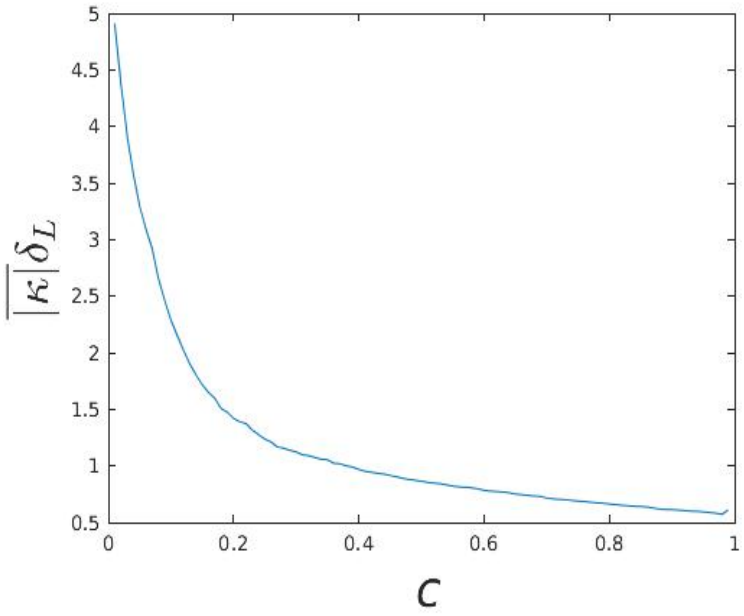

(b) Variation of $\overline{|\kappa|}$ with c, normalised by the unstrained laminar flame thickness δ_L.

Fig. 4.19 (a) Isosurfaces of c representing the leading (blue surface) and trailing (red surface) edges of the flame, and (b) surface averaged absolute mean curvature $\overline{|\kappa|}$ normalised by the unstrained laminar flame thickness δ_L, plotted against c for the $u'/s_L = 30$ case.

This behaviour can also be observed in the twin flame setup. The plots showing the fraction of the individual topologies are presented in Figure 4.21 with the top figure showing the result for PP and RP events and the bottom figure showing the result for TF and TC events. These results should not be directly compared with those for the single flames since the range of u' is different in each dataset. The highest intensity of turbulence is $40s_L$ for the twin flames dataset whereas it is $30s_L$ for the single flame dataset. The value of ℓ_0 is also different in these datasets, i.e. $\ell_0 = 2\delta_L$ for the twin flame dataset and $\ell_0 = 2.5\delta_L$ for

Topology	u'/s_L		
	10	20	30
PP	0.0983	0.1274	0.1345
TF	0.3909	0.4140	0.4203
TC	0.3922	0.3629	0.3554
RP	0.1185	0.0955	0.0898

Table 4.3 Fraction of topologies for increasing turbulent intensities. The fractions are calculated by dividing the frequency of occurrence of individual topological events by the total number of interactions for an entire range of c.

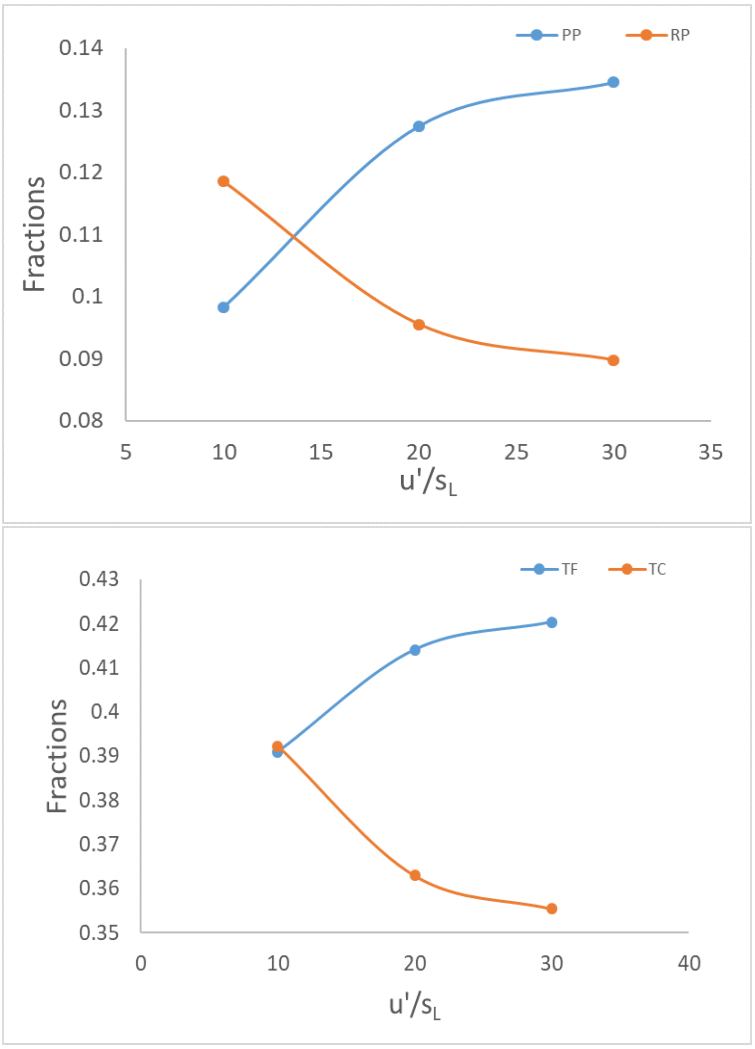

Fig. 4.20 Fractions of Reactant Pockets (RP) and Product Pockets (PP) (top), and fractions of Tunnel Formation (TF) and Tunnel Closure (TC) (bottom) for the single flame dataset

the single flame dataset. However, consistent behaviour can be seen for both datasets in that the fraction of TF and PP increases and that of TC and RP decreases as u' increases. The increase in the fraction of TF and PP does not mirror the drop in TC and RP for the twin flame setup.

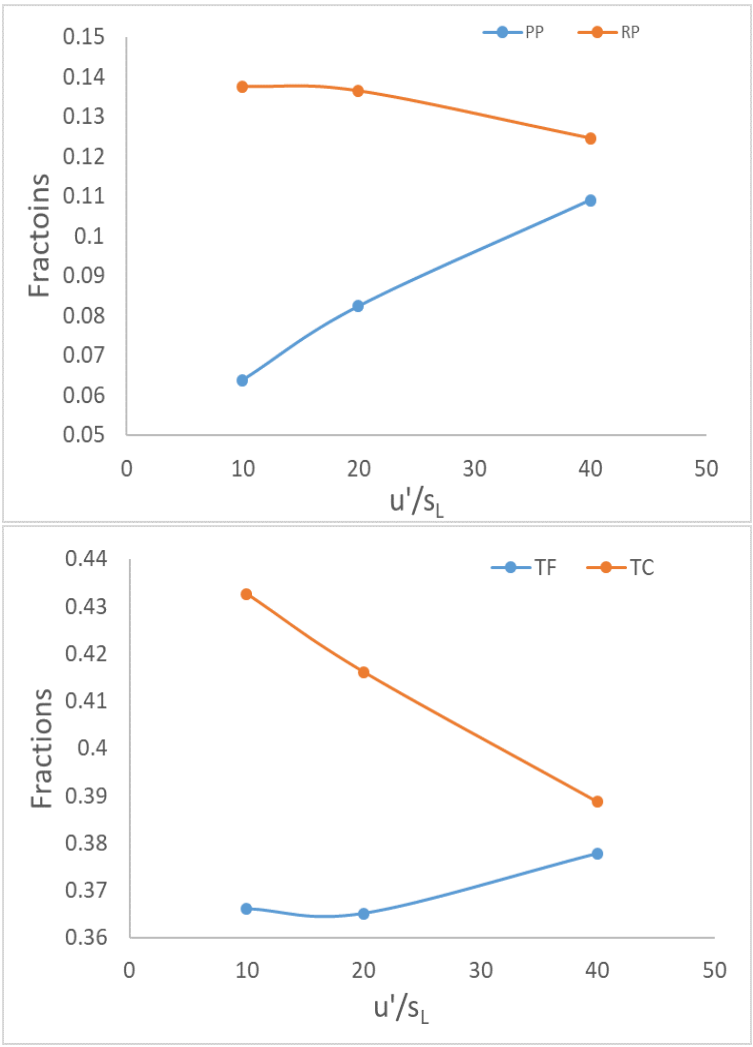

Fig. 4.21 Fractions of Reactant Pockets (RP) and Product Pockets (PP) (top), and fractions of Tunnel Formation (TF) and Tunnel Closure (TC) (bottom) for the twin flame dataset

Note that the fractions of product pockets PP and tunnel formation TF events for the twin flame dataset (Fig. 4.21) are smaller compared to those for the single flame dataset. This is because these events form ahead of the flame in the unburnt reactants. For the twin flame cases, these events occurring for one flame will be annihilated by the other flame, therefore making them less likely to be captured in a frozen snapshot.

The effect of each individual topology on global flame properties is still unknown and yet to be investigated systematically. However, the above result may have implications for flame propagation with increasing turbulence intensity. The reactant pocket and tunnel closure topologies result in a very high displacement speed near burnout [15, 20, 23, 24, 29].

4.2.3 Chapter Conclusions

The histograms showing the frequency of occurrence of critical points, and hence the interactions between the isosurfaces of progress variable c, were analysed for a hydrocarbon twin flame dataset with varying turbulence intensity. These isosurface interactions can be treated as flame-flame interactions for an isosurface of progress variable c that represents the reaction zone. The results from this dataset were compared with those for the hydrogen flame dataset. In hydrocarbon flames the interactions are mostly observed at the leading edge and are not frequent at the trailing edge. The number of isosurface interactions increases for higher turbulence intensities. The reason for this behaviour is attributed to the dissipation of turbulence with increasing temperature within a flame coupled with the lack of thermo-diffusive instabilities caused by non-unity Lewis number effects.

For hydrogen-air flames, a slightly different picture of the isosurface interactions was observed in which a significant number of interactions was found at the trailing edge of the flame. This was because of two reasons: (1) The fraction of mean shear in the total strain was found to increase at the trailing edge of the hydrogen-air flames [74], and (2) the thermo-diffusive instabilities caused by $\mathrm{Le} < 1$ effects are more prominent at the trailing edge of the flame. These effects resulted in a net increase in the absolute mean curvature of the flame at the trailing edge causing numerous isosurface interactions in that region. Very few interactions were found in the middle region for both hydrocarbon and hydrogen flames where chemical reactions occur.

It was also found that the number of interactions in the case of two flames is nearly twice as much as that in a single flame. This indicates that a significant number of interactions occur within each individual flame and the frequency of these self-interactions matches that of the twin flame setup. Furthermore, the histograms for the single flames exhibit the same behaviour as the twin flames, in that the isosurface interactions in a single flame are also mostly found at the leading edge and are not frequent at the trailing edge.

In all the flame cases analysed in this chapter, very few isosurface interactions are recorded in the middle of the flame where the chemical reaction rates are high. The reason for this observation is that because of the increase in reaction rate, high gradients of temperature and species exist, and hence the physical spacing between the isosurfaces of the progress

variable becomes very small. As a result, the individual isosurfaces do not get enough room to curve and interact within the flame.

A significant result for the hydrocarbon flames is that the proportion of different topologies varies with the turbulence intensity. There is an increase in product pockets and tunnel formation events with increasing turbulence intensity, and a corresponding drop in reactant pockets and tunnel closure events for those intensities. This behaviour is observed in both twin flame setup and single flame setup. However, in single flames the drop in the fraction of the reactant pockets mirrors the increase in the fraction of the product pockets. The same is true for the tunnel closure and tunnel formation events. The reactant pocket and tunnel closure topologies result in a very high displacement speed near burnout as discussed in Chapter 3 and references [15, 20, 23, 24, 29].

Chapter 5

Role of Isosurface Interactions in Turbulent Flame Propagation

An effective way of capturing the interactions between the isosurfaces of progress variable with the help of critical points [21] has been applied to both hydrogen and hydrocarbon flames. The results provide an important insight into the location of isosurface interactions within the flame. Several important properties that affect the frequency of interactions have been discussed. By choosing the value of c which best represents the flame, the flame-flame interactions can be analysed using the critical point method. The question still remains, how do the flame-flame interactions affect the overall flame propagation?

Some of the important properties that describe flame behaviour include the flame speed, flame area and flame surface density. The turbulent diffusivity D_T can also become significant in cases when the small length scales of turbulence act to enhance the transport of reactants into the flame. It has already been established that events such as tunnel closure directly affect the flame surface area whereas the reactant pockets burn out rapidly and enhance the overall consumption speed [15, 20, 23, 24]. The analysis in Chapter 3 focussed on the displacement speed and the surface density function near the flame-flame interaction events. This Chapter focusses on the consumption speed s_T and flame surface area A_T and their changes with the frequency of isosurface interactions.

The flame speeds and related properties obtained from a highly resolved DNS dataset are analysed here. The results are recorded for varying integral length scales ℓ_0 as well as the turbulence intensity u'. The next section outlines what changes to expect in the flame propagation properties based on the frequency of isosurface interactions. The subsequent sections describe the dataset used and the corresponding results. The final section summarises the findings of this chapter.

5.1 What To Expect?

The increase in flame surface area A_T by the action of turbulence [8, 9], and the subsequent increase in the consumption speed s_T has been extensively studied both experimentally [14] and computationally [15, 20, 75].

$$\frac{s_T}{s_L} \sim \frac{A_T}{A_L} => \frac{s_T}{s_L} = \frac{A_T}{A_L} I_0$$

where I_0 is called the stretch factor [14, 55]. Note that the above relationships are valid when all turbulence length scales are larger than δ_L. In the above expression, the flame consumption speed can be evaluated using the expression (see Eqn. 2.17)

$$s_T = -\frac{1}{\rho_u Y_{u,F} A_0} \int_V \dot{\omega}_F dV$$

where ρ_u and $Y_{u,F}$ are the unburnt mixture density and fuel mass fraction respectively and A_0 is the cross sectional area of the domain. The relation between flame area and flame surface density at a fixed isosurface $c = c^*$ is restated here as (see Eqn. 2.19)

$$A_T = \int_{-\infty}^{\infty} \Sigma \delta(c - c^*) dV$$

Isosurface interactions can directly affect both s_T and A_T. It can be argued on physical grounds that the head on collision of two flame surfaces leads to mutual annihilation and directly alters the flame surface area [3, 14]. In addition, events such as formation of reactant pockets also cause changes in the flame area. Such a process is illustrated in Figure 5.1 with the help of slices of isosurfaces of c at different instances of time showing formation of a reactant pocket. Figure 5.1a shows an initial isosurface with a relatively large surface area. No flame pockets are present in this figure. As time progresses, two local flame surfaces within the isosurface begin to approach each other as seen in Fig. 5.1b. The subsequent figures show the local surfaces colliding with each other causing the formation of a reactant pocket (Fig. 5.1c). The final slice (Fig. 5.1d) shows an isolated pocket separated out of the isosurface. The pocket burns out rapidly causing a brief and rapid increase in the consumption speed [15, 20, 23, 24]. However, the isosurface left behind now has a relatively smaller flame area. In the figure, letter 'U' represents unburnt reactants and letter 'B' represents burnt products.

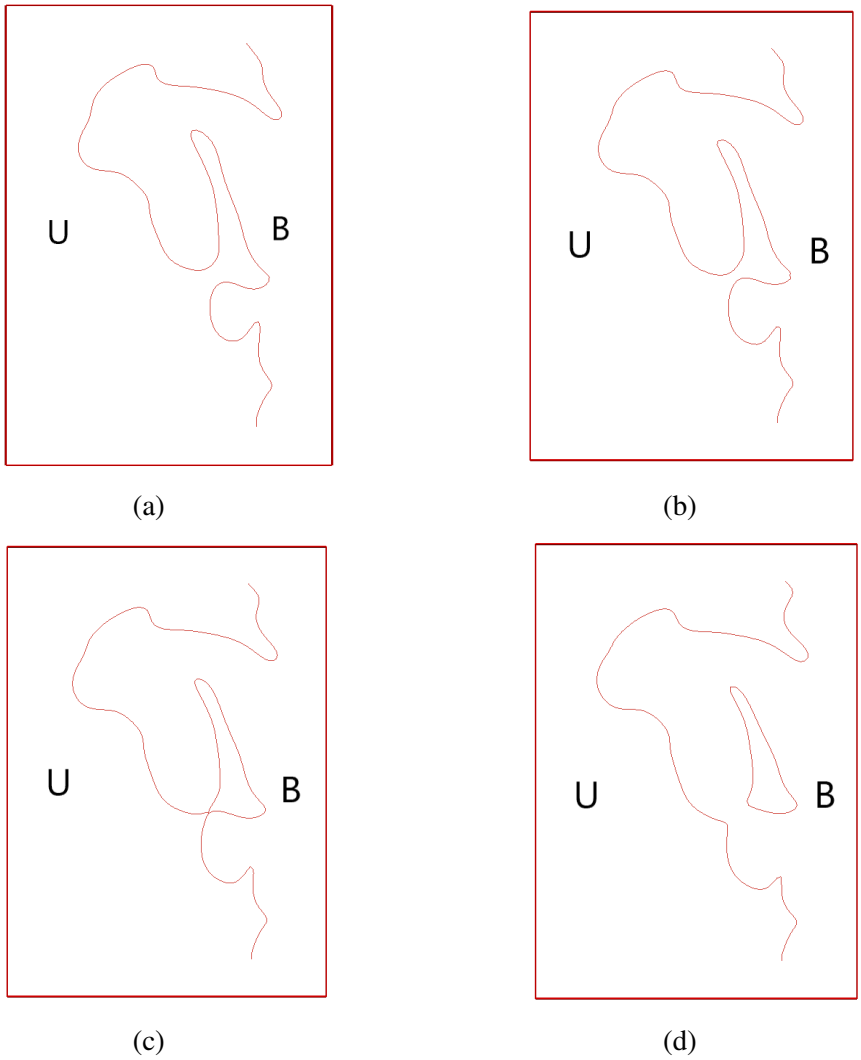

Fig. 5.1 Illustration of flame area change due to pocket formation in several stages: 5.1a shows an initial isosurface with relatively large surface area, 5.1b shows two local surfaces approaching each other, 5.1c shows the surfaces colliding and 5.1d shows an isolated pocket. The pocket burns out rapidly leaving behind an isosurface with a relatively smaller surface area. Letter 'U' represents unburnt reactants and letter 'B' represents burnt products.

When the scales of the turbulence become smaller than the flame thickness, recall that s_T follows the relationship [61] (Eqn. 2.35)

$$s_T/s_L = \frac{A_T}{A_L}\left(1+\frac{D_T}{D}\right)^{1/2}$$

consisting of both enhancement in flame surface area and turbulent diffusivity. This is particularly important in the thin reaction zones regime where the size of the smallest

turbulence length scales η becomes less than δ_L. Flame-flame interaction may be responsible for another phenomenon described as follows. In the thin reaction zone where the isosurfaces of c are not parallel with each other especially within the preheat zone, critical points are created when these isosurfaces curve and self interact within the flame. The resulting pockets in these cases are not flame pockets but simply diffusion pockets with no reactions within them. Such pockets can form under the influence of diffusion alone [20]. It is hypothesised that the "burnout" of such pockets enhances the transport of the reactants into the flame, and hence the turbulent diffusivity D_T. It remains an open question as to when D_T becomes significant enough to affect s_T and this is explored in the future.

5.2 DNS dataset for the current study

The dataset created for this analysis is similar to the twin flame setup in Chapter 4 Section 4.1.2 simulated using the DNS code `Senga2` [68] and is summarised as follows. A pair of statistically planar flames facing each other with fresh reactants between them are simulated in a cuboidal domain of cross section 5mm $\times$ 5mm. These simulations employ a single-step reaction mechanism which is tuned to replicate the flame propagation speed s_L of a stoichiometric methane-air flame, i.e. 39 cm/s, and also to capture the corresponding flame thickness δ_L. A field of homogeneous isotropic turbulence of desired intensity computed *a priori* is mapped onto the domain. The flames and turbulence evolve together as the flames propagate towards each other.

In this dataset, both turbulence intensity u' and integral length scale ℓ_0 are systematically changed. For $u' = 10s_L$ and $20s_L$, the integral length scales corresponding to $\ell_0 = 5\delta_L$, $\ell_0 = 2\delta_L$ and $\ell_0 = 1.25\delta_L$ are simulated. For $u' = 30s_L$, the values of $\ell_0 = 5\delta_L$, and $2\delta_L$ are considered and for $u' = 40s_L$ only $\ell_0 = 2\delta_L$ is simulated. The mesh spacing Δx, which is constant in all three directions, is varied in each case to match the Kolmogorov scale η and the simulation runtime was kept at 4 eddy turnover times, i.e. $t = 4\tau$. A summary of the important parameters for each simulation is provided in Table 5.1.

The separation between the flames is kept larger than that in the twin flame setup analysed earlier. It is varied for the individual cases such that the flames do not collide even at the end of the run. Figure 5.2 shows results from the cases with three different ℓ_0 values for $u' = 10s_L$. For the highest ℓ_0 value (Fig. 5.2a), the large scale wrinkling requires larger separation between the two flames,whereas for the smaller ℓ_0 values (Figs. 5.2b and 5.2c) smaller separation is sufficient to keep the two flames from interacting. This setup captures only self-interactions within the two individual flames within the domain. The turbulence here is linearly forced between the two flames to keep it from decaying rapidly [76].

	$\ell_0 = 5\delta_L$	$\ell_0 = 2\delta_L$	$\ell_0 = 1.25\delta_L$
$u' = 10s_L$			
Ka	14.14	22.36	28.28
Da	0.5	0.2	0.125
Re	50	20	12.5
η (μm)	39.27	24.85	20.33
Δx (μm)	41.66	26.04	20.833
$u' = 20s_L$			
Ka	40.0	63.25	80.0
Da	0.25	0.1	0.0625
Re	100	40	25
η (μm)	28.76	18.19	14.38
Δx (μm)	26.04	17.36	13.02
$u' = 30s_L$			
Ka	73.5	116.2	
Da	0.166	0.0667	
Re	150	60	
η (μm)	23.48	14.85	
Δx (μm)	22.72	13.02	
$u' = 40s_L$			
Ka		178.9	
Da		0.05	
Re		80	
η (μm)		12.86	
Δx (μm)		11.90	

Table 5.1 Main parameters of the different cases in this dataset presented in a matrix format with increasing u' from top to bottom and decreasing ℓ_0 from left to right.

According to Lundgren [76], the momentum equation (eq. 2.38) can be modified to take the form

$$\frac{\partial}{\partial t}u_i + \frac{\partial}{\partial x_k}u_k u_i = -\frac{1}{\rho}\frac{\partial}{\partial x_i}p + \frac{1}{\rho}\frac{\partial}{\partial x_k}\tau_{ki} + Q_f u_i \tag{5.1}$$

Here, $Q_f = \varepsilon/2K$, ε being the dissipation rate and K is the turbulent kinetic energy averaged over the entire domain. This term ensures that the turbulent kinetic energy over the entire domain is preserved. Both ε and K are evaluated over the entire domain and are hence, constant at each grid point for a given time instance.

A known shortcoming of Lundgren's method [76] is that the turbulent length scale changes over time until it reaches a steady value [77, 78]. Klein et al. [77] attempted to fix

this issue by making the forcing term proportional to a high pass filtered value of velocity. However, no such correction has been applied in this work and it is likely that the associated length scales of turbulence change in time. In future, this issue should be addressed.

(a) $\ell_0 = 5.0\delta_L$

(b) $\ell_0 = 2.0\delta_L$

(c) $\ell_0 = 1.25\delta_L$

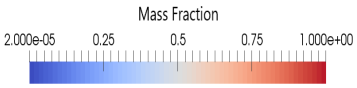

Fig. 5.2 Two dimensional slices of the 3-D snapshots of product mass fraction for cases $\ell_0 = 5\delta_L$, $\ell_0 = 2\delta_L$ and $\ell_0 = 1.25\delta_L$ (top to bottom) for fixed $u' = 10s_L$ taken after $t = 4\tau$. The separation between the flames is varied to keep them from interacting.

This dataset can be used to analyse the effects of integral length scale ℓ_0 while keeping the turbulence intensity u' fixed. Alternatively, a fixed value of ℓ_0 can be chosen and the variation in u' can be studied. Note that the Kolmogorov scale η also decreases as ℓ_0 decreases and/or u' increases. All the cases are in the thin reaction zones regime but a continuous surface was found to represent the reaction zone in all cases. No broken reaction zones were observed. The presence of two flames provides double the sample size for all the properties evaluated in this chapter. These include consumption speed, flame area and the number of isosurface interactions. The flame speed and flame area presented in this chapter provide the average

value of the two flames. The number of isosurface interactions, however, represents all the interactions for both flames.

5.3 Results

The probability density functions of mean curvature and tangential strain rate are plotted first to understand their distribution across the dataset. Subsequently, the statistics of isosurface interactions are evaluated in the same way as discussed in Chapters 3 and 4. The flame speed and flame area are analysed next, and their correlation with isosurface interactions is discussed. The last part of this section consists of separating out individual topologies isolated in a sub-domain and simulated separately. This is crucial in understanding the role of individual topological events on flame propagation.

5.3.1 Strain rate and curvature pdfs

The probability density functions (pdfs) of strain rate a_t and mean curvature κ are presented here. Values of a_t and κ are normalised by chemical time scale τ_c and unstrained laminar flame thickness δ_L respectively, and are analysed for the isosurface corresponding to $c = 0.8$ which represents the peak reaction rate. Figure 5.3 shows the variation of the pdfs with ℓ_0 for a fixed value of turbulence intensity at $u' = 20s_L$. The pdfs correspond to $\ell_0 = 5\delta_L, 2\delta_L$ and $1.25\delta_L$ and are represented by blue, red and yellow coloured lines respectively (see legend). The curvature pdfs are shown in Fig. 5.3a and the strain rate pdfs are in Fig 5.3b. The general shape of both κ and a_t pdfs is similar in all cases.

On closer inspection of the pdfs of κ (Fig. 5.3a), it can be seen that for the highest value of ℓ_0, i.e. $\ell_0 = 5\delta_L$ (blue line) the κ pdf has the highest peak but smallest overall width. The pdfs become lower and wider as the value of ℓ_0 decreases to $2\delta_L$. This is because as the value of ℓ_0 decreases, the corresponding Kolmogorov length scale η also decreases, that is, $\eta_{\ell_0=5\delta_L} > ... > \eta_{\ell_0=1.25\delta_L}$. This introduces an additional range of smaller length scales between $\eta_{\ell_0=5\delta_L} > l > \eta_{\ell_0=2\delta_L}$ for the $\ell_0 = 2\delta_L$ case. These additional small scales for each case correspond to higher κ ($\sim 1/R$) and result in more probable high curvature events as ℓ_0 decreases. Hence, the width of the mean curvature pdfs increases. Likewise, since the cases at lower ℓ_0 contain fewer large scale eddies with lower κ, the probability of low curvature events decreases, and thus the height of the peaks of the pdfs decreases. The height and width of the pdfs for $\ell_0 = 2\delta_L$ and $\ell_0 = 1.25\delta_L$ roughly remains the same suggesting a saturation in curvature pdf for values of ℓ_0 less than $2\delta_L$. Note that the peak of the pdfs shifts to the left towards more negative values as ℓ_0 decreases.

Now examining the pdfs of a_t, the peak value of the pdfs is again the highest for the largest ℓ_0 value, i.e. $\ell_0 = 5\delta_L$. The peaks of all the pdfs are at a positive value which is consistent with the previous findings in references [44, 50, 51]. The pdfs become shorter and their width increases as ℓ_0 decreases. Their peaks shift towards more positive values as ℓ_0 decreases suggesting that there is on average more positive straining for smaller ℓ_0 values and consequently, smaller η values.

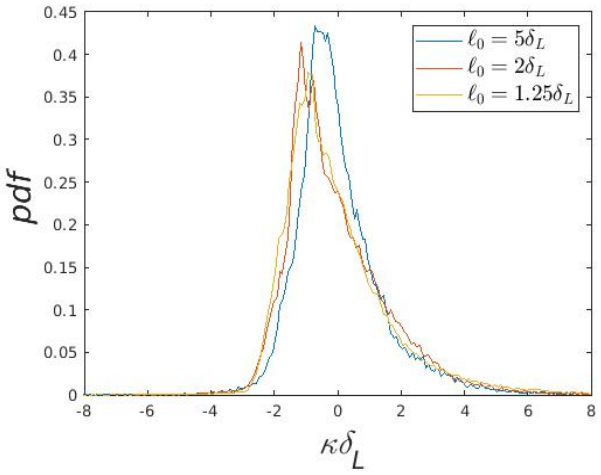

(a) Probability density function of mean curvature for a range of ℓ_0 values at $u' = 20s_L$.

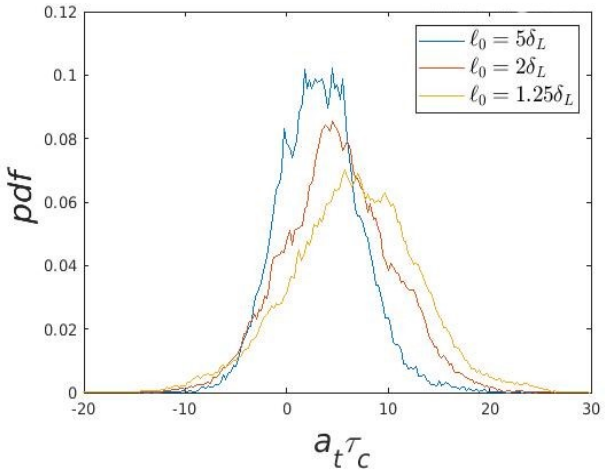

(b) Probability density function of tangential strain for a range of ℓ_0 values at $u' = 20s_L$.

Fig. 5.3 (a) Mean curvature κ and (b) strain rate a_t pdfs for three different ℓ_0 values represented by different colours at a fixed u' value. The curvature and strain rate are normalised by the unstrained laminar flame thickness δ_L and chemical time scale τ_c respectively.

Next, the pdfs for varying u' at fixed $\ell_0 = 2\delta_L$ are plotted. These are presented in Figure 5.4 for mean curvature κ (Fig. 5.4a) and tangential strain rate a_t (Fig. 5.4b). For the κ pdfs,

as u' increases the peaks shift towards more negative values. The height and width of the κ pdfs for $u' = 30s_L$ and $40s_L$ are roughly identical, again suggesting a saturation in κ pdfs as u' increases. The behaviour of these pdfs is consistent with the results of Nivarti and Cant [75].

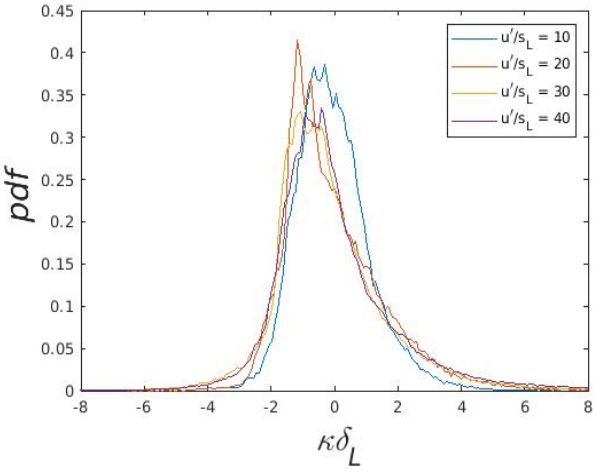

(a) Mean curvature pdfs for varying u' and fixed value of $\ell_0 = 2\delta_L$

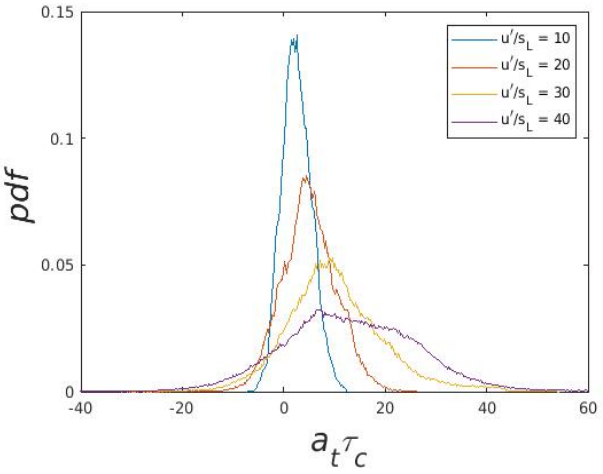

(b) Strain rate pdfs for varying u' and fixed value of $\ell_0 = 2\delta_L$

Fig. 5.4 (a) Mean curvature κ and (b) strain rate a_t pdfs for the increasing u' values represented by different colours. The curvature and strain rate are normalised by the unstrained laminar flame thickness δ_L and chemical time scale τ_c respectively.

For the strain rate pdfs, the height of their peaks decreases and their width increases as u' increases. The peaks for all the cases are observed at positive values of a_t which is consistent with previous findings [44, 50, 51]. The pdfs become increasingly wider as u' increases especially for the $u' = 40s_L$ case for which the pdf becomes significantly broader than the

other cases. The peaks of the pdfs shift towards the right as u' increases from $10s_L$ to $30s_L$ but at $u' = 40s_L$, the peak remains roughly at the same location as for $u' = 30s_L$.

5.3.2 Isosurface interactions

The total number of isosurface interactions is evaluated for this dataset using the critical point method described in Chapter 3. To obtain an adequate number of interactions for low intensity cases, cumulative results for multiple snapshots are analysed for each of the cases. The snapshots are set $t = 0.5\tau$ apart for the total run of 4τ which corresponds to 8 snapshots for each case. In addition, each simulation contains two flames and thus, the sample size is doubled by default.

The general shape of the resulting histograms of frequency of interactions against the progress variable was found to be consistent with all the hydrocarbon flame results throughout the thesis and hence, these histograms are not presented here. Instead, only the total number of isosurface interactions for each case is analysed and these are presented in Table 5.2. The top row in this table shows the results for $u' = 10s_L$ and the columns contain different values of ℓ_0 at this intensity. The subsequent rows show the values for $u' = 20s_L$, $30s_L$ and $40s_L$. Considering the isosurface interactions for varying u', it can be seen in Table 5.2 that for any given ℓ_0 value, the number of isosurface interactions increases as u' increases. This is consistent with the hydrocarbon results that have been previously presented in this thesis.

u'/s_L	ℓ_0		
	$5\delta_L$	$2\delta_L$	$1.25\delta_L$
10	1987	4551	5745
20	16882	24506	31574
30	59966	67779	
40		153606	

Table 5.2 Total number of isosurface interactions for an entire range of c for the current dataset. The values represent cumulative results for multiple snapshots up to $t = 4\tau$ for the two flames in the domain.

Next, the results for varying ℓ_0 for fixed values of u' are considered. It can be noted from Table 5.2 that for any fixed u' value, the number of isosurface interactions increase as ℓ_0 decreases. The corresponding surface averaged absolute mean curvature $\overline{|\kappa|}$ plotted against c is presented in Figure 5.5, normalised by the unstrained laminar flame thickness δ_L. The top row shows the results for $u' = 10s_L$, the middle row is for $u' = 20s_L$ and the bottom

row contains the results for $u' = 30s_L$. For each value of u', the value of $\overline{|\kappa|}$ increases as ℓ_0 decreases and hence, the number of isosurface interactions also increases.

On close inspection, especially towards the leading edge of the flames where most isosurface interactions occur, it can be observed that the values of $\overline{|\kappa|}$ for $\ell_0 = 5\delta_L$ (blue lines) and for $\ell_0 = 2\delta_L$ (red lines) come closer to each other as u' increases from $10s_L$ to $20s_L$ and then to $30s_L$. In fact, the blue lines and the red lines nearly overlap for $u' = 30s_L$ and the corresponding fractional difference in the frequency of isosurface interactions is only $\sim 13\%$ between $\ell_0 = 5\delta_L$ and $\ell_0 = 2\delta_L$ compared to $\sim 45\%$ for $u' = 20s_L$ and $\sim 129\%$ for $u' = 10s_L$. Likewise, the values of $\overline{|\kappa|}$ for $\ell_0 = 2\delta_L$ (red lines) and $\ell_0 = 1.25\delta_L$ (yellow lines) come closer as u' increases from $10s_L$ to $20s_L$.

This suggests a saturation in $\overline{|\kappa|}$ and possibly also in the number of isosurface interactions as the value ℓ_0 decreases. The saturation in $\overline{|\kappa|}$ is due to the fact that for the lowest ℓ_0 cases the Kolmogorov length scales η become too small to affect the flame curvature significantly. For $u' = 30s_L$ (Fig. 5.5c), the values of $\overline{|\kappa|}$ as well as the the frequency of isosurface interactions become nearly saturated for $\ell_0 = 5s_L$ whereas for $u' = 20s_L$ (Fig. 5.5b), the saturation in $\overline{|\kappa|}$ seems to occur at $\ell_0 = 2s_L$. The value of η at which the saturation occurs and its dependence on u' and other parameters requires further investigation which will be part of future work.

5.3.3 Flame Consumption Speed

The consumption speed s_T and flame area A_T evaluated using Eqns. 2.17 and 2.19 respectively and normalised with the unstrained laminar flame speed s_L and domain cross section A_L for the full dataset are presented in Table 5.3. Different sections of the table show results for the flames at different u' values as ℓ_0 is varied. The table also restates the total number of isosurface interactions (FF) for each case, along with the ratio $I_0 = (s_T/s_L)/(A_T/A_L)$.

There are several important observations to be made in Table 5.3. First, looking at both $u' = 10s_L$ and $20s_L$, the values of s_T/s_L and A_T/A_L are higher for $\ell_0 = 5\delta_L$ than for $\ell_0 = 2\delta_L$. Likewise, these values are higher for $\ell_0 = 2\delta_L$ than $\ell_0 = 1.25\delta_L$. Therefore,

$$s_{T,\ell_0=5\delta_L} > s_{T,\ell_0=2\delta_L} > s_{T,\ell_0=1.25\delta_L}$$

The value of s_T/s_L and the corresponding A_T/A_L differs by more than a factor of two between $\ell_0 = 5\delta_L$ and $\ell_0 = 1.25\delta_L$. This behaviour is consistent with the analysis of Peters [4]. Note that the ratio I_0 remains ~ 1 for all ℓ_0 values for $u' = 10s_L$ and $20s_L$. Therefore, these flames are within the framework of Damköhler's first hypothesis (see equation 2.16).

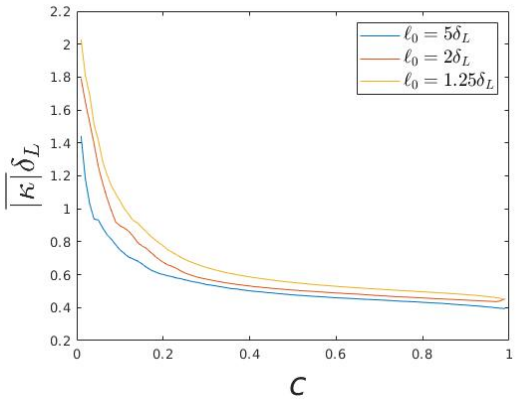

(a) $u' = 10s_L$

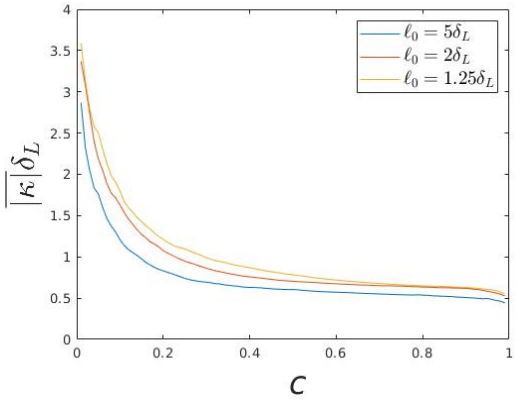

(b) $u' = 20s_L$

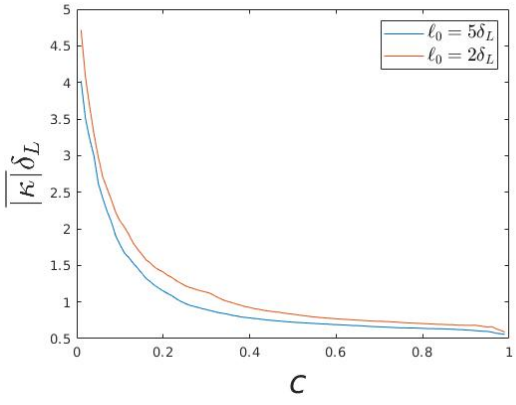

(c) $u' = 30s_L$

Fig. 5.5 Plots of surface averaged $|\kappa|$ for different u' values, normalised by untrained laminar flame thickness δ_L. Different coloured lines represent plots for different ℓ_0 values in each figure.

u'	ℓ_0/δ_L	s_T/s_L	A_T/A_L	I_0	FF
$10s_L$	5.0	3.94	3.89	1.012	1987
	2.0	2.74	2.75	0.996	4551
	1.25	1.68	1.71	0.984	5745
$20s_L$	5.0	6.74	6.41	1.050	16882
	2.0	3.23	3.22	1.002	24506
	1.25	2.27	2.37	0.958	31574
$30s_L$	5.0	7.12	6.52	1.091	59966
	2.0	4.35	4.17	1.042	67779
$40s_L$	2.0	4.388	4.147	1.058	153606

Table 5.3 The consumption speed s_T and flame surface area A_T (evaluated at $c = 0.8$) normalised by unstrained laminar flame speed s_L and domain cross section area A_L respectively for all cases. The values of I_0 and total number of isosurface interactions are also presented.

The next steps include analysing the impact of isosurface interactions on overall flame properties. For example, it is believed that the so-called "bending effect" [75] where s_T/s_L bends away from a linear relationship with u'/s_L, is caused by these interactions [3, 14]. The isosurface interactions conditioned on a carefully chosen value of c can help identifying the flame-flame interactions.

5.3.4 Analysis of Individual Topologies

Individual topologies, especially the reactant pockets, can play a significant role in flame propagation. This is consistent with the observations in references [15, 20] which suggest that the reactant pockets can affect the overall flame consumption speed and the formation of cusps can significantly affect the flame area. To investigate the behaviour of individual topologies, a method of capturing them from a bigger dataset such as the hydrogen flame dataset of Hawkes et al. [35], and simulating them separately using `Senga2` [68] is devised.

This is accomplished by inspecting the 3-D domain and identifying the isolated individual topological events. Once identified, a localised domain that fully contains the topological event is selected. For this domain, the properties such as density, temperature and species mass fractions are recorded for each point in order to create a restart file that can be read by `Senga2` [68] . The restart file is used as the initial setup for `Senga2` [68] and the boundary conditions are appropriately chosen. For a small domain and short run times, a domain with all periodic boundaries suffices. An example of a reactant pocket isolated from the Da+ case

of the Hawkes et al. [35] hydrogen dataset is simulated in `Senga2` [68]. A contour of an isosurface corresponding to $c = 0.8$ for four different stages in the temporal evolution of the pocket are shown in Figure 5.6. This pocket was captured in a 3-D domain with $30 \times 30 \times 30$ points. The reactant pocket starts out at a relatively large diameter and becomes smaller as time progresses. Thus, `Senga2` [68] accurately simulates the burnout of a reactant pocket separated out of the hydrogen flame simulated in a different DNS code, i.e. in S3D ([35]).

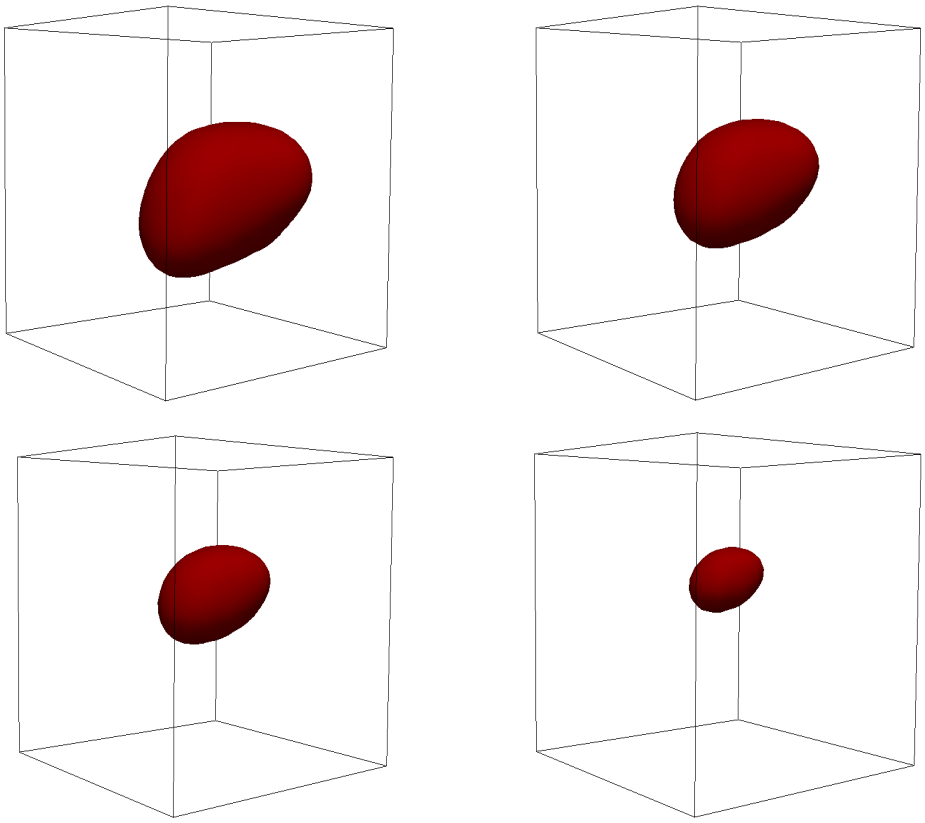

Fig. 5.6 Evolution of an isolated reactant pocket with time. This pocket is captured from the hydrogen flame dataset of Hawkes et al. [35] and simulated separately using Senga2 [68]

Simulating the individual topological events can provide insight into their behaviour locally and combined with their overall frequency of occurrence, their effect on overall flame propagation can be studied. In addition, it can also be used to validate the theory of pocket formation or to validate the models related to the topological events. For example, the displacement speed S_d can be divided into two categories, one during the normal flame propagation and second near flame-flame interaction events. Such models for S_d are under development and the above analysis can be used to validate them.

5.4 Chapter Conclusions

Chapter 5 of this thesis expands on the analysis of isosurface interactions performed in Chapter 3 and 4 by creating a matrix of simulations in which the integral length scales ℓ_0 as well as the turbulence intensity u' is varied. This dataset is similar to the twin flame dataset of Chapter 4, with a few notable differences: 1) the separation between the flames is kept large so that the flames do not collide at all and thus, only self-interactions occur, 2) linear forcing is applied between the two flames so that the turbulence does not decay rapidly as the flames propagate towards each other.

The probability density function (pdf) of the mean curvature and tangential strain rate is analysed first, with the focus on varying ℓ_0 for $u' = 20s_L$. It is found that as ℓ_0 decreases, both curvature and strain rate pdfs become shorter and wider. The peak of the curvature pdfs shifts to a more negative value whereas that of the strain rate shifts to a more positive value. The general shape of the pdfs remains similar for all ℓ_0 values. When ℓ_0 is kept constant and u' is increased, the peaks of the mean curvature pdfs move towards more negative values. The strain rate pdfs become shorter and wider as u' increases and the peaks shift towards more positive values. However, in these cases, the shape of the pdf changes as u' increases.

Next, the number of isosurface interactions is evaluated for this dataset and is found to increase as ℓ_0 decreases for any fixed u' value. The corresponding values of $\overline{|\kappa|}$ plotted against c also increase as ℓ_0 decreases. For $u' = 30s_L$, the fractional change in the frequency of interactions and the values of $\overline{|\kappa|}$ is smaller than those for the lower u' values when ℓ_0 changes from $5\delta_L$ to $2\delta_L$. This suggests an onset of saturation in these values which will be investigated as part of future research.

Finally, the flame speed and flame area is calculated for all the cases. The flame speed is found to be the highest for the highest value of ℓ_0 for fixed u'. This is consistent with the findings of Peters [4] and Nivarti et al. [61]. The ratio of s_T/a_L and A_T/A_L is found to be close to unity for all cases up to $u' = 30s_L$. At $u' = 40s_L$ and $\ell_0 = 2\delta_L$, it is found that $s_T/a_L > A_T/A_L$. The role of flame-flame interactions on overall flame propagation will be investigated with the help of critical points in future.

Chapter 6

Conclusions

This thesis aims to further the understanding of flame-flame interactions and their effect on flame propagation. This is accomplished in several steps. First, the flame topology at the location of flame-flame interactions is defined and their effect on flame surface is theoretically analysed with the help of the balance equation for the flame surface density Σ. The numerical method developed by Griffiths et al. [21] is used to identify the isosurface of progress variable interactions and their corresponding topology. The isosurface interaction at a carefully chosen value of c can be used to represent the flame-flame interactions. The statistics of isosurface interactions are presented along with their variation in the progress variable space.

The same numerical tools are applied to several DNS datasets. First, the established hydrogen flame dataset of Hawkes et al. [35] is considered. This dataset consists of two simulations, one at a higher Damköhler number Da = 0.54 called the Da+ case and the other at a lower Damköhler number Da = 0.13 called the Da- case. Second, a twin flame hydrocarbon dataset was created as part of the present investigation using the DNS code `Senga2` [68] to compare the results from the hydrogen flame datasets with those from the hydrocarbon flame datasets. The flames in these datasets eventually collide, making sure that an adequate number of isosurface interactions are captured. However, a significant number of self-interactions are found to exist within the flames. Third, these are analysed using the existing single flame DNS dataset of Nivarti et al. [75].

The datasets mentioned above only considered the variation in turbulence intensity u' with all other parameters held constant. The final part of the research added another dimension to the analysis by varying the integral length scale of turbulence ℓ_0 along with u'. The key findings in this thesis are summarised in the following sections.

Critical Points Method

In Chapter 3, the theory of critical points and their use in evaluating isosurface interactions is discussed. Critical points are defined as the points where the gradient of the progress variable, i.e. ∇c becomes zero. The location and the corresponding topology at the critical points was recorded using the numerical tools of Griffiths et al. [21]. To evaluate the topology at the critical points, the shape factors defined as the ratio of maximum to minimum principal curvature are calculated with the help of the Hessian matrix. The flame topology at the critical points can be categorised into four general groups called the Product Pockets (PP), Tunnel Formation (TF), Tunnel Closure (TC) and Reactant Pockets (RP). The numerical tools are applied to the hydrogen flame dataset of Hawkes et al. [35] for both the Da+ and Da- cases. The frequency of isosurface interactions is recorded for this dataset along with the individual topologies and the results are found to be consistent with those of Griffiths et al. [21].

Next, the terms of the Surface Density Function (SDF) equation are evaluated in the vicinity of the critical points. Using the lemma of Morse [34], the individual terms in the equation are expanded and it was found that the kinematic restoration term and the dissipation term become singular for both tunnel formation and tunnel closure events. However, the singularities cancel each other out exactly and the overall flame surface remains well behaved. The displacement speed S_d is also analysed at the critical points and it is found to be singular near all of the isosurface interaction event types. This suggests that S_d needs to be modelled separately near the critical points.

Hydrogen and Hydrocarbon Twin Flames

A detailed comparison between the isosurface interactions in hydrocarbon and hydrogen flames is drawn in the first part of Chapter 4. A twin flame hydrocarbon dataset with the flames propagating towards each other in homogeneous isotropic turbulence is created using DNS code `Senga2` [68]. Apart from the fuel type, this dataset is similar to the hydrogen flame dataset of Hawkes et al. [35] except that the turbulence in the hydrogen dataset is generated through shearing of the flow. Several cases at increasing turbulence intensity u' but constant integral length scale ℓ_0 were simulated as part of this hydrocarbon dataset and they were run until the flames fully annihilated each other.

It is observed that the number of isosurface interactions increase significantly in the case of hydrocarbon flames as u' increases. Most of the interactions are found at the leading edge of the flame, i.e. at low values of c, and their frequency decreases with increasing values of c. Very few interactions are recorded in the middle of the flame but there is a small rise in

their number at the trailing edge of the flame. This rise, however, still remains very small compared to the total number of interactions at the leading edge of the flame. For hydrogen flames, there is a significant number of isosurface interactions at the leading edge of the flame but the frequency of interactions at the trailing edge dominates that at the leading edge. Very few interactions are recorded in the middle of the flame for the hydrogen flames as well.

The high number of isosurface interactions at the leading edge results from highly curved isosurfaces at low values of c. This is shown with the help of the surface averaged absolute value of mean curvature $\mid \kappa \mid$ averaged over isosurfaces of c. The value of $\overline{\mid \kappa \mid}$ is found to be highest at the lowest values of c and it decreases monotonically in hydrocarbon flames as c increases. In the case of hydrogen flames, $\overline{\mid \kappa \mid}$ shows an increase at the trailing edge causing an increase in the frequency of isosurface interactions at the trailing edge of the hydrogen flames. This increase in $\overline{\mid \kappa \mid}$ is attributed to the combined effect of mean shear and thermo-dffusive instabilities caused by low Lewis number Le < 1. The lack of interactions in the middle of the flame for both hydrocarbon and hydrogen flames is caused by the small spacing between the isosurfaces in a region where the gradients are high due to chemical reaction.

Flame Self Interactions

The twin flame dataset contains a combination of interactions due to the collision of the two flame surfaces together with self-interactions within single flames. A significant number of self interactions can exist within single flames especially at high turbulence intensity. Self-interactions are responsible for phenomena such as pocket formation which do not exist in the case of head on collision between two flames. This makes a standalone analysis of self-interactions important in order to understand their overall effect on flame propagation.

For this purpose, the isosurface interactions in the single hydrocarbon flame dataset of Nivarti et al. [75] were analysed. Consistent with the twin flames setup, it is found that the number of interactions increases with u'. Most of the isosurface interactions exist at the leading edge of the flame and their number decreases as u' increases. Very few interactions are observed in the middle of the flame, however, there is a slight rise in their frequency at the trailing edge when compared to the middle of the flame.

An interesting picture emerges when plotting the fraction of individual topologies against u'. It is observed that the fraction of tunnel closure (TC) events and reactant pockets (RP) decreases and that of tunnel formation (TF) events and product pockets (PP) increases with increasing u'. Furthermore, the drop in the fraction of TC and RP is mirrored by the rise in the fraction of TF and PP. Both tunnel closure events and reactant pockets burn out at a high rate and the decrease in their fractions may affect the overall flame propagation at higher u'

values. Similar observations are made for the twin flame hydrocarbon dataset, however, no mirroring is observed.

Implications for Flame Propagation

The isosurface interaction analysis is extended to systematic variations in both integral length scales ℓ_0 as well as the turbulence intensity u'. A new hydrocarbon flame dataset is created for this purpose with the same configuration as the twin flame setup but with a larger separation between the two flames. These flames do not collide and hence all the isosurface interactions that occur in this dataset are self interactions. The probability density functions (pdfs) of the mean curvature and tangential strain rate are analysed first, focussing on varying ℓ_0 for $u' = 20s_L$. The pdfs for constant ℓ_0 and varying u' are also analysed.

Next, the number of isosurface interactions is evaluated for this dataset and is found to increase as ℓ_0 decreases for a fixed u'. The number of isosurface interactions also increases when ℓ_0 is kept constant and u' increases. The value of $\overline{|\kappa|}$ decreases as the value of c increases but reaches a saturation point as ℓ_0 decreases. The saturation point shifts towards a lower value of ℓ_0 as u' increases.

Finally, the changes in turbulence flame speed s_T and flame surface area A_T are analysed against the changes in the number of isosurface interactions. The values of s_T and A_T area are calculated for all the cases and both these properties are found to decrease as the value of ℓ_0 decreases for a fixed u'. This is consistent with the findings of Peters [4] and Nivarti et al. [61]. When u' is varied with constant ℓ_0, clear evidence is found that when isosurface interactions become significant, the flame speed shows the so called "bending effect."

Future Directions

Future work involves investigating individual topologies and their specific role in flame propagation. The individual topologies have already been captured in subdomains that can be separately simulated. Their effect can then be combined with the flame-flame interaction statistics to predict their effect on overall flame properties. For example, the displacement speed can be modelled separately during flame-flame interactions and development of such models are under way. By simulating individual topologies, such models can be validated.

The results from the simplified single-step reaction mechanism need to be validated with more detailed hydrocarbon combustion chemical schemes. Parametric studies involving systematic changes in the Lewis number need to be performed. Flame-flame interactions in different fuel types need to be compared. The results from the critical point method of finding flame-flame interactions needs to be compared with other such techniques, for example the

Dual Tree Wavelet Transform method used by Dunstan et al. [19, 36]. The numerical results can also be validated with experiments which are being performed for specifically studying flame-flame interactions [79, 80]. Further comparisons between the numerical results with high-intensity turbulence [81, 82] will also be useful.

References

[1] *BP Statistical Review of World Energy*. 2019. URL: bp.com/energyoutlook.

[2] G. Damköhler. "Der einfluss der turbulenz auf die flammengeschwindigkeit in gasgemschen". *Zeitschrift für Elektrochemie und angewandte physikalische Chemie* 46 (1940), pp. 601–652.

[3] J. M. Duclos, D. Verynante, and T. J. Poinsot. "A Comparison of Flamelet Models for Premixed Turbulent Combustion". *Combustion and Flame* 95 (1993), pp. 101–117.

[4] N. Peters. "The turbulent burning velocity for large-scale and small-scale turbulence". *Journal of Fluid Mechanics* 384 (1999), pp. 107–132.

[5] B. Karlovitz, D. W. Denniston, and F. E. Wells. "Investigation of Turbulent Flames". *J. Chem. Phys.* 19 (1951), p. 541.

[6] A. M. Klimov. "Laminar flame in turbulent flow". *Prikladnoy Mekhaniki i Tekhnicheskoy Fiziki Zhurnal (English translation AD-A200 241 Foreign Technology Division, Air Force Systems Command, 1988)* 3 (1963), pp. 49–58.

[7] F. A. Williams. *Combustion Theory*. Westview Press, 1985.

[8] Chung K. Law. "Dynamics of Stretched Flames". *Proceedings of the Combustion Institute* 22 (1988), pp. 1381–1402.

[9] S. B. Pope. "The Evolution of Surfaces in Turbulence". *International Journal of Engineering and Science* 26 (1988), pp. 445–469.

[10] S. M. Candel and T. J. Poinsot. "Flame Stretch and the Balance Equation for the Flame Area". *Combustion Science and Technology* 70 (1990), pp. 1–15.

[11] R. S. Cant, S. B. Pope, and K. N. C. Bray. "Modelling of flamelet surface–to–volume ratio in turbulent premixed combustion". *Twenty-Third Symposium (International) on Combustion, The Combustion Institute* (1990), pp. 809–815.

[12] K. N. C. Bray. "The Challenge of Turbulent Combustion". *Twenty-Sixth Symposium (International) on Combustion, The Combustion Institute* (1996), pp. 1–26.

[13] Y. B. Zel'dovich. "An Effect Which Stabilises The Curved Front of a Laminar Flame". *Zhurnal Prikladnoi Mekhanlki i Tekhnicheskoi Fiziki* 1 (1966), pp. 102–104.

[14] J. F. Driscoll. "Turbulent premixed combustion: Flamelet structure and its effect on turbulent burning velocities". *Progress in Energy and Combustion Science* 34 (2008), pp. 91–134.

[15] A. Y. Poludnenko and E. S. Oran. "The interaction of high-speed turbulence with flames: Turbulent flame speed". *Combustion and Flame* 158 (2011), pp. 301–326.

[16] R. Borghi. "Turbulent premixed combustion: Further discussions on the scales of fluctuations". *Combustion and Flame* 80 (1990), pp. 304–312.

[17] A. A. Burluka, A. Gorokhovski, and Borghi R. "Statistical model of turbulent premixed combustion with interacting flamelets". *Combust. Flame* 109 (1997), pp. 173–187.

[18] A. R. Kerstein. "Turbulence in Combustion Processes: Modeling Challenges". *Proceedings of the Combustion Institute* 29 (2002), pp. 1763–1773.

[19] T. D. Dunstan, N. Swaminathan, K. N. C. Bray, and N. G. Kingsbury. "Flame Interactions in Turbulent Premixed Twin V-flames." *Combustion Science and Technology* 185 (2013), pp. 134–159.

[20] J. H. Chen, T. Echekki, and W. Kollman. "The Mechanism of Two-Dimensional Pocket Formation in Lean Premixed Methane-Air Flames with Implications to Turbulent Combustion". *Combustion and Flame* 116 (1999), pp. 15–48.

[21] R. A. C. Griffiths, J. H. Chen, H. Kolla, R. S. Cant, and W. Kollman. "Three-dimensional topology of turbulent premixed flame interaction". *Proceedings of the Combustion Institute* 35 (2015), pp. 1341–1348.

[22] S. Trivedi, G. V. Nivarti, and R. S. Cant. "Flame self-interactions with increasing turbulence intensity". *Proceedings of the Combustion Institute* 37 (2019), pp. 2443–2449.

[23] W. Kollmann and J. H. Chen. "Pocket Formation and the Flame Surface Density Equation". *Twenty-Seventh Symposium (International) on Combustion, The Combustion Institute* (1998), pp. 927–934.

[24] S. Trivedi, R. A. C. Griffiths, H. Kolla, J. H. Chen, and R. S. Cant. "Topology of pocket formation in turbulent premixed flames". *Proceedings of the Combustion Institute* 37 (2019), pp. 2619–2626.

[25] T. Schuller, D. Durox, and S. Candel. "Dynamics of and noise radiated by a perturbed impinging premixed jet flame". *Combustion and Flame* 128 (2002), pp. 88–110.

[26] M. Talei, M. J. Brear, and E. R. Hawkes. "A parametric study of sound generation by premixed laminar flame annihilation". *Combustion and Flame* 159 (2012), pp. 757–769.

[27] D. Brouzet, A. Haghiri, M. Talei, and M. J. Brear. "Annihilation events topology and their generated sound in turbulent premixed flames". *Combustion and Flame* 204 (2019), pp. 268–277.

[28] C. L. Chen and S. H. Sohrab. "Upstream Interactions between Planar Symmetric Laminar Methane Premixed Flames". *Combustion and Flame* 101 (1995), pp. 360–370.

[29] T. Echekki, J. H. Chen, and I. R. Gran. "The Mechanism of Mutual Annihilation of Stoichiometric Premixed Methane-Air Flames". *Twenty-Sixth Symposium (International) on Combustion, The Combustion Institute* (1996), p. 855.

[30] S. H. Sohrab, Z. Y. Ye, and C. K. Law. "Theory of Interactive Combustion of Counterflow Premixed Flames". *Combustion Science and Technology* 45 (1986), pp. 27–45.

[31] P. A. Libby and F. A. Williams. "Strained Premixed Laminar Flames with Two Reaction Zones". *Combustion Science and Technology* 37 (1984), pp. 221–252.

[32] G. I. Sivashinsky. “On a Converging Spherical Flame Front”. *International Journal of Heat and Mass Transfer* 17 (1974), pp. 1499–1506.

[33] C. J. Sun and C. K. Law. “On the Consumption of Fuel Pockets via Inwardly Propagating Flames”. *Twenty-Seventh Symposium (International) on Combustion, The Combustion Institute* (1998), pp. 963–970.

[34] J. Milnor. *Analysis of Math. Studies*. Princeton University Press, 1963.

[35] E. R. Hawkes, O. Chatakonda, H. Kolla, A. R. Kerstein, and J. H. Chen. “A petascale direct numerical simulation study of the modelling of flame wrinkling for large-eddy simulations in intense turbulence”. *Combustion and Flame* 159 (2012), pp. 2690–2703.

[36] T. D. Dunstan, N. Swaminathan, K. N. C. Bray, and N. G. Kingsbury. “The effects of non-unity Lewis numbers on turbulent premixed flame interactions in a twin V-flame configuration.” *Combustion Science and Technology* 185 (6) (2013), pp. 874–897.

[37] T. Poinsot and D. Veynante. *Theoretical and Numerical Combustion*. R.T. Edwards, 2005.

[38] N. Peters. “Laminar Flamelet Conceps in Turbulent Combustion”. *Proc. Combust. Inst.* 21 (1986), pp. 1231–1250.

[39] P. A. Libby, K. N. C. Bray, and J. B. Moss. “Effects of finite reaction rate and molecular transport in premixed turbulent combustion”. *Combustion and Flame* 34 (1979), pp. 285–301.

[40] N. Peters. “A spectral closure for premixed turbulent combustion in the flamelet regime”. *Journal of Fluid Mechanics* 242 (1992), pp. 611–629.

[41] R. S. Cant and E. Mastorakos. *An introduction to turbulent reacting flows*. Imperial College Press, 2008.

[42] A. R. Kerstein, W. T. Ashurst, and F. A. Williams. “Field equation for interface propagation in an unsteady homogeneous flow field”. *Physical Review A* 37 (1988), p. 2728.

[43] N. Peters, P. Terhoeven, J. H. Chen, and T. Echekki. “Statistics of Flame Displacement Speeds From Computations of 2-D Unsteady Methane-Air Flames”. *Twenty-Seventh Symposium (International) on Combustion, The Combustion Institute* (1998), pp. 833–839.

[44] T. Echekki and J. H. Chen. “Unsteady Strain Rate and Curvature Effects in Turbulent Premixed Methane-Air Flames”. *Combustion and Flame* 106 (1996), pp. 184–202.

[45] H. G. Im and Chen J. H. “Preferential Diffusion Effects on the Burning Rate of Interacting Turbulent Premixed Hydrogen-Air Flames”. *Combustion and Flame* 131 (2002), pp. 246–258.

[46] S. B. Pope. *Turbulent flows*. Cambridge University Press, 2001.

[47] C. Meneveau and T. Poinsot. “Stretching and Quenching of Flamelets in Premixed Turbulent Combustion”. *Combustion and Flame* 86 (1991), pp. 311–332.

[48] N. Fogla, F. Creta, and M. Matalon. “Effect of folds and pockets on the topology and propagation of premixed turbulent flames”. *Combustion and Flame* 162 (2015), pp. 2758–2777.

[49] M. Boger, D. Veynante, H. Boughanem, and A. Trouve. “Direct Numerical Simulation analysis of flame surface density concept for Large Eddy Simulation of turbulent premixed combustion”. *Twenty-Seventh Symposium (International) on Combustion* 27 (1998), pp. 917–925.

[50] R. S. Cant, C. Rutland, and A. Trouve. “Statistics for laminar flamelet modelling”. *Proceedings of the Summer Program, Centre for Turbulence Research, Stanford University/NASA-AMES* (1990), pp. 299–310.

[51] N. Chakraborty and R. S. Cant. “Unsteady effects of strain rate and curvature on turbulent premixed flames in an inflow–outflow configuration”. *Combustion and Flame* 137 (2004), pp. 129–147.

[52] D. Bradley. “"How fast can we burn?"”. *Twenty-Fourth Symposium (International) on Combustion, The Combustion Institute* (1992), pp. 247–262.

[53] S. Ruan, N. Swaminathan, and Y. Mizobuchi. “Investigation of Flame Stretch in Turbulent Lifted Jet Flame”. *Combustion Science and Technology* 186 (2014), pp. 243–272.

[54] S. B. Pope, P. K. Yeung, and S. S. Girimaji. “The curvature of material surfaces in isotropic turbulence”. *Physics of Fluids* A 12 (1989), pp. 2010–2018.

[55] K. N. C. Bray and R. S. Cant. “Some applications of Kolmogorov’s turbulence research in the field of combustion”. *Proceedings of the Royal Society A* 434 (1991), pp. 217–240.

[56] E. R. Hawkes and J. H. Chen. “Comparison of direct numerical simulation of lean premixed methane–air flames with strained laminar flame calculations”. *Combustion and Flame* 144 (2006), pp. 112–125.

[57] A. Lipatnikov and J. Chomiak. “Turbulent flame speed and thickness: phenomenology, evaluation, and application in multi-dimensional simulations”. *Progress in Energy and Combustion Science* 28 (2002), pp. 1–74.

[58] J. Park and T. Echekki. “LES–ODT study of turbulent premixed interacting flames”. *Combustion and Flame* 159 (2012), pp. 609–620.

[59] R. Borghi. “On the structure and morphology of turbulent premixed flames”. In: *Recent Advances in the Aerospace Sciences*. Ed. by C. Casci and C. Bruno. Springer US, 1985, pp. 117–138.

[60] S. Lapointe, B. Savard, and G. Blanquart. “Differential diffusion effects, distributed burning, and local extinctions in high Karlovitz premixed flames”. *Combustion and Flame* 162 (2015), pp. 3341–3355.

[61] G. V. Nivarti, R. S. Cant, and S. Hochgreb. “Reconciling turbulent burning velocity with flame surface area in small-scale turbulence”. *Journal of Fluid Mechanics* 858 (2019).

[62] J. Li, Z. Zhao, A. Kazakov, and F. L. Dryer. “An Updated Comprehensive Kinetic Model of Hydrogen Combustion”. *International Journal of Chemical Kinetics* 36 (2004), pp. 566–575.

[63] J. H. Chen, A. Choudhary, B. de Supinski, M. DeVries, E. R. Hawkes, S. Klasky, W. K. Liao, K. L. Ma, J. Mellor-Crummey, N. Podhorszki, R. Sankaran, S. Shende, and C. S. Yoo. “Terascale direct numerical simulations of turbulent combustion using S3D”. *Computational Science and Discovery* 2 (2009), p. 015001.

[64] W. H. Press, S. A. Teukolsky, W. T. Vetterling, and B. P. Flannery. *Numerical Recipes, 3rd editon*. Cambridge University Press, 2007.

[65] A. Y. Poludnenko and E. S. Oran. "The interaction of high-speed turbulence with flames: Global properties and internal flame structure". *Combustion and Flame* 157 (2010), pp. 995–1011.

[66] D. C. Haworth and T. J. Poinsot. "Numerical simulations of Lewis number effects in turbulent premixed flames". *Journal of Fluid Mechanics* 244 (1992), pp. 405–436.

[67] C. J. Rutland and A. Trouve. "Direct Simulations of Premixed Turbulent Flames with Nonunity Lewis Numbers". *Combustion and Flame* 94 (1993), pp. 41–57.

[68] R. S. Cant. "Senga2 User Guide". *Technical Report CUED-THERMO* (2012).

[69] V. Giovangigli and M. D. Smooke. "Formulation of the premixed and nonpremixed test problems". In: *Reduced Kinetic Mechanisms and Asymptotic Approximations for Methane-Air Flames*. Ed. by M. D. Smooke. Springer-Verlag, 1991, pp. 1–28.

[70] T. Poinsot and S. Lele. "Boundary conditions for direct simulations of compressible viscous flows". *Journal of Computational Physics* 101 (1992), pp. 104–129.

[71] S. A. Orszag. "Numerical methods for the simulation of turbulence". *Phys. Fluids Suppl.* II (1972), pp. 250–257.

[72] G. K. Batchelor and A. A. Townsend. "Decay of turbulence in the final period". *Proc. Roy. Soc. Lond.* A194 (1948), pp. 527–543.

[73] G. K. Batchelor. *The Theory of Homogeneous Turbulence*. Cambridge University Press, 1953.

[74] S. Chaudhuri, H. Kolla, H. L. Dave, E. R. Hawkes, J. H. Chen, and C. K. Law. "Flame thickness and conditional scalar dissipation rate in a premixed temporal turbulent reacting jet". *Combustion and Flame* 184 (2017), pp. 273–285.

[75] G. V. Nivarti and R. S. Cant. "Direct numerical simulation of the bending effect in turbulent premixed flames". *Proceedings of the Combustion Institute* 36 (2017), pp. 1903–1910.

[76] T. S. Lundgren. "Linearly forced isotropic turbulence". *Annual Research Briefs, CTR Stanford* (2003), pp. 461–473.

[77] M. Klein, N. Chakraborty, and S. Ketterl. "A Comparison of Strategies for Direct Numerical Simulation of Turbulence Chemistry Interaction in Generic Planar Turbulent Premixed Flames". *Flow Turbulence and Combustion* 99 (2017), pp. 955–971.

[78] C. Rosales and C. Meneveau. "Linear forcing in numerical simulations of isotropic turbulence: Physical space implementations and convergence properties". *Physics of Fluids* 17 (2005), p. 095106.

[79] A. Tyagi, I. Boxx, S. Peluso, and J. O'Connor. "The role of flow interaction in flame-flame interaction events in a dual burner experiment". *Proceedings of the Combustion Institute* 37 (2019), pp. 2485–2491.

[80] A. Tyagi, I. Boxx, S. Peluso, and J. O'Connor. "Statistics and topology of local flame–flame interactions in turbulent flames". *Combustion and Flame* 203 (2019), pp. 92–104.

[81] T. M. Wabel, A. W. Skiba, and J. F. Driscoll. “Turbulent burning velocity measurements: extended to extreme levels of turbulence”. *Proceedings of the Combustion Institute* 36 (2017), pp. 1809–1816.

[82] A. W. Skiba, T. M. Wabel, C. D. Carter, S. D. Hammack, J. E. Temme, T. Lee, and J. F. Driscoll. “Reaction layer visualization: a comparison of two PLIF techniques and advantages of kHz-imaging”. *Proceedings of the Combustion Institute* 36 (2017), pp. 4593–4601.

Appendix A

Effect of Resolution on Isosurface Interaction Statistics

This appendix addresses the issue of resolution requirement to get sufficient accuracy in the simulation results. Ideally, a domain is considered well resolved if the mesh spacing Δx can resolve the Kolmogorov length scale η. However, due to the limitations on the computational cost, full resolution of the domain is not possible in some of the cases studied in this work. For example, the twin flame setup in Chapter 4 requires long runtimes for the flames in high intensity turbulence to interact fully. This simulation will be too expensive to carry out for a fully resolved domain and hence a trade-off is necessary. Also, the isosurface interaction analysis in the published work on self-interactions of flames (Chapter 4 Section 4.2.2) was performed on a dataset with $\eta < \Delta x$ [75]. It is necessary to understand the limitations of the results owing to the resolution.

A DNS sub-dataset is created which branches off from the twin flame setup discussed in Chapter 4 Section 4.1.2. All of the initial parameters in this dataset are exactly the same as the $u' = 20 s_L$ case in the twin flame dataset with two notable exceptions. First, a freely propagating single flame in an inflow-outflow configuration is employed here. For simplicity, the inflow was kept laminar with a speed equal to laminar flame speed s_L. The incoming reactants stay well away from the flame throughout the run and hence do not affect the flame or the turbulence interacting with the flame. Second, the mesh spacing Δx is varied. Three different cases are simulated corresponding to a low resolution case at $\Delta x/\eta = 3$ and two higher resolution cases at $\Delta x/\eta = 1$ and 0.75. Figure A.1 shows slices of the product mass fraction for the lowest and highest resolution cases after $t = 3\tau$ runtime.

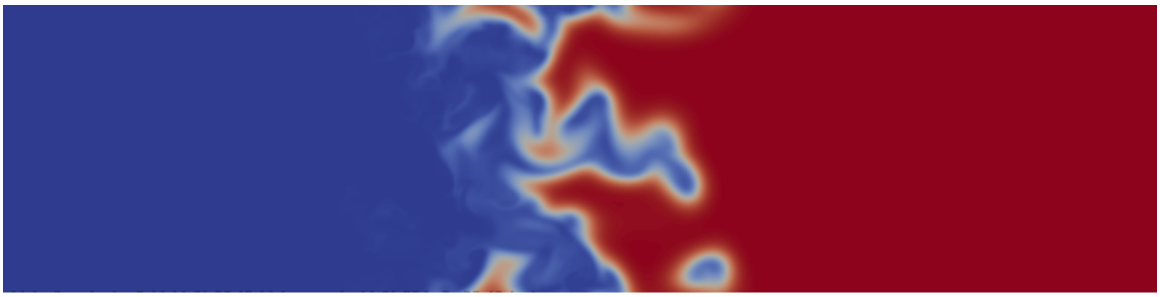

(a) $\Delta x/\eta = 3$

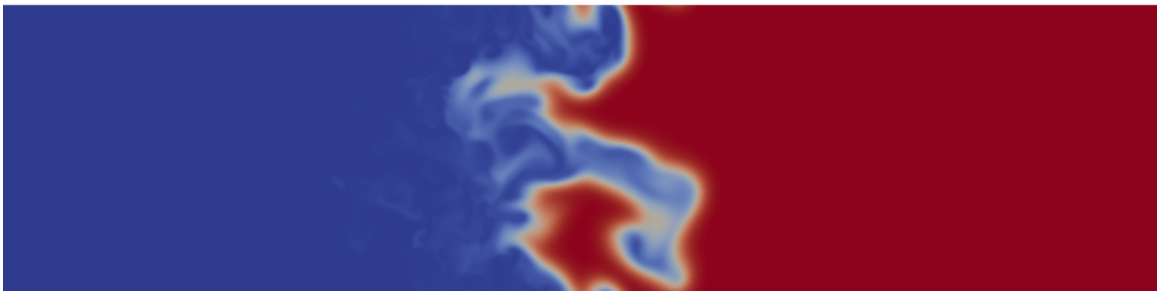

(b) $\Delta x/\eta = 0.75$

Fig. A.1 Slices of snapshots of product mass fractions for the lowest (top) and highest (bottom) resolution cases

The isosurface interaction statistics of the above dataset are evaluated with the help of the critical point method (see Chapter 3) and the corresponding topology at the location of the isosurface interactions are recorded using the numerical method of Griffiths et al. [21]. The statistics are presented in the form of histograms plotted against the progress variable for all the cases. Changes in flame area with resolution are also analysed.

A.1 Isosurface Interaction Statistics

Histograms showing the frequency of isosurface interactions against the progress variable are shown in Figure A.2. These histograms contain the cumulative statistics of multiple snapshots taken during the total runtime of $t = 3\tau$ set 0.25τ apart each. The histograms from top to bottom correspond to $\Delta x/\eta = 3, 1$ and 0.75 respectively. Figures on the left are for $0.01 < c < 0.99$ whereas those on the right are specifically for $0.3 < c < 0.99$ since this range is not discernible on the left figures. It is immediately noticeable that the histograms all take qualitatively similar shapes for all cases. The observed trend is consistent with the hydrocarbon flame results discussed throughout the thesis.

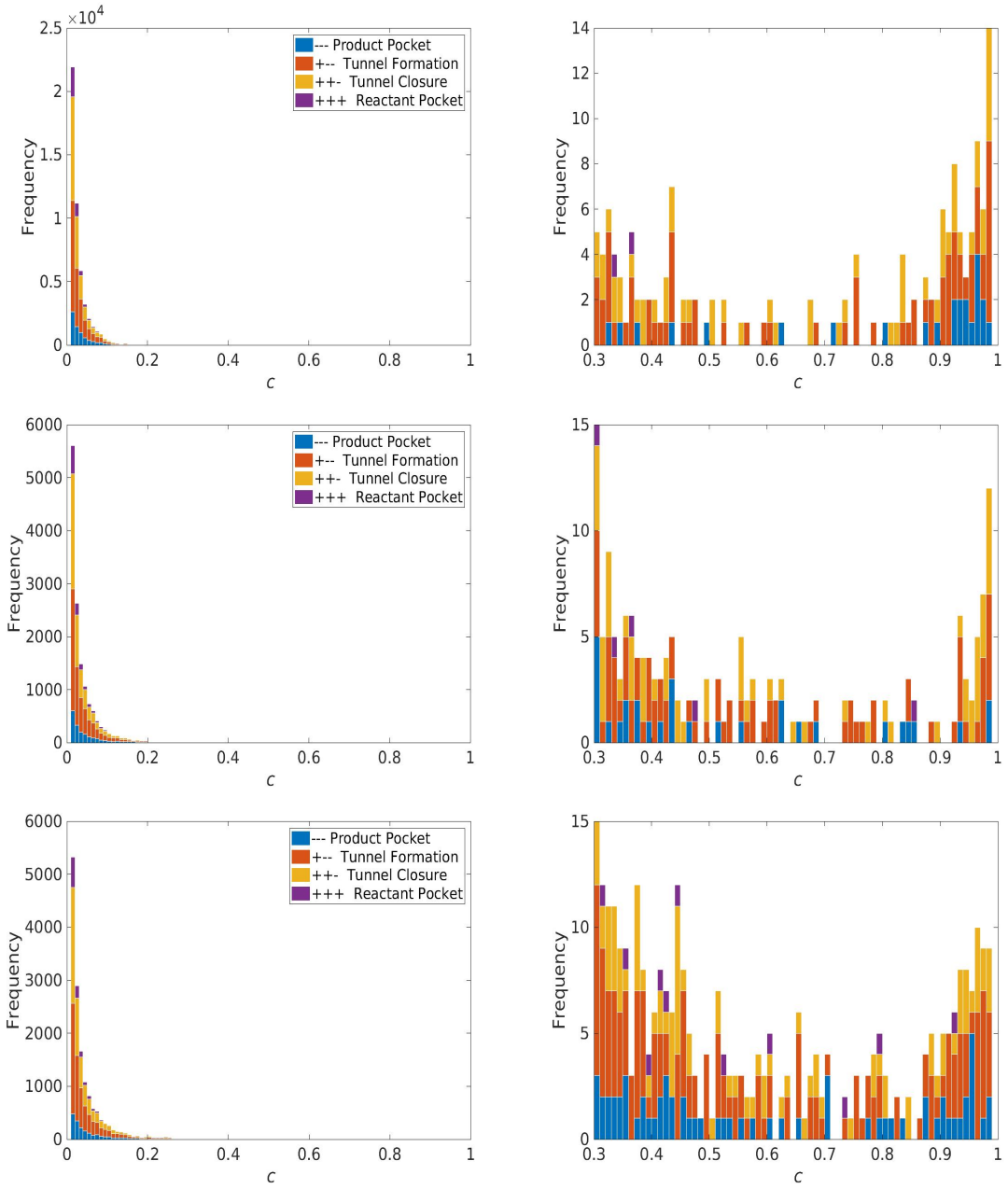

Fig. A.2 Histograms for the frequency of occurrence of different topologies represented by different colours. The left column shows the frequency of interactions for $0.01 < c < 0.99$ and the right column focusses on the frequency of interactions for $0.3 < c < 0.99$.

The total number of isosurface interactions as well as the frequency of occurrence of individual topologies are summarised in Table A.1. The number of interactions resulting from the low resolution case (top row) is found to be significantly higher than the higher resolution cases. At the same time, the number of interactions for the $\Delta x/\eta = 1$ case is nearly

equal to that for the $\Delta x/\eta = 0.75$ case. A similar observation is made for the fraction of topologies which are almost identical for the higher resolution cases. In the lower resolution case, the fractions are accurate to within 15% of the high resolution cases.

Interactions	$\Delta x/\eta$		
	3.0	1.0	0.75
Total	49678	14241	15343
PP	0.1423	0.1282	0.1230
TF	0.4171	0.4289	0.4270
TC	0.3497	0.3622	0.3695
RP	0.0909	0.0806	0.0804

Table A.1 Total interactions and fraction of individual topologies at different domain resolution levels

A high number of isosurface interactions for the low resolution case results from the fact that a critical point is recorded when the isosurfaces come within one mesh point from each other. Since the mesh spacing is larger for the $\Delta x/\eta = 3$ case, the probability of finding the interpolated isosurfaces within one mesh spacing in a frozen snapshot becomes greater. This is illustrated in Figure A.3 showing two isosurfaces at an equal c value that are approaching each other (red lines). The surfaces have already come within the mesh spacing for the low resolution case (high Δx) and hence, a critical point is recorded. By contrast, in case of higher resolution (low Δx), the surfaces are more than the mesh spacing apart.

Despite a higher number of isosurface interactions being recorded at low resolution, it can be assumed that the critical points are being accurately captured when they come within one mesh spacing. This is seen in Figure A.2 where the correct shape of the histogram is achieved even for the lowest resolution case. Therefore, for analysis of the general location of critical points and the magnitude of the frequency of occurrence, low resolution of approximately $\Delta x/\eta = 3$ is adequate. For accurate numbers of interactions and more precise topology fractions, resolving the Kolmogorov scales becomes necessary requiring a mesh spacing corresponding to $\Delta x/\eta = 1$ or lower.

A.2 Flame Area

The cases corresponding to $\Delta x/\eta = 3.0$ and $\Delta x/\eta = 1.0$ are simulated further for the total runtime of $t = 12\tau$. The flame area for these cases is presented in Fig. A.4. Is is found that the lower resolution case constantly over-predicts the flame area. This suggests that to

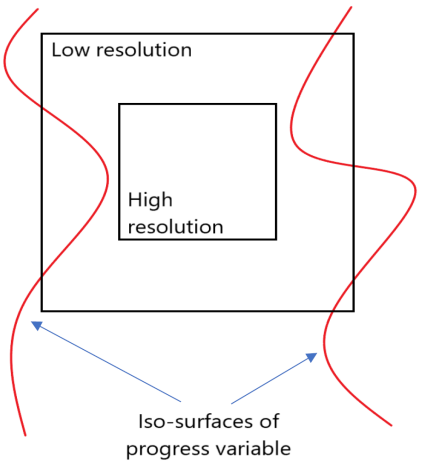

Fig. A.3 Illustration of effect of low resolution (high Δx vs higher resolution (low Δx) in isosurface interaction. The isosurfaces of the progress variable come within the mesh spacing (hence, a critical point will be recorded) for the low resolution case but not for the high resolution case.

evaluate specific properties such as flame area or consumption speed, a fully resolved domain is more important.

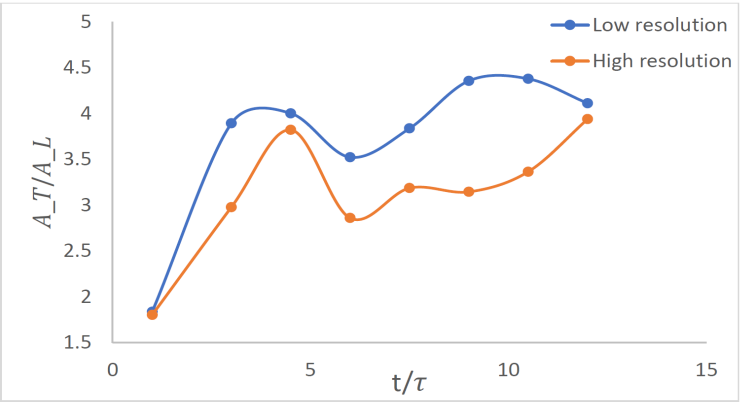

Fig. A.4 Flame area change with time for low resolution (blue line) and high resolution (red line) cases

Appendix B

List of Publications

The research presented in this thesis has been presented in the following papers:

- S. Trivedi, R. A. C. Griffiths, H. Kolla, J. H. Chen, and R. S. Cant. “Topology of pocket formation in turbulent premixed flames”. Proceedings of the Combustion Institute 37 (2019), pp. 2619–2626.
- S. Trivedi, G. V. Nivarti, and R. S. Cant. “Flame self-interactions with increasing turbulence intensity”. Proceedings of the Combustion Institute 37 (2019), pp. 2443–2449.
- (Book Chapter) S. Trivedi, G. V. Nivarti, and R. S. Cant. “Analysis of Flame Topology and Burning Rates”. In: DNS data analysis for turbulent combustion. *Submitted*.
- S. Trivedi, H. Kolla, J. H. Chen, and R. S. Cant. “Comparison Between Flame-Flame Interactions in Hydrogen and Hydrocarbon Flames”. *In preparation*.
- S. Trivedi, G. V. Nivarti, and R. S. Cant. “DNS analysis of flame propagation at different turbulence length scales”. 11^{th} U.S. National Combustion Meeting (2019).

The research work in this thesis has also been presented in the following conferences:

- S. Trivedi, R.A.C. Griffiths and R.S. Cant "Three-Dimensional Flame-Flame Interaction Topology for Premixed Hydrocarbon Flames". 16^{th} International Conference on Numerical Combustion (2017), Orlando, USA.
- S. Trivedi, G. V. Nivarti, and R. S. Cant. “Flame self-interactions with increasing turbulence intensity”. 37^{th} International Symposium on Combustion (2018), Dublin, Ireland

- S. Trivedi, R. A. C. Griffiths, H. Kolla, J. H. Chen, and R. S. Cant. "Topology of pocket formation in turbulent premixed flames". 37^{th} International Symposium on Combustion (2018), Dublin, Ireland

- S. Trivedi, H. Kolla, J. H. Chen, and R. S. Cant. "Comparison Between Flame-Flame Interactions in Hydrogen and Hydrocarbon Flames". UKCTRF Annual Meeting (2018), Cambridge, UK.

- S. Trivedi, G. V. Nivarti, and R. S. Cant. "DNS analysis of flame propagation at different turbulence length scales". 11^{th} U.S. National Combustion Meeting (2019), Pasadena, California